ELECTRONIC PROPERTIES OF ELECTRODEPOSITED SEMICONDUCTOR JUNCTIONS

SHAWN MICHAEL EDWARD CHATMAN


CENTRE FOR NFLD. STUDIES
MEMORIAL UNIVERSITY
OF NEWFOUNDLAND

Electronic Properties of Electrodeposited Semiconductor Junctions

by

Shawn Michael Edward Chatman

Master of Science

A Thesis Submitted in Partial Fulfilment of
the Requirements for the Degree of

Doctorate of Philosophy

Department of Physics and Physical Oceanography
Memorial University of Newfoundland

August, 2009

St. John's Newfoundland Labrador

Abstract

This thesis describes the synthesis, structural properties, optical properties, and electronic properties of semiconductor junctions based on electrochemically deposited ZnO and Cu_2O thin films. The first focus is characterizing the effect of deposition conditions (including applied potential and electrolyte composition) on the fundamental properties of these materials (including carrier concentration, band gap, and microstructure). Subsequent discussion addresses electrical conduction to and through ZnO/substrate junctions as a function of these deposition conditions. Finally, three device applications for these ZnO-based junction are explored: Schottky rectifiers, humidity sensors, and photovoltaic cells. Since electrical conduction to and through heterojunction interfaces is very important for maximizing the functionality of semiconductor devices, this thesis work is an essential step towards increasing the functionality of multi-layer ZnO-based heterojunction devices prepared by electrodeposition.

Capacitive Mott-Schottky analyses showed that the carrier concentrations of our ZnO electrodeposits are dependent upon deposition potential, with higher net carrier concentration at more positive potentials. UV/Visible diffuse reflectance data indicates that band gap increases with more positive deposition potentials. Together, these results suggest that hydrogen is the dominant, yet unintentional, Moss-Burstein

like dopant in our *n*-type ZnO. Furthermore, the range of carrier concentrations we can achieve ($10^{18} - 10^{21}$ cm^{-3}) is comparable to that obtained with intentional doping. This is significant because using deposition potential to change growth rate or morphology will simultaneously change electronic properties.

The deposition potential studies evolved into a procedure for selective, one-step production of either ohmic or rectifying (Schottky) ZnO/metal junctions (Chatman *et al.*, *Appl.Phys.Lett.*, **2008**, 92, 012103/1-3). Rectifying ratio and soft-breakdown characteristics can be influenced by tuning either deposition potential and *p*H (Chatman *et al.*, *ACS Appl. Mater. Interfaces*, **2009**, 1, 552-558). (In contrast, our Cu_2O/metal junctions were always ohmic.) Rectifying ZnO/metal junctions are very susceptible to relative humidity compared with ohmic samples because of protonic conduction at the ZnO/air interface. Hydrophobic coatings applied to ZnO deposits greatly reduce the erratic sensitivity of ZnO at high humidities while retaining humidity sensitivity (Chatman *et al.*, *ACS Appl. Mater. Interfaces*, **2009**, 1, 552-558).

ZnO/Cu_2O *pn* junctions were prepared with different permutations of a two-step electrodeposition process. ZnO/Cu_2O/metal junctions were determined to be light sensitive when the Cu_2O layer was deposited using lactate-based electrolytes. Unfortunately, solar conversion efficiencies was too low to determine device efficiencies.

Acknowledgements

I would like to thank Dr. Kristin Poduska for all her time, effort, and patience during the completion of this work. In particular, I'd like to thank her for her tireless editing work she undertook during the completion of this thesis, without which this text would not have come together so well. Without her generous contributions, this thesis work would never have been written.

I would also like to that by doctoral review committee, Dr. Qiying Chen and Dr. John Whitehead. Their advice and input helped me overcome many challenging areas of my research.

I would like to thank my mother and father for their continued support over the last half-dozen years. Without their unwaivering belief in me, my time at university would have been much more difficult.

I would like to thank all the other graduate students who I worked with and around: Tingting Ren, Kitty Kumar, Asim Rasheed, and Ramesh Kumar. I would especially like to thank Lisa Emberley and Bernard Ryan who worked closely with me during their time with the research group.

I would also like to thank Dr. R. Mason, H. Gillespie, L. Men (SEM), and M. Shaffer (XRD and SEM facilities at Memorial University of Newfoundland). I also acknowledge financial support from the Natural Science and Engineering Resource

Council (Canada), Canada Foundation for Innovation New Opportunities Fund, and Memorial University of Newfoundland.

List of Abbreviations

AC	Alternating Current
ACS	American Chemical Society
AFM	Atomic Force Microscopy
CE	Counter Electrode
CIGS	$Cu(In,Ga)Se_2$
CREAIT	Core Research Equipment and Instrument Training Network
CV	Cyclic Voltammogram
CZS	$Cu_2O/ZnO/substrate$
DC	Direct Current
EDX	Energy Dispersive X-ray
HER	Hydrogen Evolution Reaction
ITO	Indium tin oxide
I–V	Current-Voltage
JCPDS	Joint Committee on Powder Diffraction Standards
MS	Mott-Schottky
MUN	Memorial University of Newfoundland
OTS	Octadecyltrichlorosilane
PAR	Princeton Applied Research
PV	Photovoltaic
RE	Reference Electrode
RH	Relative Humidity
SEM	Scanning Electron Microscopy
STP	Standard Temperature and Pressure
UHV	Ultra High Vacuum
UV	Ultraviolet
VI	Virtual Instrument
WE	Working Electrode
XRD	X-ray Diffraction
ZCS	$ZnO/Cu_2O/substrate$

Contents

List of Tables

List of Figures

Chapter 1

Introduction

The construction of practical semiconducting devices, such as photovoltaic solar cells and miniaturized semiconducting transistors, has been considered one of the most important avenues leading to the advancement of technology[1, 2, 3, 4]. Therefore, it is useful to identify factors that can improve semiconductor device functionality. In broad strokes, the four most important elements that must be considered when designing semiconductor devices are functionality, efficiency/quality, cost, and toxicity[5]. By using electrochemical synthesis techniques, we can effectively reduce the cost of synthesizing low-toxicity semiconducting materials. This thesis describes the study of electrodeposited metal oxides that are prime candidates for use in next-generation electronic and optical devices[6, 7, 8]. In particular, I have explored conduction to and through single layers of ZnO, and how these ZnO single layers can be utilized in *pn* junctions with Cu_2O.

ZnO is a transparent wide band direct gap semiconductor with a band gap (E_g) of $3.1-3.5$ eV at room temperature[9, 10]. It has a hexagonal wurtzite crystal structure (space group $P6_3mc$) with lattice constants $a = 3.255$ Å and $c = 5.217$ Å, and a four atom basis (Figure 1.1)[11]. Though there has been some recent debate on the source of n-type conduction in native zinc oxide, it is generally attributed to interstitial hydrogen doping[12, 13, 14]. ZnO is non-toxic, especially compared to heavy metal (Cd, Ga, As) containing semiconductors, making it an excellent candidate for technological use. Indeed, ZnO has recently enjoyed a large amount of attention in the literature due to its electrical and optical properties[15, 16, 17]. It has been utilized as a transparent window material and to create pn heterojunctions in photovoltaic cells[18], and also to form other current limiting devices[19, 20]. Even though ZnO has been studied previously for use in electrical devices, there is still much that is not understood about the surface and interface conduction properties of ZnO, especially with respect to native doping[21, 22].

Traditionally, semiconducting devices have been manufactured using techniques such as laser ablation (for nanowire arrays)[23], chemical vapor deposition (for UV detectors)[24], and electron beam evaporation (for Schottky diodes)[25]. These techniques typically involve high temperature or high energy deposition conditions, as well as post-deposition annealing. This can necessitate substantial start-up and operation costs, including procuring high-purity solid metal or semiconductor starting ingots, contributing greatly to the price of synthesis. Alternative synthesis methods include

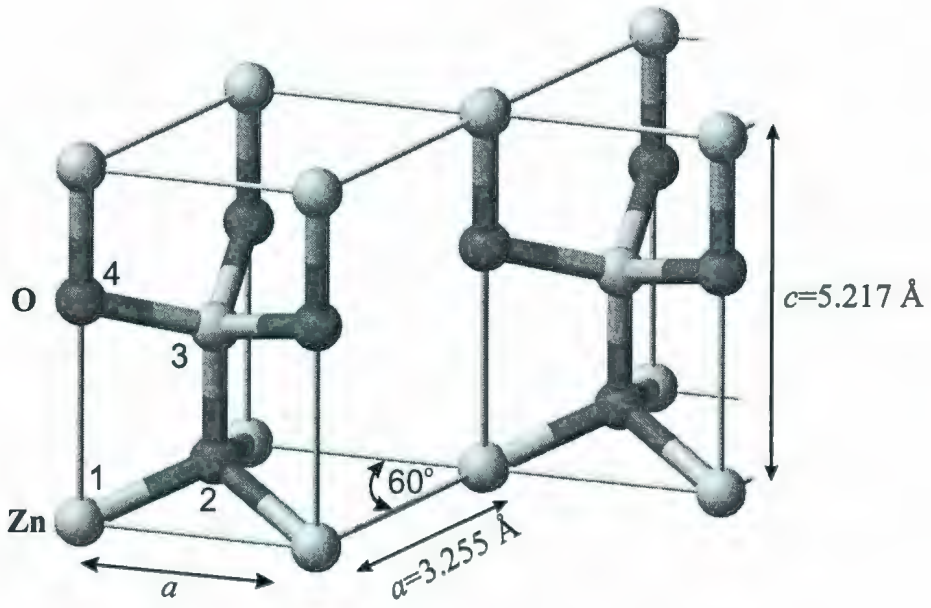

Figure 1.1: Schematic representation of two unit cells of ZnO's wurtzite crystal structure. The light grey spheres represent Zn while the dark grey spheres represent O. ZnO has a four atoms basis consisting of two Zn atoms and two O atoms. One possible basis scheme is labeled 1 through 4.

solution-based electrodeposition or chemical precipitation synthesis. Their economical source materials (commercially available metal salts for aqueous electrolytes) and synthesis equipment (stable voltage sources and hotplates), leads to greatly reduced start-up and operation costs while retaining the ability for controlled growth of high-quality thin films.

While the cost advantage of using electrodeposition is a great impetus in itself, the flexibility of electrodeposition techniques allow us to influence the electrical and optical characteristics of materials, making this technique very useful. For example, this method has been used to synthesize and tailor thin films for technologies such as giant magnetoresistant materials[26, 27], solar cells[28, 29], and magnetic spin-valves devices[30, 31, 32]. Like all synthesis techniques, electrodeposition has drawbacks as well. Electrodeposits typically have very rough surfaces[33] (compared to techniques such as molecular beam epitaxy), which can be detrimental for electronic devices[34, 35]. It can also be difficult to deposit some phases due to complicated aqueous stability relations (see Chapter 2).

Of particular interest in recent literature is the formation of semiconductor/metal interfaces utilizing electrodeposition to synthesize at least one of the layers. For example, Vaidyanathan *et al.*[36] have demonstrated the ability to grow alternating selenide/telluride superlattices on titanium by atomic layer deposition, the electrochemical equivalent of atomic layer epitaxy. This technique offers the ability to create very flat interfaces between layers that are on the order of a few atoms

thick for thermoelectric and infrared devices. The magnetic properties of electrodeposited metal/semiconductor junctions for spintronic devices has also been recently explored. For example, Bao *et al.* have electrodeposited Fe_xNi_{1-x} thin films on commercially available GaAs wafers[37]. Others have worked on spin-polarized permalloy on Si[27], CoNiCu/Cu multi-layers on Au/Si substrates[26], and $Ni_{80}Fe_2O$/Cu/Co/Cu spin-valve multi-layers on NiFe[30] for giant magnetoresistant devices. As a whole, electrodeposition of semiconductor/metal junctions is enjoying a large amount of research attention. Often these studies focus on very thin (four atoms thick)[36] or epitaxial growth layers on single crystals[38, 39]. Our work explores thicker layers with near-bulk electronic properties, but with complicated grain structures (unlike commercially-produced single crystal wafers).

In this thesis, I have compiled my publications[40, 41] exploring the electronic characteristics of electrodeposited ZnO. Background information and experimental details relevant for all work is provided in Chapter 2 and Chapter 3, respectively. Chapter 4 describes our discovery of the ability to selectively create ohmic or rectifying (Schottky) ZnO/metal junctions by changing the deposition potential[40]. In order to more fully explore conduction to and through ZnO, we studied the carrier concentration and band gap of electrodeposited ZnO, linking these traits to their current-voltage behaviour (Chapter 5)[42]. This work is described in Chapter 5, and is currently under peer review for publication. In Chapter 6 we studied the effect of relative humidity on ZnO/metal junctions, and how conformal hydrophobic coatings

can improve the functionality of these junctions under high-humidity conditions[41].

Chapter 7 reports on multi-layer semiconductor studies that we have undertaken. One of the main goals of recent semiconductor research has been the production of higher efficiency solar cells[18, 43, 44]. We used the knowledge gained from our ZnO studies to create ZnO/Cu_2O *pn* junctions. Cu_2O a is non-toxic direct energy gap material ($E_g = 2.0 - 2.2$ eV) with *p*-type conductivity in its native form due to copper vacancies[45, 46]. Like ZnO, its constituent salts are readily available and of low-toxicity[46]. Cu_2O has been used for semiconducting devices in the past, such as solar cells[46], rectifiers[47], and electroluminescent diodes[48]. Our studies focused on the light sensitivity of ZnO/Cu_2O junctions for potential photovoltaic applications.

Chapter 8 puts our synthesis and device prototype studies into context. I show how this thesis work can be applied to other areas of semiconductor physics, and suggest some avenues of research that can now be explored because of our advances.

Chapter 2

Background

To explore and understand how electrodeposited semiconductor heterojunctions behave when a voltage is applied across them, it is important to understand how the junctions are produced and the measurement technologies available to assess their electrical responses.

2.1 Electrodeposition

2.1.1 Electrochemical Synthesis

In order to determine the conditions required for the electrosynthesis of any material, we can begin by considering the stability of the target material in aqueous solution. A Pourbaix diagram indicates the pH and potential values at which chemical species are stable in aqueous solution. These pH/potential phase plots are thermody-

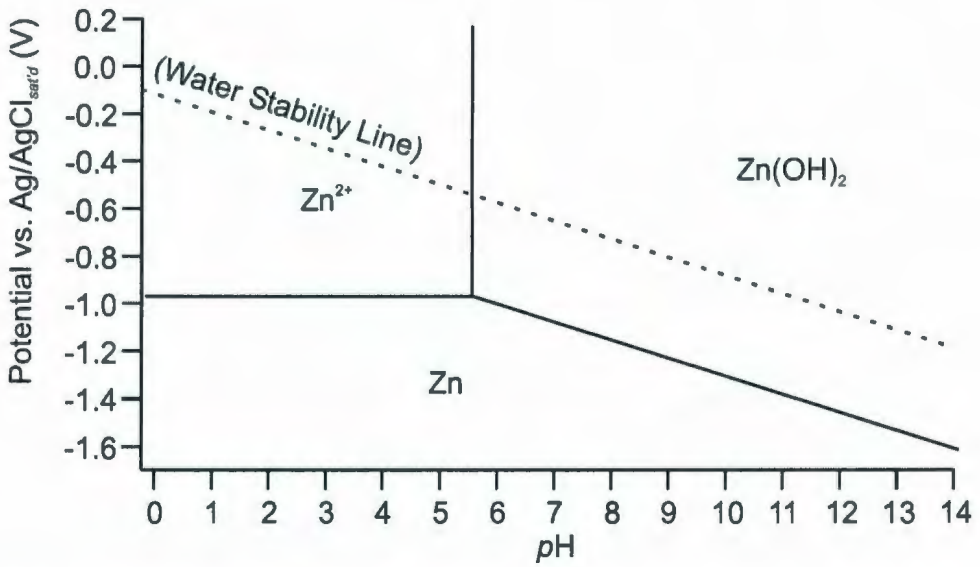

Figure 2.1: Diagram indicating the potentials and pH regions at which Zn^{2+}, Zn, and $Zn(OH)_2$ are stable. These schematic diagrams are based on thermodynamic calculations of phase stabilities at STP (25°C and 1 atm). They are used as general guidelines when determining synthesis conditions, as they do not include the effect of supporting electrolytes, temperatures and pressures other than STP, electrode stability, *etc.* The dashed lines indicate the lower limits of stability for water; below the dashed line, hydrogen gas will be evolved.

namic calculations of the stability of the metal oxides, metal hydroxides, and metal ions in water[49]. A simplified version of the Pourbaix diagram for Zn^{2+}, Zn, and $Zn(OH)_2$ at 1 atm and 25°C can be seen in Figure 2.1.

The standard potentials for electrochemical reactions shown on the ordinate axis in a pH-potential phase diagram (Pourbaix diagram) are measured relative to the potential difference between the working electrode, at which the reaction occurs, and a reference electrode. This thesis will report against the $Ag/AgCl_{sat'd}$ potential unless otherwise noted. Potential is applied with an external power supply (Described in Chapter 3), and the pH is varied with the addition of acids (i.e. HCl) or bases (i.e.

NaOH) as noted. Care must be taken when choosing pH modifiers, as unintentional effects such as extrinsic doping with Cl^- can occur in ZnO[10].

The phase boundaries in a Pourbaix diagram indicate reduction/oxidation (redox) reactions that can occur during an electrochemical experiment. Such reactions can be written as a redox couple,

$$O + ne^- \rightleftarrows R, \tag{2.1}$$

where O is the oxidized species, R is the reduced species, and n is the number of electrons transferred per reaction[50]. At potentials more negative than the standard reaction potential ($E°$), the reductive formation of O is more favoured, while at potentials more positive than $E°$ the oxidative formation of R is favoured[50, 51].

A straightforward example is the reduction-oxidation of zinc metal (Zn^0) and the zinc ion (Zn^{2+}), for which the standard potential is -0.962 V *vs.* $Ag/AgCl_{sat'd}$.[52]

$$Zn^{2+}_{(aq)} + 2e^- \rightleftarrows Zn_{(s)} \tag{2.2}$$

At potentials more negative than -0.962 V *vs.* $Ag/AgCl_{sat'd}$, the formation of the reduced species (Zn^0) is more favourable, while above this potential Zn^{2+} is more favourable. If a redox reaction occurs at a high enough rate that it can be considered to be in thermodynamic equilibrium as the potential is swept, it is considered a reversible reaction. Such a system can, in principle, be reduced and oxidized an infinite number of times without adverse affect (no loss of O or R). Zinc metal deposition is

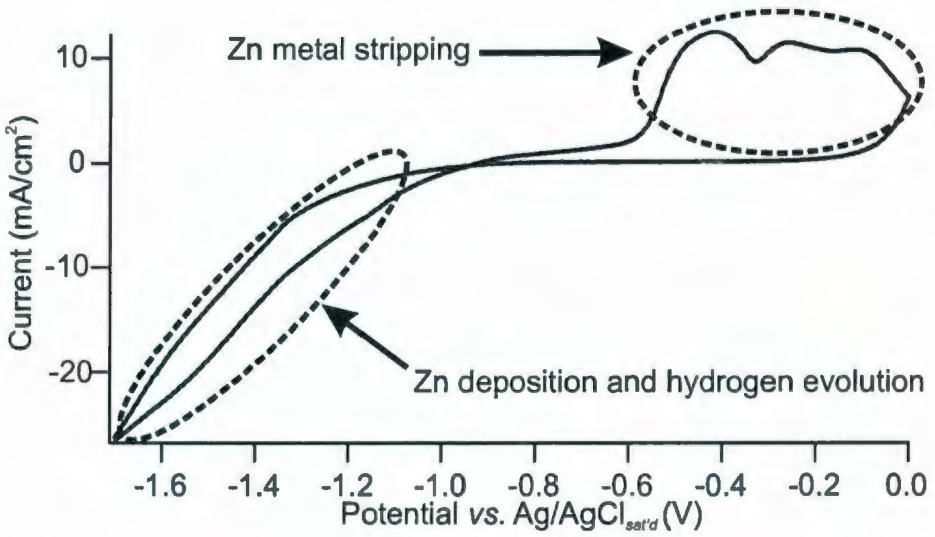

Figure 2.2: This cyclic voltammogram illustrates a reversible reaction. The peak at more negative potentials is due to both Zn metal deposition and hydrogen evolution. The peak at more positive potentials corresponds to stripping of electrodeposited Zn metal. This CV was performed on a gold working electrode in 0.02 M $Zn(NO_3)_2$.

an example of a reversible reaction. A cyclic voltammogram (CV) of the reversible zinc metal deposition can be seen in Figure 2.2. A CV is collected by sweeping an applied potential across the working electrode and reference electrode and recording the current response. Current peaks in a CV indicate movement of charge at or near the working electrode surface.

2.1.2 Zinc Oxide Electrodeposition

In contrast to simple redox reactions, there are electrodeposition reactions that are not reversible. For example, metal oxide deposition can involve the formation of intermediate species such as metal hydroxides. The electrochemical synthesis of metal oxides can be achieved by several different techniques, such as electromigration

of reactant species, electrolysis of fused salts, anodic oxidation, alternating current synthesis, or cathodic reduction[53]. For our ZnO electrodeposition experiments, we used cathodic reduction exclusively.

Cathodic reduction often utilizes the production of an alkaline species at the surface of an electrode to hydrolyze metal ions and metal complexes. This hydrolysis forms metal oxides and hydroxides either in solution or at the surface of the working electrode. Therese *et al.*[53] reviewed this technique and report many of the metal oxides that can be synthesized in this way, including TiO_2, ZrO_2, Cr_2O_3, and $LaMnO_3$. Direct cathodic reduction of metal ions and metal complexes to metal oxides, such as Cu_2O[45, 54, 55, 56, 57], CeO_2[58], and Tl_2O,[58] has also been reported.

We electrodeposit zinc oxide samples using a multi-step process facilitated by a nitrate reduction reaction first reported by Izaki *et al.*[59].

$$Zn(NO_3)_2 \rightarrow Zn^{2+} + 2NO_3^- \tag{2.3}$$

$$NO_3^- + H_2O + 2e^- \rightarrow NO_2^- + 2OH^- \tag{2.4}$$

$$Zn^{2+} + 2OH^- \rightarrow Zn(OH)_2 \tag{2.5}$$

$$Zn(OH)_2 \rightarrow ZnO + H_2O \tag{2.6}$$

This reaction includes the reduction of NO_3^- to NO_2^- at the working electrode surface, creating an alkaline environment in the immediate vicinity that promotes the formation of $Zn(OH)_2$. ZnO then forms on the surface of the working electrode as the precipitated $Zn(OH)_2$ decomposes. It is thought that this reduction reaction is catalyzed by Zn^{2+} ions adsorbed on the surface of the working electrode[60], similar to the catalytic effect of Zr^{4+} and La^{3+} on nitrate reduction reported by Cox *et al.*[61]. The effect of the nitrate reduction reaction at the surface of the working electrode can be seen in the annotated Pourbaix diagram in Figure 2.3, which shows the need for a high pH to form $Zn(OH)_2$[49].

The choices of potential and pH ranges for ZnO electrodeposition in this thesis were guided by the Pourbaix diagram seen in Figure 2.1. Deposition temperature was set at $70 \pm 4°C$, in order to be safely above the temperature needed to decompose $Zn(OH)_2$ into ZnO[62], while reducing the effect of electrolyte evaporation. The Pourbaix diagram for this system was not significantly affected by the higher deposition temperatures and complexing agents[63].

Only a portion of the current through our electrochemical cell is due to the primary cathodic reduction reaction, and its magnitude is heavily dependent upon the concentration of Zn^{2+} and NO_3^{2-} within solution[50]. Other reactions contribute to a background current, including the evolution of hydrogen at the electrode surface. At potentials more negative than -0.630 V *vs.* $Ag/AgCl_{sat'd}$, at pH =5, water will be electrolyzed[49, 16]:

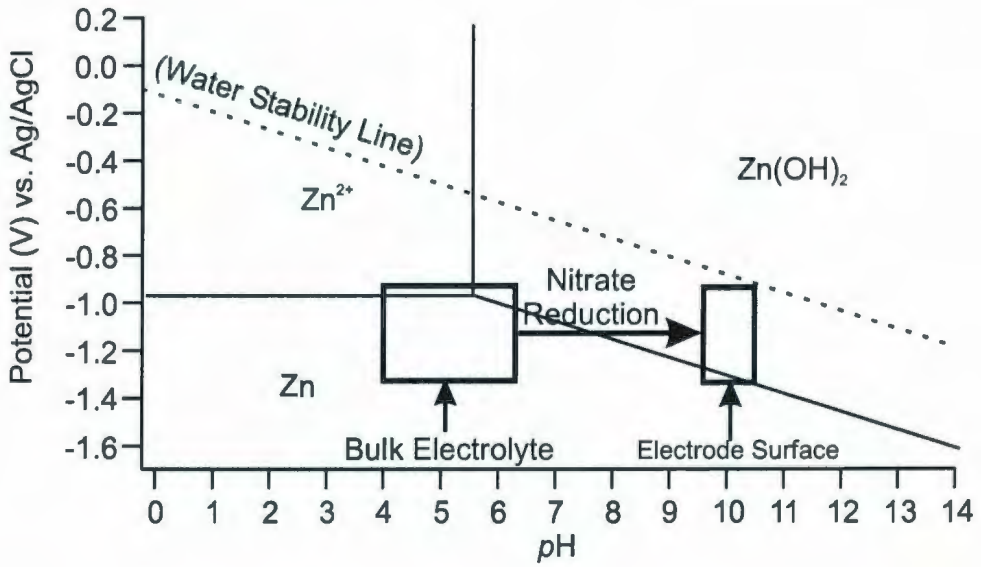

Figure 2.3: This annotated Pourbaix diagram indicates the effect of nitrate reduction on the electrolyte pH at the surface of the working electrode. This increase in pH facilitates the formation of $Zn(OH)_2$ which thermally decomposes to ZnO. The area labeled "Electrode Surface" is an estimate of the pH at the surface of the working electrode due to the nitrate reduction. No data have been reported on the exact pH at the surface of the working electrode.

$$2H_2O + 2e^- \rightleftharpoons H_2 + 2OH^-. \tag{2.7}$$

This reaction occurs in parallel with ZnO formation. Below, we discuss how the evolution of hydrogen during the formation of ZnO can affect its electrical properties. Contamination of the electrodeposited samples by other *in situ* species must be considered carefully. While there is no evidence of either the nitrate or nitrite supporting ions incorporating in ZnO (both molecules are too large), Cl^- present in acidic electrolytes can incorporate into ZnO[10]. The majority of our electrodeposits were made in chloride free electrolytes (unless otherwise noted), eliminating this concern. Sodium ions from the NaOH have never been found to incorporate into ZnO.

2.2 Conduction in Semiconductors

2.2.1 Semiconductor Doping

The novel electrical conduction characteristics of semiconducting materials have garnered much attention since their discovery. A common way to distinguish semiconductors from metals and insulators is by comparing their electrical resistivities at room temperature. Semiconducting materials typically have resistivities between 10^{-1} and $10^{-2}\ \Omega \cdot m$, which are higher than the $10^{-8}\ \Omega \cdot m$ for copper metal but lower than the $10^{17}\ \Omega \cdot m$ for fused quartz (a good insulator)[64]. The energy required to

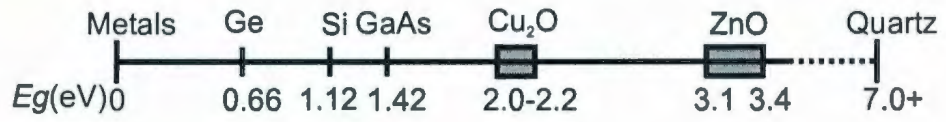

Figure 2.4: This schematic diagram illustrates the relative magnitudes of the band gaps of some common semiconductors compared to metals and insulators (such as quartz).

move an electron from the valence band to the conduction band (E_g), lie in the range of 0.5 eV to 3.5 eV for semiconductors[65, 66, 67]. Some typical semiconductors used in electrical devices are silicon (E_g=1.12 eV), germanium (E_g=0.66 eV), and gallium arsenide (E_g=1.42 eV)[65]. Figure 2.4 illustrates the range of band gaps for these semiconductors.

An important way to control the band gap of (and conduction through) a semiconductor is by dictating the concentration and type of dopants within the crystal structure. Adding impurity atoms to create n-type (majority electron carriers) or p-type (majority hole carriers) semiconductors allows tailoring of a material's electrical response. Ideally, atomic substitution can increase the electron or hole density, but in real systems the doping can be much more complicated due to compensating defects, vacancies, interstitials, and phase segregation[65].

2.2.2 Native Doping of Semiconductors

ZnO's natural n-type conductivity is an example of a system where the excess negative charge carriers are incorporated during synthesis, often unintentionally. The source of ZnO's native conductivity has recently been debated in literature[13, 14, 15],

since it had long been thought that the n-type doping was due to both interstitial zinc atoms and oxygen vacancies. Recent studies have shown that hydrogen interstitial doping plays a much larger role than previously thought. Hydrogen is present during all ZnO synthesis techniques, even in ultra high vacuum. Due to its high mobility, hydrogen can easily diffuse into the material during synthesis and has been detected in ZnO prepared by many methods[16, 68, 69, 70, 71, 72]. In most semiconducting materials, incorporated hydrogen is amphoteric, counteracting the dominant source of conduction[73]. Indeed, hydrogen has been found to passify nitrogen dopants added to ZnO[74]. It is generally agreed that electronically active interstitial H^+ ions routinely exist in ZnO[12, 73, 75]. First principles studies have shown that this incorporated hydrogen acts as a shallow donor, with an ionization energy of 30 meV or less[12], and experimental results have confirmed this finding[76]. Hydrogen that has diffused into ZnO loses its electron to the conduction band of the crystal due to its low ionization energy[12, 73, 75]. Depending on the amount of hydrogen diffused into ZnO during synthesis, n-type doping occurs with electron concentrations of $\sim 10^{16} - 10^{21} \mathrm{cm}^{-3}$[15, 17, 20]. Earlier work from our group has shown that deposition potential can be used to influence hydrogen evolution rate and subsequently the doping level in electrodeposited ZnO samples[16].

2.3 Direct Current Responses

2.3.1 Ohmic and Rectifying Junctions

For device applications, it is imperative to control electrical conduction to and through semiconductor/metal junctions. The materials described in this thesis involve two basic types of contacts: resistive and rectifying. Resistive contacts are governed by Ohm's law, wherein the current through a junction is linearly dependent upon the applied voltage and the DC resistance, as seen in Equation 2.8:

$$V = IR \tag{2.8}$$

In contrast, many semiconducting junctions show non-linear current-voltage (I-V) behaviour. Rectifying contacts act like one way valves for electrons, conducting well in one direction and poorly in the opposite direction. In my thesis work, I focus on rectifying Schottky junctions (a junction between a semiconductor and a metal), though I do briefly explore rectifying *pn* junctions (a junction between an *n*-type semiconductor and a *p*-type semiconductor).

The Mott-Schottky theory describing the conditions leading to rectifying semiconductor/metal junctions was developed by Walter H. Schottky and Neville Francis Mott in the mid-twentieth century. Rectification often occurs at the interface between an *n*-type semiconductor and a metal due to the difference between the Fermi energy levels in the two isolated materials. Due to the position of the charge carriers in

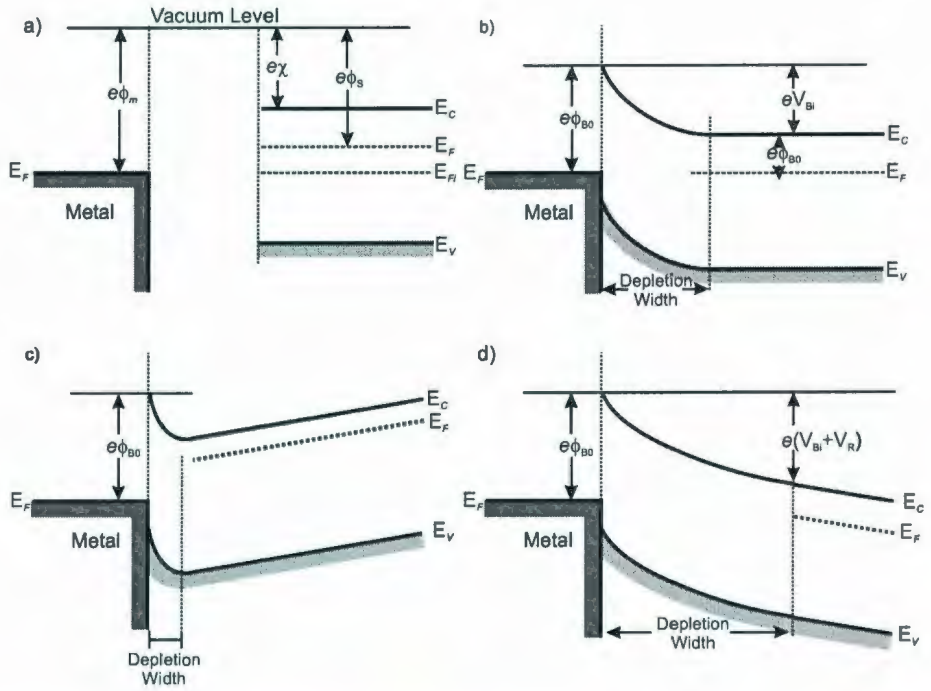

Figure 2.5: Energy band diagram of a semiconductor/metal Schottky junction before coming into contact (a), after achieving equilibrium (b), under forward bias voltage (c), and under reverse bias voltage (d). Note the formation of the Schottky barrier (Φ_{B0}), built-in plus reverse bias voltage ($V_{bi} + V_R$), and depletion width (W).

their valence band p-type materials typically do not have the band structure needed to create a Schottky barrier[65]. When an n-type semiconductor comes into contact with a metal, the negative charge carriers near the junction move into the metal to occupy the many available lower energy states. This serves to equilibrate the junction and to make the Fermi energy continuous across the whole system. The excess positive charge in the semiconductor occupies a volume that is relatively depleted of charge carriers (space charge region or depletion zone) as can be seen in Figure 2.5. As a result, two barriers are created that impede the flow of electrons: the Schottky barrier and the built-in potential.

The Schottky barrier, Φ_{B0}, is the potential barrier encountered by electrons in the metal incident upon the metal/semiconductor interface,

$$\Phi_{B0} = \Phi_m - \chi_s, \tag{2.9}$$

where Φ_m is the work function of the metal and χ_s is the semiconductor's electron affinity. Values for the work function and electron affinity of materials discussed in this proposal are $\sim$ 5 eV (see Table 2.1) and Schottky barriers are $\sim$ 1 eV; for example, Equation 2.9 gives a Schottky barrier height of 1.4 eV for ZnO/Au.

Electrons in the semiconductor incident upon the semiconductor/metal interface encounter a barrier called the built-in potential, V_{bi},

$$V_{bi} = \Phi_{B0} - \frac{kT}{e}\ln\left(\frac{N_c}{N_d}\right), \tag{2.10}$$

where k is Boltzmann's constant, T is the absolute temperature, e is the fundamental charge, N_c is the effective density of states in the conduction band, and N_d is the density of donor impurity atoms. The built-in voltage is the measurement of the potential height difference between the conduction band at the ZnO/substrate junction and at the end of the depletion width (Figure 2.5). It can be derived from the change in potential across the depletion width, and the inherent electric field caused by the potential difference. The built-in electric field opposes the travel of electrons into the metal after thermal equilibrium has been achieved.

The depletion width created during the formation of the Schottky junction,

Metal	Φ_m(eV)	Semiconductor	χ_s(eV)
Au	5.1[65]	ZnO	3.7[77, 78]
Pt	5.7[65]	Cu_2O	1.1[79]
Zn	4.4[65]		

Table 2.1: Work function and electron affinity values for selected materials.

$$W \approx x_n = \frac{2\epsilon_s(V_{bi} + V_R)}{eN_d}, \tag{2.11}$$

extends almost exclusively into the semiconductor due to the relative imbalance in carrier concentrations ($N_a \gg N_d$, where the number of acceptor carriers, N_a, is the number of unfilled states in the conduction band of the metal). The Schottky junction depletion width is determined by the dielectric constant of the semiconductor (ϵ_s), the donor carrier concentration (N_d), the applied reverse bias voltage V_R, and the built in potential. As a result of this relation, semiconductors with lower carrier concentrations have larger depletion widths. The depletion width can also change dramatically with applied voltage.

When a positive (reverse bias, $V = V_R$) voltage is applied to the semiconductor, the built-in potential height (V_{bi}) increases by V_R, increasing the depletion zone width (Figure 2.5d), and impeding electron flow across the junction. If a negative (forward bias) voltage is applied to the semiconductor, the built-in barrier height will be reduced by the applied voltage and the depletion width will be reduced. Current flow from the semiconductor into the metal will occur, and the resulting current will

follow an exponential function with increasing applied potential

$$J = \frac{4\pi e m_n^* k^2}{h^3} T^2 \exp\left(\frac{-e\phi_{B0}}{kT}\right)\left[\exp\left(\frac{eV_a}{kT}\right) - 1\right], \tag{2.12}$$

wherein J is the current density (cm/s^2), m_n^* is the electron's effective mass (2.551×10^{-31}kg for ZnO[80]), h is Planck's constant (eV·s), and V_a is the applied bias voltage. In real systems (and where $V_a > 3kT/e$ and $\exp(eV_a/kT) \gg 1$), Equation 2.12 is modified to

$$J = \frac{4\pi e m_n^* k^2}{h^3} T^2 \exp\left(\frac{-e\Phi_{B0}}{kT}\right) \exp\left(\frac{e(V_a)}{nkT}\right), \tag{2.13}$$

which includes an ideality factor n that indicates how close the non-linear curve is to the ideal exponential response. Idealities > 1 can occur when there are multiple electron conduction pathways, interfacial states, or the presence of deep recombination centers[81].

Schottky barriers formed between high purity metals (such as Au, Pt, and Cd) and single crystal ZnO layers have been vigourously studied in recent literature[17, 25, 82, 83, 84]. These studies have shown that the predictable creation of Schottky barriers is non-trivial. A unifying theme of these studies is to improve Schottky barrier height, ideality, leakage voltages and break-down voltages by using secondary processes such as sulfide treatments[85], H_2O_2 treatments[86], ozone cleaning[19], eximer laser irradiation[20], and hydrogen plasma doping[87]. The ideal Schottky junction would have a barrier height on the order of 1 V, with very repeatable I–V char-

acteristics. Optical devices benefit from very well structured interfaces, which have idealities of ≈ 1. Schottky barrier heights reported for ZnO-based junctions are 0.6-1.0 eV, leakage currents range from 1 nA to 100 mA, break-down voltages are ~ 5 V, and idealities range from 1 to ~ 10. Junctions with these characteristics are considered usable for some Schottky response based devices. In some device applications the I–V characteristics need not follow the ideal Schottky diode equation as long as the I–V characteristics are repeatable and suitably rectifying. ZnO Schottky junctions have been proposed for devices such as diodes[25], hydrogen sensors[84, 88], ultraviolet photodetectors[89], photodiodes[25], and ultraviolet light-emitting diodes[90].

2.4 Mott-Schottky Analysis

As mentioned above, carrier concentration can have a strong impact on a junction's electrical conduction properties. To determine carrier concentration, we use an alternating current technique (Mott-Schottky analysis) that utilizes the capacitance of a Schottky junction in reverse bias.

Mott-Schottky analysis exploits the charge separation in one-sided junctions, wherein one side has a much higher carrier concentration than the other. This condition is met in both semiconductor/metal Schottky junctions and p^+n junctions[65]. Like a typical two-sided junction, a one-sided junction in equilibrium has positive and negative charge separated by a depletion zone (W) created by the Fermi energy equalization across the junction. In a pn junction with the same carrier concentra-

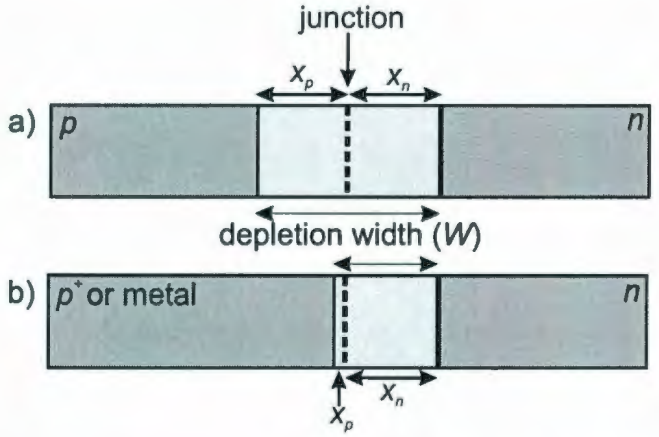

Figure 2.6: This diagram illustrates the doped regions of a pn junction (a) and a one-sided junction (b). The depletion width ($W = x_p + x_n$) extends equally into both the p and n sides of the junction when their carrier concentrations are equal ($N_a = N_d$). In a one-sided junction, the depletion width is almost completely within the material with the lower carrier concentration. $W \approx x_n$ in both p^+n and Schottky junctions, where $N_a \gg N_d$.

tion on both sides, the depletion width in the n-type side (x_n) and p-type side (x_p) are equal. However, the depletion zone in a one-sided junction is almost completely contained within the low carrier concentration side ($W \approx x_n$), as seen in Figure 2.6. The charge separation across the depletion width creates an associated capacitance. When a reverse bias is applied to a Schottky junction (semiconductor positive with respect to the metal), the depletion width will grow as electrons are removed from the semiconductor at the connection opposite the Schottky junction. As the depletion width increases more positive charge is uncovered in the semiconductor (Equation 2.11), which results in a voltage dependent junction capacitance (C).

$$C = a\frac{dQ}{dV_R} = a\frac{d(eN_d x_n)}{dV_R} = aeN_d\frac{dx_n}{dV_R} \tag{2.14}$$

Here, dQ (C) is the amount of charge uncovered during the application of dV_R (V) reverse bias (R denotes semiconductor is positive (reverse bias)), a (cm^2) is the area of the junction, e is the elemental charge (C), N_d is the carrier concentration (cm^{-3}), and dx_n (cm) is the change in depletion width in the n-type material. The charge uncovered in the n-type region of the depletion width is:

$$x_n = \sqrt{\frac{2\epsilon_S(V_{bi}+V_R)}{e}\frac{N_a}{N_d}\frac{1}{N_a+N_d}}, \tag{2.15}$$

wherein ϵ_S is the dielectric constant of the semiconductor, and N_a and N_d are the p-type and n-type carrier concentrations, respectively. By differentiating Equation 2.15, with respect to the reverse bias voltage, Equation 2.14 can be expressed as:

$$C = \sqrt{\frac{a^2 e\epsilon_S N_a N_d}{2(V_{bi}+V_R)(N_a+N_d)}} \tag{2.16}$$

In the case of a one-sided Schottky junction with an n-type semiconductor, where $N_a \gg N_d$, Equation 2.16 reduces to:

$$C = \sqrt{\frac{a^2 e\epsilon_S N_d}{2(V_{bi}-V_R)}} \tag{2.17}$$

By expressing this relationship as C^{-2} *vs* V_R we have a function that is linear with respect to applied bias[91]:

$$\frac{1}{C^2} = \frac{2}{e\epsilon_0\epsilon_r N_d a^2}(V_R - V_{bi} - \frac{kT}{e}). \tag{2.18}$$

Here C is the capacitance, ϵ_0 is the permittivity of free space, ϵ_r is the relative dielectric constant, a is area of the contact, V_R is the applied voltage, V_{bi} is the built-in potential, k is the Boltzmann constant, and T is the absolute temperature.

To measure junction capacitance in the lab, an alternating potential ~ 10 mV is imposed over a DC potential to determine the impedance of a one sided junction. The capacitance of the junction can be found by using straight-forward impedance/capacitance relationships. Junction impedance can be determined using the frequency dependent formulation of Ohm's law:

$$E_t = I_t Z, \tag{2.19}$$

wherein E_t and I_t are the alternating current equivalents of V and I respectively:

$$E_t = E_0 \sin(\omega t) = E_0 e^{i\omega t} \tag{2.20}$$

$$I_t = I_0 \sin(\omega t + \phi) = I_0 e^{i(\omega t - \phi)}. \tag{2.21}$$

Here E_0 and I_0 are the amplitude of the sinusoidal applied potential and the resulting current, ω is the angular frequency of the applied AC potential, and ϕ is the phase constant in radians. By substituting into Equation 2.19, and rearranging to find the impedance, we can see that:

$$Z = \frac{E_t}{I_t} = \frac{E_0 \sin(\omega t)}{I_0 \sin(\omega t + \phi)} = Z_0 \frac{\sin(\omega t)}{\sin(\omega t + \phi)} \tag{2.22}$$

The impedance can also be expressed in complex form:

$$Z = \frac{E_0 e^{i\omega t}}{I_0 e^{i(\omega t - \phi)}} = Z_0 e^{i\phi} = Z_0(\sin(\phi) - i\cos(\phi)) \tag{2.23}$$

The capacitance of a system can be determined from AC impedance at each applied frequency. During Mott-Schottky analysis we determine the capacitance of a system by using the equation:

$$Z = \frac{1}{j\omega C}, \tag{2.24}$$

at different applied DC voltages. The junction capacitance determined from impedance data can be plotted as C^{-2} *vs.* V_R. By rearranging Equation 2.18 into the form:

$$\frac{1}{C^2} = \left(\frac{2}{e\epsilon_0\epsilon_r N_d a^2}\right) V_R - V_{FB}. \tag{2.25}$$

A linear regression of the C^{-2} *vs.* applied reverse voltage plot will yield values for N_d and V_{FB}.

This technique can be undertaken using either dry samples or samples immersed in liquid. It order for the Mott-Schottky method to elicit useful data, the Schottky junction must be as close to ideal as possible ($n \approx 1$). Any parallel conduction pathways

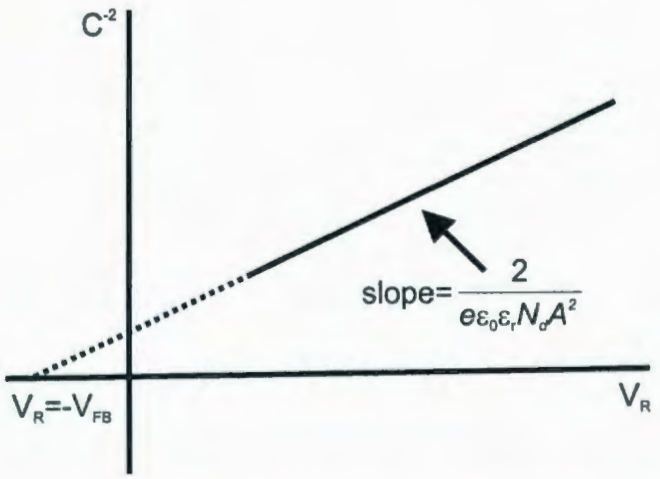

Figure 2.7: This diagram illustrates the ideal Mott-Schottky relation for a one-sided junction. Linear regression analysis of this plot using Equation 2.25 can elicit N_d and other characteristics of the one-sided junction.

would perturb the linearity of the Mott-Schottky C^{-2} *vs.* V_R theory. While determining the contact materials for making effective dry contact is relatively straightforward, deciding on an electrolyte for the liquid contact is more difficult. The electrolyte must not cause extensive damage to the semiconductor (*i.e.*, through dissolution), nor can it be electrochemically active at the DC potentials applied. It must also conduct well enough so that the depletion layer forms properly at the semiconductor/electrolyte interface. These challenges are compounded by the existence of extra capacitances, such as the geometric double plate capacitance inherent in the dry method and the addition of a double layer capacitance in the solution method[92].

Chapter 3

Experimental Methods

To understand how junction formation affects the electrical response of semiconductor heterojunctions, we adapted existing electrodeposition techniques to synthesize metal oxide semiconductors. Phase identification techniques were used in conjunction with the electronic and optical properties, morphologies, and roughnesses to characterize our thin film semiconductors.

3.1 Semiconductor synthesis

3.1.1 Apparatus

The electrodeposition experiments in this thesis were performed in a Pyrex cell that was designed and modified in our lab (Figure 3.1). A Teflon top secured a variety of electrodes and probes necessary for a controlled deposition procedure. The

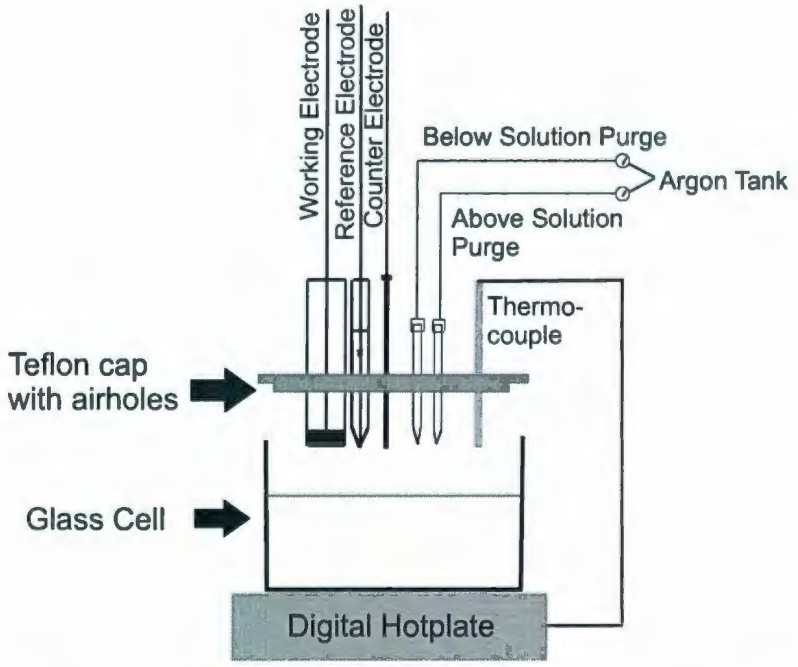

Figure 3.1: Schematic diagram of the setup used for the electrodeposition of semiconductors during this thesis. This is a practical adaptation of a traditional setup, as described by Bard and Faulkner[50].

working electrode (WE) was the surface on which the semiconductor films formed. A potential was applied to the WE, relative to the $Ag/AgCl_{sat'd}$ reference electrode (RE), with a Hokuto Denko HA501 potentiostat. A gold counter electrode (CE) was used to allow conduction through the cell.

A potentiostat is the primary device used to control the potential of a three electrode (WE, CE, and RE) electrochemical cell. It utilizes an amplifier to automatically match the potential between the working electrode and the reference electrode to an applied input voltage. An amplifier feedback circuit works by determining the impedance of the electrochemical cell and controlling the current flow between the

working electrode and the counter electrode. By doing so, the potentiostat controls the potential between the working electrode and the reference electrode, matching it to the input voltage.

Using a K-type thermocouple, we maintained a targeted electrolyte temperature to within ±4°C. To reduce the amount of dissolved oxygen in the solution, one purge tube was used to cover the electrolyte in an inert gas (argon or nitrogen), while the second was used to bubble an inert gas through the electrolyte.

A Hokuto Denko coulombmeter (HF 201) counts the charge passed between the WE and the CE. Analog data from the potentiostat were digitized using a National Instruments BNC 2090 input connected to a National Instruments NI 6502E analog/digital converter board in a desktop PC. Data are recorded using a virtual instrument (VI) originally written by Bizzotto *et al.* for the LabVIEW 7.0 language[93], and modified by various members of the Poduska research group.

3.1.2 Substrate Preparation

All semiconductor films described here were formed on polycrystalline conducting substrates: corrosion resistant stainless steel (316 series or A-286 series steel alloy), Au/Cr/glass, In_2O_3:SnO_2/glass (ITO), or platinum. Steel surfaces were polished using 1500 grit (350,000 grains per cm^2, ≈ 1.7 μm diameter grains) alumina sandpaper followed by sonication in ultrapure water (18.2 M$\Omega \cdot$ cm, Barnstead Nanopure). Au/Cr/glass (Erie Scientific; vapour-deposited 1250 Å of Au and 400 Å of Cr) and Pt

sheets (Alfa Aesar) were cleansed in 96% sulphuric acid (H_2SO_4). ITO/glass (Delta Technologies) was activated by sonication in acetone immediately prior to deposition. Structural studies (See Sections 3.2.1-3.2.2) reveal that there is no structural difference between samples deposited on different substrates, and SEM micrographs (See Section 3.2.3) indicate that the morphology is not substrate dependent.

3.1.3 ZnO Deposition

Our ZnO thin films were synthesized using a modified version of the procedure outlined by Izaki *et al.*[59], and used by our group previously[16]. An aqueous electrolyte of 0.01 M $Zn(NO_3)_2$ (ACS grade, SCP Science) with an initial *p*H of 5 was used for all ZnO syntheses. The *p*H of the electrolyte was adjusted to between 4.0 (by adding HCl) and 7.0 (by adding NaOH), (ACS grade, Sigma-Aldrich or SCP Science). Argon (Ultra High Purity Plus grade, Air Liquide) or nitrogen (High Purity grade, Air Liquide) was bubbled through the electrolyte to reduce the amount of dissolved oxygen. All electrolytes were prepared with ultrapure water (18.2 Ω·cm, Barnstead Nanopure).

The procedure for deposition was as follows. The substrate, counter electrode, reference electrode, and argon purge tubes were inserted into the electrolyte during heating. The electrolyte was heated to a temperature of 70°C to promote ZnO formation over $Zn(OH)_2$[62, 59, 94]. The working electrodes, including the thin stainless chromium oxide (Cr_2O_3) surface of the steel substrates, are stable in our *p*H-potential

regions, ensuring a consistent electrode surface[49]. The desired deposition potential, between -0.7 V and -1.5 V *vs.* $Ag/AgCl_{sat'd}$, was applied between the counter electrode and the reference electrode when the electrolyte reached the target temperature. Only then was the working electrode connected, in order to maintain control of the working electrode potential throughout the experiment.

During deposition, bubbles of the inert gas, hydrogen gas, or water vapour sometimes blocked the working electrode. Bubbles that did form were removed by agitating the electrolyte with a pipette. After a predetermined time (5-25 min) or a predetermined amount of charge (100-400 mC) had passed, the sample was removed, rinsed in ultrapure water, and dried under flowing argon gas to reduce post-deposition zinc hydroxide formation or the dissolution of the slightly soluble zinc oxide.

3.2 Characterization techniques

3.2.1 X-Ray Diffraction

One of the main analytical techniques used in crystallographic characterization is X-Ray Diffraction (XRD), which can enable phase identification, lattice constant determination, and particle size estimations. The principles of XRD analysis can be explained using the Von Laue formulation of scattering [66, 67], which assumes a crystal to be composed of a set of basis atoms placed on the sites **R** of a Bravais lattice. Each of these atoms reradiates in all directions the radiation incident upon

them. From this system, sharp diffraction peaks will only be seen at angles and wavelengths where constructive interference between scattered waves of neighbouring atoms occurs.

In order to analyze XRD data for the purpose of phase identification, we need to collect the peak heights and positions from a range of crystal lattice planes. Fortunately, we can analyze a large number of crystal orientations during a single diffraction experiment because the electrodeposited thin films reported here are polycrystalline and exhibit a large number of crystallographic orientations. In contrast, one diffraction scan of a single crystal film would show diffraction peaks from only a single set of diffraction planes (001, 002, 003, *etc.*).

By comparing the relative peak heights of our electrodeposits to those of a truly randomly oriented sample, it it possible to determine if there is a preferred orientation among the crystallites in the film. Quantitative analysis of preferred orientation is called texture analysis, which quantifies how much of a film exhibits the preferred orientation. Qualitative texture analysis was used in this research.

XRD data were collected on a Rigaku D/MAX 2200PC $\theta - \theta$ Powder Diffractometer (MUN Earth Sciences). Scan parameters are typically 15–85° 2θ, at a rate of 0.5°/minute with a step size 0.05° 2θ. In its simplest form, an X-ray diffractometer is composed of two components: an X-ray source, and a detector, as shown schematically in Figure 3.2. The X-ray source emits Cu-Kα (20 kV, 40 mA max) radiation at 1.5418 Å with a graphite monochromator. These X-ray photons diffract from a

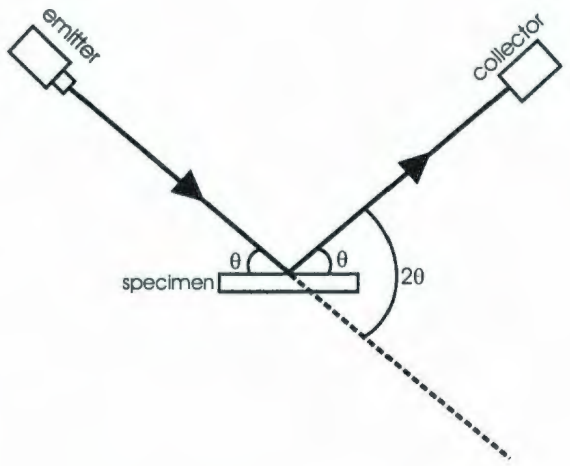

Figure 3.2: Schematic diagram showing a typical $\theta - \theta$ X-ray diffractometer.

specimen and are collected by a detector. The detector includes a beryllium window (to block superfluous radiation), a high linearity scintillation counter (such as a sodium iodide crystal), and a phototube. An X-ray photon that strikes the scintillation counter will excite an electron to a higher energy state, which then emits a photon as it returns to its ground state. The photon that is emitted is detected by a phototube, and the computer interface records the intensity and the detector angle. In a $\theta - \theta$ diffractometer, both the detector and emitter move, while the specimen is stationary. Consequently, the angle between the emitter and collector beam is 180-2θ. Bragg reflection from different families of lattice planes yields a plot of scattered X-ray intensity versus 2θ.

The diffraction patterns obtained in this thesis work were compared with the intensity and peak data from the Joint Committee for Powder Diffraction Studies

Table 3.1: Standard XRD pattern of ZnO, JCPDS #34 – 1451, for Cu Kα incident radiation (1.54 Å). Intensity is given as a relative percentage compared to the most intense (101) reflection [11].

2θ	Intensity (%)	(hkl)	2θ	Intensity (%)	(hkl)
31.770	57	(1 0 0)	66.380	4	(2 0 0)
34.422	44	(0 0 2)	67.963	23	(1 1 2)
36.253	100	(1 0 1)	69.100	11	(2 0 1)
47.539	23	(1 0 2)	72.562	2	(0 0 4)
56.603	32	(1 1 0)	76.955	4	(2 0 2)
62.864	29	(1 0 3)	81.370	1	(1 0 4)

(JCPDS), a database of experimentally determined X-ray diffraction patterns of over 160,000 crystalline materials [11]. The peak positions and intensities, such as those shown in Table 3.1 for ZnO, are used to confirm the material identity and possible preferred orientation. For example, a zinc oxide film that is made up of crystallites with a predominant (002) orientation would have a relative (002) peak intensity greater than 44%. Generally, a preferred orientation in a sample could be due to epitaxial growth, or other influences in deposit formation or preparation. This is not the case in our samples, as we exclusively use polycrystalline substrates. A (002) preferred orientation is often seen in samples deposited electrochemically[16, 39, 60, 95]. The level of crystallinity of our electrodeposits was determined by comparing the ZnO/substrate/holder XRD pattern to the substrate/holder patterns. No increase in broad low angle peaks from our samples was observed, indicating high levels of crystallinity.

3.2.2 Lattice Constant Refinement

One of the critical tasks faced during this thesis work was the proper phase identification of deposited films. By determining and comparing the lattice constants of electrodeposited samples, it is also possible to detect deviations from phase purity. The diffraction patterns of metal oxides often have diffraction peaks that overlap slightly with those of the constituent metal, such as zinc metal diffraction peaks overlapping those of zinc oxide. This overlap can shift the peak positions of the combined peak slightly, but it can be significant enough to stand out in a refinement of peak positions relative to the expected unit cell lattice constants.

Lattice parameter-refinement was performed using a freely-available DOS-based program, Prozski [96]. LATCON [97], a sub-program of Prozski, calculates the lattice parameters from user supplied peak positions using a simple non-iterative linear least squares fit of the data[98, 99]. Lattice constant refinements were performed on 5-6 diffraction peaks for each sample. No peaks were discerned from any materials other than ZnO and the substrate. Our XRD data is consistent with phase pure ZnO. However, it would be difficult to detect crystalline impurities of $< 5\%$ or amorphous phases with XRD analyses.

3.2.3 Scanning Electron Microscopy

The main technique used to analyze the morphology of deposited samples was scanning electron microscopy (SEM). While atomic force microscopy (AFM, men-

tioned below) can provide true topographic data, our samples have complex morphologies that can be difficult to assess due to tip-sample convolution effects. SEM is a common imaging tool that employs the emission of secondary electrons from the primary beam of focused electrons on the surface of a sample [100]. A thermionic or field-emission cathode is typically used as the electron source for such a microscope. The beam of electrons are accelerated by a potential difference between the cathode and the sample/anode. Secondary electrons ejected from the surface of the sample are collected, and correlated with the position of the raster scan, creating a scanning electron micrograph. The beam diameter ($\sim$ 10 nm) limits the spatial resolution. Excess charge buildup created by the electron beam can also limit spatial resolution, though our ZnO samples conducted reasonably well and did not require a gold coating to obtain good images.

A Hitachi S570 (MUN Biology/CREAIT) and a FEI Quanta 400 (Inco Innovation Centre/CREAIT) scanning electron microscopes were used to produce micrographs for this thesis. Magnification of up to 12000$\times$, corresponding to scans of 2 μm, were typically used for these analyses. The images are displayed on a video display in a raster scan that is synchronous with a scan across a sample, and captured digitally. These images, while reminiscent of an aerial photo, do not necessarily provide an accurate topographical representation. The gradient of the grayscale is based on two main characteristics: atomic number and conduction. Materials that conduct better or have higher atomic numbers appear lighter, while less conducting or lower atomic

number materials appear darker. Even though the conductivity of the films play an important role, atomic mass plays a greater role. The SEM micrographs were analyzed for crystallite homogeneity, crystallite size and habit.

3.2.4 Energy Dispersive X-Ray Analysis

Complementary to XRD data, energy-dispersive X-ray (EDX) analysis was used to determine the elemental composition of electrodeposits. In particular, this technique was used to confirm the presence of zinc and/or copper in electrodeposited samples and to confirm the absence of contaminant elements. EDX systems are commonly incorporated into SEM instruments [100, 101]. An electron beam, the beam utilized by the SEM, is focused on a sample, and facilitates the release of an X-ray photon from a sample. The energy of the X-ray ejected is dependent upon the type of atoms in the sample. In a typical EDX spectrometer, this photon will then pass through a beryllium window onto a lithium-drifted silicon detector. The beryllium window blocks electrons and longer wavelength photons (ultraviolet, visible, etc.) from entering the detector chamber. This silicon detector is a fast response [*p-i-n* (*p*-type, intrinsic, *n*-type)] semiconductor, reverse biased, and must be cooled with liquid nitrogen. A *pin* semiconductor junction is used to increase the sensitivity of the detector. By adding an intrinsically doped (i, where $N_a = N_d$) layer, the depletion width will be increased by the width of the i layer. This increased depletion width allows greater numbers of photons to be captured, thereby increasing sensitivity.

The electron beam focused on the sample causes the ejection of an electron, and the creation of an electron-hole pair in the sample. The vacancy left by the ejected electron will be filled by a electron from a higher energy level. To balance the energy loss of this electron, an X-ray will be emitted. The detector can determine the energy of the X-ray and the quanta of X-rays emitted from a sample. The data are then recorded and displayed, and are compared against known X-ray energies for all elements. Data acquisition is very fast, usually requiring less than two minutes to collect enough data to clearly distinguish constituent elements. A Tracor Northern EDX (MUN Biology/CREAIT) and a Roëntec Quantax EDX system employing the Xflash SDD detector (Inco Innovation Centre/CREAIT) were used in this thesis work. An example of EDX data of an iron oxide sample collected by the Northern Tracor system can be seen in Figure 3.3. Due to the age of the instrument, hard copies of EDX analysis on ZnO could not be printed from the Northern Tracor system. It was not possible to identify atoms with atomic weights below that of sodium with the Northern Tracor system or nitrogen with the Roëntec Quantax system.

There are two main limitations of EDX that are of concern in the characterization of zinc oxide. The first is that it cannot distinguish the ionic state of atoms, therefore it cannot distinguish between metal, metal oxide, and metal hydroxide phases. Secondly, the data peaks are not weight-normalized and so do not directly show relative amounts of atoms in a sample. It is possible to do a semi-quantitative analysis of these peak area, but this is a process that requires a standard sample with a pre-

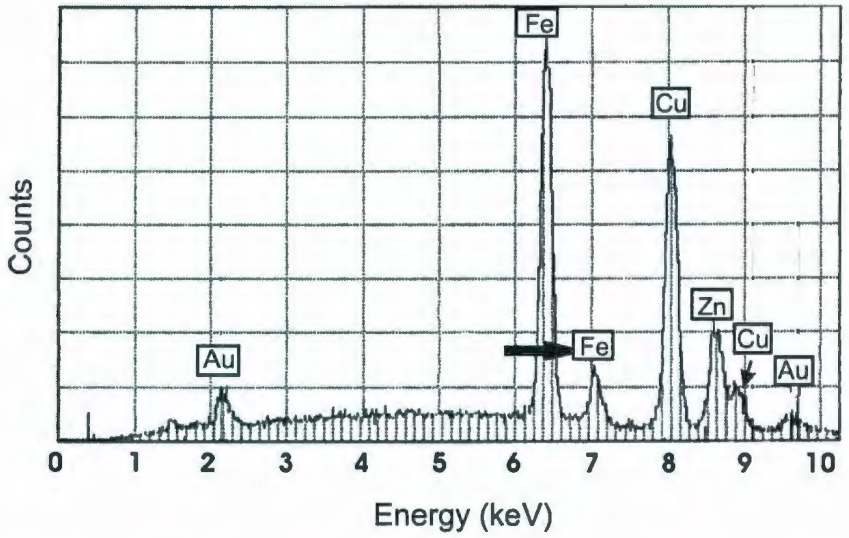

Figure 3.3: Typical EDX plot of an iron oxide sample deposited on brass collected with the Northern Tracor system. Peaks can be seen from the iron in the iron oxide, the copper and zinc in the brass substrate, and the gold that coats the sample to ensure proper conduction.

cisely known composition. Therefore, EDX was used only to qualitatively determine the elemental composition of samples, in order to detect any contamination of the electrodeposited thin films.

3.2.5 Diffuse Reflectance Spectroscopy

The optical response of electrodeposited samples are also used for phase confirmation. Collected spectra show a shift in the amount of reflected light with respect to the incident photon energy. At photon energies lower than the band gap, no electrons can be excited into the conduction band, resulting in reflection back to the collector. At photon energies greater than the band gap, most photons are absorbed. In a real system, the transition between absorption and reflection is not sharp, often

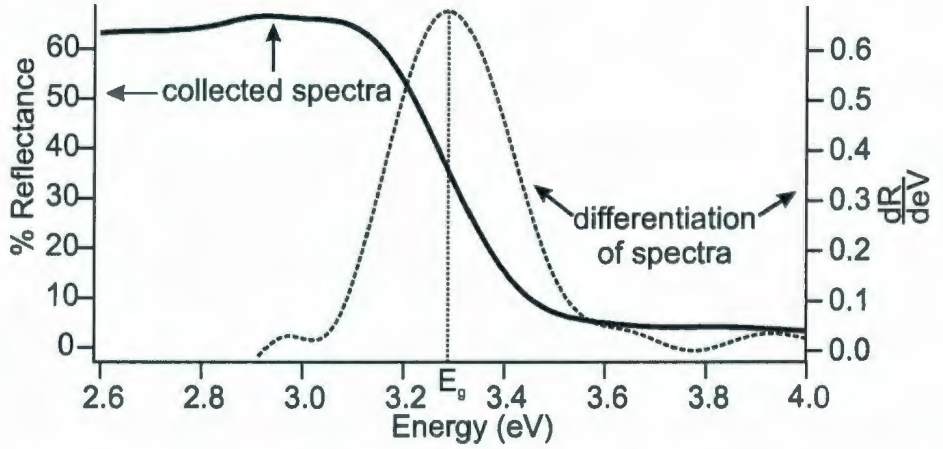

Figure 3.4: Representative UV/Visible diffuse reflectance spectra of a ZnO sample. Included is the differentiation of the raw spectra (dashed line). A Gaussian fit of the differentiated spectrum indicates the band gap energy.

due to local defects in the crystal lattice and variations in crystallite sizes[102]. Consequently, collected spectra are analyzed using a simple differentiation function (in reflection with respect to wavelength) to determine E_g[102]. The peak position of the differential spectra is taken as the band gap, (Figure 3.4).

UV/Visible reflectance data were collected using an Ocean Optics SD2000 spectrometer. An Analytical Instrument Systems Model DT 1000 CE UV/Visible light source is used to provide incident radiation from 275 nm to 700 nm (4.75 eV to 1.75 eV respectively). A 45° incident angle is used to illuminate the sample, with a co-linear reflectance collector. This setup was preferred over a transmittance setup because of the opaque substrates used during these experiments.

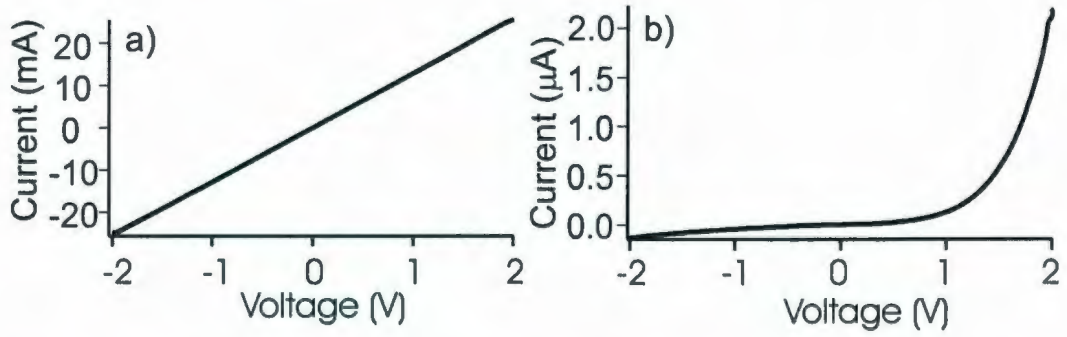

Figure 3.5: Representative I–V scans of an ohmic ZnO/metal junction (a) and a rectifying Schottky ZnO/metal junction (b) deposited with 0.01 M $Zn(NO_3)_2$ at -0.9 V and -1.1 V, respectively.

3.2.6 Current-Voltage Characteristics

The current flow as a function of applied voltage (I–V scans) of our electrodeposits were collected with one of tree instruments, a Hokuto Denko HA 501 potentiostat, a Princeton Applied Research EG&G potentiostat, or a Keithley 2400 source meter. The resulting data were recorded with customized LabVIEW interfaces (National Instruments). Connections were made to both the substrate and the electrodeposited layers using stainless steel compression contacts with a surface area of 0.18 cm^2. The data collected in the I–V scans were fitted to mathematical models, such as Equations 2.8 and 2.13, to assess film resistance and rectification properties. Examples of linear and rectifying I–V scans can be seen in Figure 3.5.

3.2.7 Mott-Schottky Analysis

Mott-Schottky (capacitance-voltage) analysis experiments were performed with a EG&G Princeton Applied Research 273A potentiostat in conjunction with a Sig-

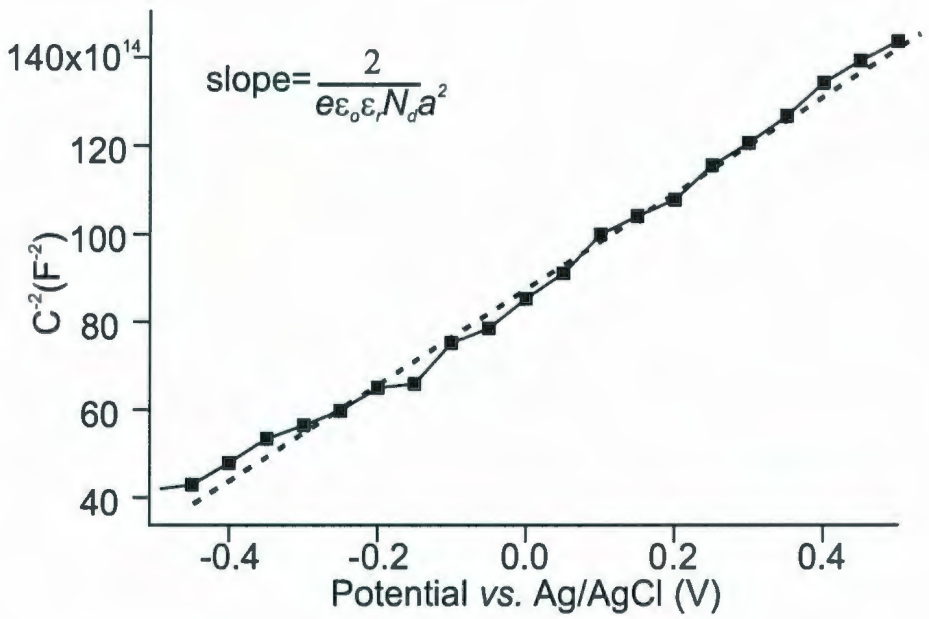

Figure 3.6: Representative Mott-Schottky data collected from a ZnO sample, performed in a *p*H 7 buffered electrolyte. The slope of the plot is inversely proportional to carrier concentration (N_d). V_R is measured *vs.* $Ag/AgCl_{sat'd}$.

nal Recovery 5210 lock-in amplifier. Alternating current voltages of 20 mV amplitude were superimposed over a direct current voltage ranging from -1.3 V to 1.3 V *vs.* $Ag/AgCl_{sat'd}$ at frequencies of 10-15 kHz. Data collection and potentiostat control were performed with PowerSUITE software (Princeton Applied Research). Further details of the analysis are given in Section 2.4. A representative Mott-Schottky plot can be seen in Figure 3.6. Linear regression analysis is only performed on the linear section of the graph. Outside the linear section, there is no charge separation movement due to the junction not being in reverse bias (applied voltage too negative) or the depletion width extending the entire width of the material (applied voltage too positive).

3.2.8 Atomic Force Microscopy

Atomic force microscopy (AFM, Asylum Research) was utilized to determine sample thickness and roughness. Height profiles can be collected by scanning a cantilevered Si tip (diameter $\sim$ 10 nm, CSC37/Cr-Au/50, μMasch), across the surface of a sample. As the tip is scanned along the surface of the sample, vertical features will change the deflection angle of the tip. This deflection changes the angle of a laser reflected from the back of the cantilever. The AFM uses the position of the reflected beam within a feedback loop to adjust the height of the cantilever base to maintain a constant force (the forced required to push the cantilever base towards the surface) on the cantilever. The adjustments of the base height translates into the topography of the samples. A simplified diagram of the AFM setup can be seen in Figure 3.7.

Sample thicknesses were determined by scoring the sample with a razor and finding the height difference between the substrate and the top surface of the deposit. Thicknesses were determined at sections along the score where ZnO has chipped off the substrate, ensuring that the height difference did not include any gouge caused by the razor (Figure 3.7 (c) and (d)). Most deposits showed thickness variations across the samples between 1 and 3 microns. This thickness range was confirmed in several cases with cross-sectional SEM.

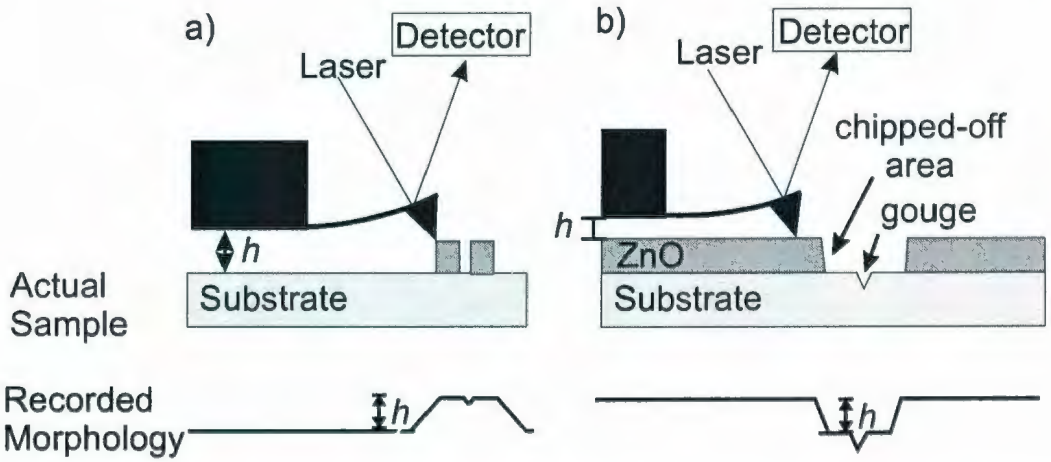

Figure 3.7: Schematic representation of an AFM tip in contact mode for (a) a single feature on a substrate and (b) a scored thin film. The height of the feature/film (h) is the amount that the cantilever base moves. Tip-sample convolution (a) reduces the accuracy of lateral height variation for a very rough surface. By taking the layer height at the site of a sample "chip", we avoid the gouge in the substrate from the razor score.

Chapter 4

Selective formation of ohmic junctions and Schottky barriers with electrodeposited ZnO

Reprinted with permission from Chatman, S.; Ryan, B. J.; Poduska, K. M., *Appl. Phys. Lett.* **2008**, 92, 012103/1-3, doi:10.1063/1.2828702, Copyright 2008, American Institute of Physics. (Some sections have been modified to fit this format.)

4.1 Abstract

Constant-potential electrochemical synthesis of ZnO on metal substrates enables selective formation of either ohmic or Schottky-barrier contacts. Using a mildly acidic

nitrate-based aqueous electrolyte, there is a substrate-dependent deposition potential below which electrodeposited ZnO heterojunctions display Schottky response with high contact resistances ($\sim 10^5\ \Omega$), and above which ohmic behavior and low contact resistances ($\sim 1\ \Omega$) occur. Voltametric evidence for Zn metal deposition, in conjunction with Schottky barrier heights that are consistent with values expected for a ZnO-Zn junction, suggests that more negative deposition potentials create a Zn-based interface between the substrate and ZnO that leads to rectifying behavior.

4.2 Introduction

ZnO's ability to form rectifying (Schottky) junctions with metals is one characteristic that promotes its use in diodes, varistors, UV detectors, gas sensors, and piezoelectric transducers[15]. There is also a demonstrated need for low-resistance ohmic contacts to ZnO for optical and piezoelectric applications[103]. While many performance improvements have been realized, it remains a challenge to apply predictive power to determine what conditions will yield optimal Schottky or ohmic responses in ZnO/metal heterojunctions[15, 81]. Here, we show that electrochemical deposition methods can be used to selectively form either ohmic or Schottky contacts between polycrystalline ZnO and metals – without compromising the optical response of the ZnO – simply by tuning the applied potential during deposition. We show that this potential-selectivity is intimately related to a Zn-based interfacial layer that forms at more negative deposition potentials. Because the resulting barrier

heights of these one-step, electrochemically synthesized Schottky junctions are competitive with those prepared by more expensive and resource-intensive methods, our method offers promise for greater economy and control over ZnO heterojunctions for device applications.

Recent reviews highlight substantial efforts to improve the quality of Schottky contacts between ZnO, single crystalline or polycrystalline, and high purity precious metals with high work functions (Au, Pd, Pt)[15, 81]. Conversely, lower work function metals and alloys (often based on Al and Ag) have been targeted for ohmic contacts on ZnO[15, 81, 89, 103]. Many approaches for controlled current-voltage response of surface contacts focus on modification of the ZnO/metal interface through acid, plasma, laser, or thermal treatments[19, 20, 81, 85]. The mechanisms behind such improvements are not always investigated, in part because the surface chemistry of ZnO is extremely complex due to the existence of polar and non-polar faces[15].

4.3 Experimental Methods

Electrochemical methods have been widely applied to metal deposition, but their use for preparation of functional oxide materials is still a growing area of research [104, 105, 106]. Our thin films were prepared using a method described in Chapter 2, based on a nitrate-reduction reaction using 0.01 M $Zn(NO_3)_2$ in ultrapure water (pH = 5). Substrates were polycrystalline Pt, Au/Cr/glass, or stainless steel (316 series), and were cleaned in HCl and H_2SO_4 prior to use. Cyclic voltammetry data for

these different substrates in contact with the working electrolyte were collected with a Hokuto Denko HA 501 potentiostat. Constant applied potentials between –0.70 V and –1.50 V (*vs.* Ag/AgCl reference) at 70°C yielded ZnO films with thicknesses ~1 μm, as determined with contact-mode atomic force microscopy (Asylum Research MFP-3D). Structural confirmation was enabled by X-ray diffraction (XRD) data obtained with a Rigaku D/MAX 2200PC (Cu Kα radiation) and analyzed with the LATCON software package[97]. Optical absorption edges were calculated from diffuse reflectance data (Ocean Optics SD2000, 45° incident angle, collinear reflectance collector). Current-voltage (I–V) characteristics of deposited samples were assessed with a Keithley 2400 source meter, employing stainless steel compression contacts (0.06 cm^2).

4.4 Analysis

Electrochemical ZnO deposition produces either ohmic or rectifying contacts, as shown in Figure 4.1. The electrical response of these ZnO heterojunctions are strongly correlated with the potential applied during deposition. For example, ZnO deposits on stainless steel prepared at –0.9 V exhibit ohmic behavior (Figure 4.1a) with through-layer resistances of 1–10 Ω. However, more negative deposition potentials (≤–1.1 V) show much higher perpendicular–to–layer resistances (10^3– 10^6 Ω) even though the ZnO films have similar thicknesses.

In addition, asymmetric rectifying behavior was observed for deposits prepared at these more negative deposition potentials (Figure 4.1b), indicative of a Schottky bar-

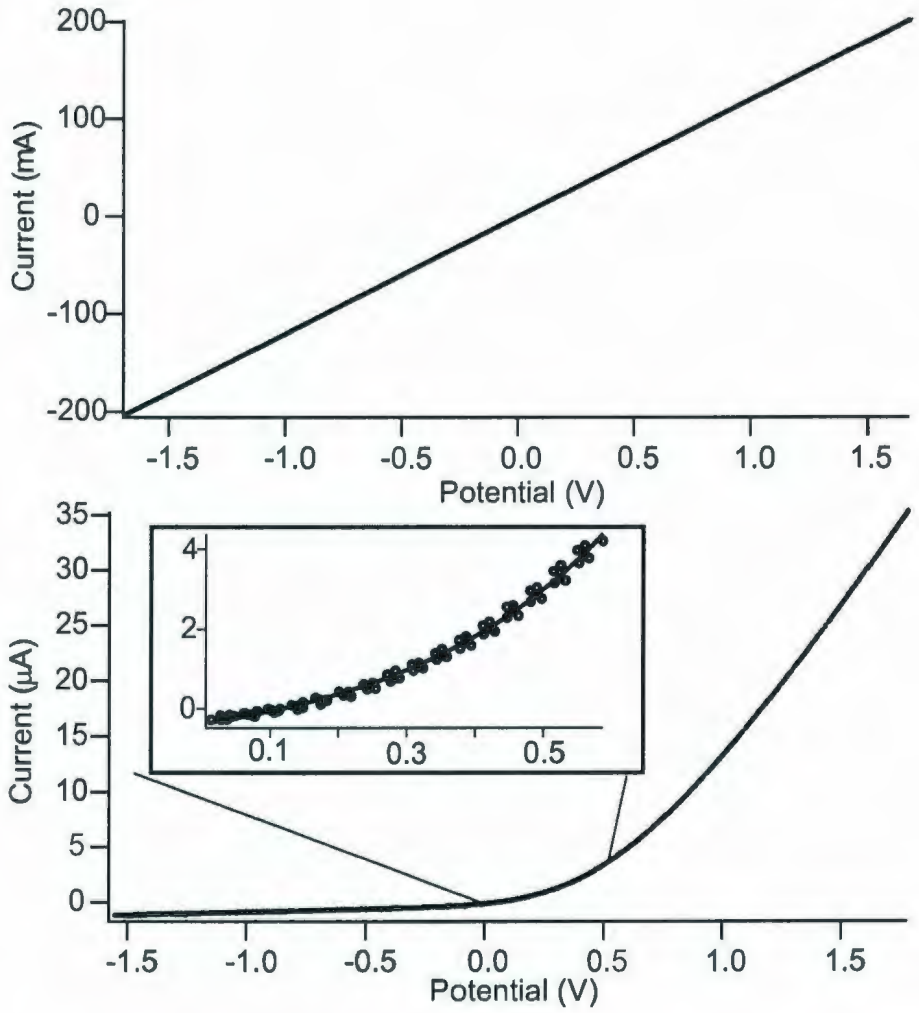

Figure 4.1: Electrodeposited ZnO exhibits an ohmic current-voltage response when prepared at more positive deposition potentials (a), in contrast with asymmetric rectifying behavior for more negative deposition potentials (b). Current values in (b) are scaled relative to reverse-bias leakage currents (~10 nA for Au, Pt and ~100 nA for stainless steel). Positive voltage indicates forward bias.

rier at the ZnO/substrate junction. This ohmic-Schottky deposition potential threshold is also evident on Au (–0.8 V *vs.* $Ag/AgCl_{sat'd}$) and Pt (–1.2 V *vs.* $Ag/AgCl_{sat'd}$). In contrast, semiconducting substrates with band gaps similar to that of ZnO, such as polycrystalline indium tin oxide ($E_g \approx 3.7$ eV), always yielded ohmic contacts with electrodeposited ZnO, regardless of deposition potential. It is not uncommon to see substrate dependent effects on electrochemical reactions due to surface energy, substrate stability, and contact resistance.

A broad range of complementary experiments confirm that our results are consistent with interfacial effects, rather than deposition-potential-related changes in the ZnO film itself. XRD analyses for samples deposited at a potential between –0.9 V to –1.5 V showed diffraction peaks consistent with those hexagonal wurzite ZnO's space group ($P6_3mc$) and lattice constants $a = 3.255\pm0.001$ Å and $c = 5.217\pm0.002$ Å, which are in good agreement with accepted values (3.250 Å and 5.207 Å, JCPDS #36-1451)[11]. Relative peak intensity data show that our films are truly polycrystalline, but with a preference for (002) orientation, as is typical for electrodeposited ZnO[16, 106, 62]. Optical absorption edge values for these same ZnO films, calculated from diffuse reflectance measurements, lie in the accepted range for native ZnO (3.3±0.1 eV) [19, 20].

The rectifying behavior of our electrodeposited junctions compare favorably with ZnO-based Schottky junctions prepared by other methods, with forward-current to leakage-current ratios of ~50:1 and no breakdown at reverse bias voltages up to 2 V.

It is customary to compare the rectifying behavior with an ideal Schottky response as outlined in Equation 4.1:

$$J = A^* T^2 \exp\left(\frac{-q\Phi_B}{kT}\right) \exp\left(\frac{q(V - IR)}{nkT}\right), \tag{4.1}$$

where J is current density, A^* is Richardson's constant ($A^* = 32$ A/cm^{2}K^2), T is temperature, q is the fundamental unit of charge, Φ_B is the Schottky barrier height, k is Boltzmann's constant, V is the applied voltage, I is the resulting current, R is the series resistance, and n is the ideality factor. Schottky barrier heights for our electrodeposited junctions, calculated by fitting I–V data (Figure 4.1b) to Equation 4.1, showed slight variations with substrate: 0.73 ± 0.05 eV for steel, 0.85 ± 0.05 eV for Au, and 0.90 ± 0.05 eV for Pt. All values fall comfortably within the range of ZnO Schottky barrier heights reported by others ($0.6 - 1.0$ eV)[17, 19, 20, 81, 85, 89, 107]. Another measure of the rectifying quality is the ideality factor (n), with a value of 1 corresponding to a perfect exponential transition from leakage current to forward current flow. High values of the ideality factor (> 2) are attributed to the existence of multiple current pathways[81], such as a mixture of spatially distinct rectifying (and ohmic) connections[108]. Our electrodeposited ZnO junctions have high ideality factors (n $\sim$ 10, determined over 0.5 V), commensurate with ZnO Schottky diodes formed using chemical-vapor deposition[82], while more ideal Schottky junctions have been prepared by other methods ($n = 1.0 - 2.0$, determined over ~ 0.1 V)[19, 81, 85, 107]. We chose not to determine n over smaller voltage ranges in order to eliminate artificially small idealities.

To a first approximation, the best Schottky barriers occur when the metal's work function (Φ_m) is very different from the electron affinity (χ_{sc}) of the semiconductor.

$$\Phi_B = \Phi_m - \chi_{sc}. \tag{4.2}$$

For electrodeposited junctions, evidence suggests that a composition-related change in the interfacial electronic states also affects Schottky barrier formation, height, and ideality. Applied deposition potentials more negative than –1.5 V generally favour Zn metal formation over ZnO[62] due to a complicated relationship between Zn metal stability, the local pH increase, and the formation of $Zn(OH)_2$ as can be seen in the simplified Pourbaix diagram in Figure 2.1. At more negative deposition potentials, electrochemical ZnO formation can be preceded by a Zn metal pre-layer, as reported by others[106]. Cyclic voltammograms performed on bare substrates (Figure 4.2) show that reversible deposition and stripping of Zn metal is possible using our electrolyte. Cyclic voltammograms collected from ZnO surfaces do not show stripping peaks do to the complicated nature of the irreversible ZnO formation process. In contrast, ZnO formation is not reversible and has no current associated with it due to the fact that Zn does not change its oxidation state[62]. Substrates such as Pt can support an electrochemically produced Zn surface alloy, although the details of its composition and structure remain elusive[109].

To confirm that the earliest stages of deposition are critical for controlling the ohmic/rectifying responses of our ZnO electrodeposits, we compared constant-potential deposition to a pulsed deposition sequence. Rectifying responses were observed

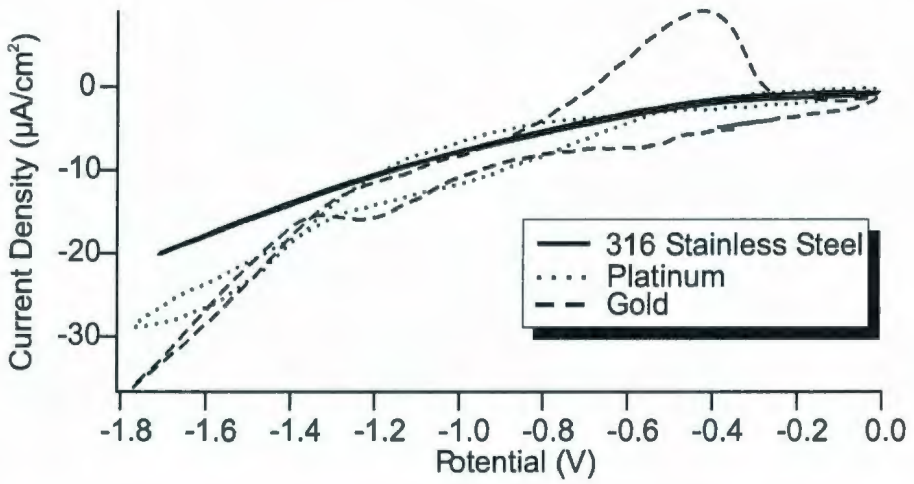

Figure 4.2: Cyclic voltammograms for Au (dashed curve) in 0.1 M $Zn(NO_3)_2$ show an anodic peak near –0.5 V that is characteristic of Zn metal stripping. The suppression of stripping peaks on stainless steel and Pt substrates (solid and dotted curves) during cyclic voltammetry studies in the same electrolyte is consistent with the formation of an electrochemically irreversible Zn alloy, as described in Ref. [109].

for pulse-prepared junctions (–1.5 V for 10 seconds to deposit Zn metal, followed by subsequent deposition at –0.9 V to deposit ZnO), whereas a constant deposition potential of –0.9 V yielded ohmic contacts. We also note that, despite the large difference in work functions of our substrates (Φ_{Au} = 5.1 eV, Φ_{Pt} = 5.7 eV)[65], barrier heights of the electrodeposited junctions on these different substrates show a much smaller spread (0.8±0.1eV). Furthermore, using Equation 4.2 to estimate an effective substrate work function, we find a value of 4.5±0.1 eV which is on par with the work function reported for Zn (4.4 eV)[65]. Thus, the rectifying response in electrodeposited ZnO heterojunctions is consistent with contacts at a Zn metal interface. Carrier concentration measurements on electrodeposits indicate that this is not a simple matter of creating a Zn-rich layer. Failure to create Schottky junctions

on other, higher work function metals without the Zn layer is intimately related to the carrier concentration of the ZnO layers, which will be described in more detail in Chapter 5. Unfortunately, our method for producing ZnO electrodeposits did not work on Zn metal substrates, perhaps due to competing oxidation processes in the electrochemical environment. It is unclear why ZnO could not be deposited on Zn substrates, but the complicated nature of the catalyzed nitrate reduction reaction may play a part in the failure to grow ZnO.

We established a more definite link between Schottky behavior and the presence of a Zn-based pre-layer at the buried interface using scanning electron microscopy (SEM, FEI Quanta 400) with energy dispersive X-ray (EDX) analysis. ZnO/substrate interfaces were exposed by mechanically detaching film from their substrates by cooling epoxy-coated films in liquid nitrogen. EDX data show higher Zn content at the ZnO/substrate interface relative to the ZnO film's air interface. Using the Zn/O peak height ratio collected from the top of ZnO samples deposited at all conditions, and comparing this with the Zn/O peak height ratio collected from the ZnO/substrate interface, we saw an increase in the relative height of the Zn peak only on samples that also exhibited rectifying behaviour. EDX investigations on the stainless steel substrates after ZnO film removal show no evidence of Zn content, suggesting that the Zn-based pre-layer contributing to the Schottky response is strongly adhered to the ZnO film. Contrast variations in the backscattered electron images from the ZnO/substrate interface suggest that the Zn-based pre-layer may have thickness

inhomogeneities, which would be consistent with multiple conduction pathways[81] implied by our films' high ideality factors.

4.5 Conclusion

In summary, potentiostatic electrochemical deposition of ZnO on metal substrates provides selectivity between ohmic contacts and Schottky junctions, with no need for annealing. This selectivity can be attributed to potential-dependent formation of a Zn-based interface between the substrate and ZnO electrodeposit, thereby yielding barrier heights consistent with ZnO-Zn contacts. The electrodeposited junctions compare well with ZnO Schottky diodes synthesized using more resource-intensive synthesis methods, offering an opportunity for greater economy and control over ZnO heterojunctions for device applications.

Chapter 5

Significant Carrier Concentration Changes in Native Electrodeposited ZnO

5.1 Abstract

We show that unintentional hydrogen doping of ZnO during the electrodeposition process can impact the material's carrier concentration as significantly as others have reported for intentional extrinsic doping. Mott-Schottky analyses on the natively n-type electrodeposits show a decrease in carrier concentrations from 10^{21} to 10^{18} cm^{-3} with increasing overpotential. A strong link exists between larger optical band gaps (determined from diffuse reflectance spectroscopy) and higher carrier concentrations,

which suggests that hydrogen-based doping underlies the n-type conductivity (Moss-Burstein effect). We propose that kinetic defects introduced during growth at larger overpotentials compete with hydrogen doping, thereby leading to lower net carrier concentrations. This has important implications for using deposition potential to tune other electrodeposit properties such as growth rate and morphology.

5.2 Introduction

Transparent semiconducting materials are the cornerstone of many optoelectronic devices, including those used in the photovoltaic industry[15, 44]. In these applications, reliable control of carrier concentration is essential to optimize both optical transparency and electrical conductivity. Electrochemical deposition of transparent semiconductors is gaining acceptance as a viable means of producing films of transparent semiconducting metal oxides such as ZnO and TiO_2[95]. However, there is still much to be understood about how to control carrier concentrations in these electrodeposited materials. Here, we show that the carrier concentration of native electrodeposited ZnO can be modified over several orders of magnitude simply by changing the potential applied during deposition. Our results show an approach to n-doping that yields a similar range of carrier concentrations without introducing intentional dopants. The implications are that using potential to control other features of the electrodeposit, such as growth rate or morphology, may simultaneously affect the deposit's electronic properties.

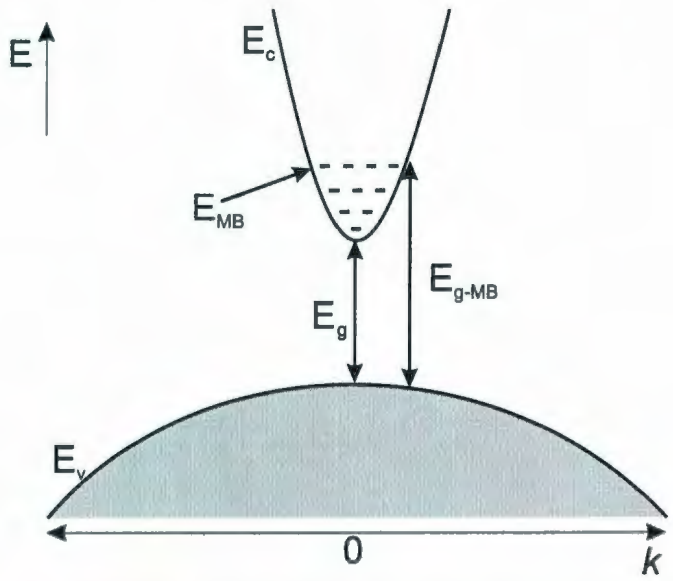

Figure 5.1: Schematic diagram of the band structure of a semiconductor doped with a Moss-Burstein dopant. The energy level of a Moss-Burstein dopant E_{MB} can reside in the conduction band for high doping levels, increasing the band gap from E_g to E_{g-MB}.

ZnO is a well-studied wide band gap material that is n-type in its native form[15, 19, 20, 80, 110]. Considerable scientific effort has been devoted to understanding how and why hydrogen is the cause of this n-type doping[12, 14, 111]. Hydrogen is expected to be an amphoteric dopant in most materials by compensating existing defects. In ZnO, however, electronically active interstitial H^+ serves as a donor[12, 73, 75] and increases the band gap energy when doping levels are high enough to lead to degenerate semiconducting behavior (Figure 5.1). This Moss-Burstein effect of larger band gaps with higher doping levels is a trend that opposes the usual response of decreasing band gap with an increase in extrinsic dopants (as has been observed in boron-doped ZnO[10, 112]).

This work, based on Mott-Schottky analyses, shows that significant changes in carrier concentration can be induced in native ZnO electrodeposits without introducing intentional dopants. Since the hydrogen evolution reaction (HER) proceeds concurrently with ZnO electrosynthesis, there is an obvious presence of hydrogen. However, there are no existing studies that address its effect on carrier concentration in electrodeposits.

5.3 Experimental Methods

5.3.1 ZnO Electrosynthesis

ZnO thin films were deposited using the method described in Chapter 2. ZnO samples were synthesized from 0.01 M $Zn(NO_3)_2$ (ACS reagent grade, SCP Science in 18.2 MΩ·cm water, Barnstead Nanopure). Electrolyte *p*H was controlled by the addition of HCl (*p*H = 4.0-5.5) or NaOH (*p*H = 6.0-7.5). Deposition potentials, ranging from –1.3 V to –0.85 V, are all reported relative to a Ag/AgCl reference. Substrates consisted of mechanically polished stainless steel (316 stainless steel or A286 steel alloy) that were ultrasonically cleaned prior to use.

5.3.2 Carrier Concentration Measurements

Mott-Schottky (MS) analysis, based on the concept of impedance spectroscopy, utilizes the relationship between capacitance and applied potential to extract infor-

mation about a material's carrier concentration. This technique has been applied to nano-structured[91, 113] as well as Cl-doped[10] ZnO.

MS analysis assesses carrier concentrations near a rectifying (non-ohmic, Schottky) junction at the surface of the semiconductor; in our experiments, this was achieved at the semiconductor/electrolyte interface. For Schottky junctions, theory dictates that the junction capacitance squared will vary linearly with the inverse of the applied reverse bias, as shown here:

$$\left(\frac{1}{C}\right)^2 = \left(\frac{2(V_{bi}) + V_R}{e\epsilon_s a^2 N_d}\right). \tag{5.1}$$

Here, C is the junction capacitance, V_R is the applied reverse bias voltage, V_{bi} is the built-in potential, a is the surface area of the junction, e is the elemental charge, N_d is the carrier concentration, and ϵ_s is the semiconductor's dielectric constant, which we take to be 8.0 for bulk ZnO[91]. In reality, extra terms must be added to account for additional capacitive effects due to classic dielectric capacitance, C_d, as well as the "double-layer" capacitance, C_{dl} (due to an accumulation of ions at the surface of the working electrode), and capacitance due to fractional coverage or a conducting substrate (f) and increased surface area fraction due to roughness (g, where $g = 1.5$ would indicate a 50% increase in surface area due to roughness)[92]:

$$\left(\frac{1}{C}\right)^2 = \left(\frac{2(V_{bi}) + V_R}{e\epsilon_s a^2 N_d}\right) + (1-f)\frac{1}{C_{dl}^2} + f\left(\frac{1}{C_d} + \frac{1}{gC_{dl}}\right)^2 \tag{5.2}$$

Since these additional capacitance terms change the intercept – but not the slope –

of Equation 5.1, it is not necessary to quantify all auxiliary capacitances in order to determine the carrier concentration.

Accounting for the true surface area, a, of the ZnO in contact with the electrolyte requires prudent approximations. Since one of the classical methods for analytical electrochemical surface measurements (hydrogen adsorption)[114, 115, 116] does not work well for oxide surfaces, we used RMS roughness analyses of atomic force microscopy (AFM) images. This procedure determines the surfaces area of a sample from an AFM micrograph and computes roughness by determining the increase in surface area over the planar area of the scan. Our data show a surface area increase of 50±25% over the planar area. We expect that this is an underestimation of the true surface area, suggesting the carrier concentrations determined from our MS data are upper limits, with uncertainties on the order of a factor of two. Therefore, we focus on trends and order of magnitude variations in carrier concentrations, rather than on specific values.

MS analyses were performed in electrolyte by superimposing an alternating current at 10-15 kHz with a peak-to-peak voltage of 20 mV over a stepped potential ranging from -1 V to 1.3 V *vs.* Ag/AgCl and measuring the resulting impedance. Capacitance values were extracted from impedance data using the relation:

$$C = \frac{1}{j\omega Z}. \tag{5.3}$$

MS experiments were controlled by, and data were collected with, the PowerSUITE

(EG&G Princeton Applied Research (PAR)) impedance spectroscopy software package interfaced with a PAR 273A potentiostat and Signal Recovery 5210 lock-in amplifier. Several supporting electrolytes were tested for their suitability for these MS experiments. The native electrolyte (pH adjusted 0.01 M $Zn(NO_3)_2$), as used by Windisch *et al.*[91], contributes capacitance fluctuations due to both the nitrate reduction reaction and Zn^{2+} adsorbtion, as discussed by Pajkossy[117]. A better alternative was a modified phosphate buffer, similar to one reported recently[10], consisting of 0.063 M K_2PO_4 + .036 M NaOH, which has a pH of 7. All MS data shown here were collected using this buffered phosphate electrolyte.

5.4 Results

The electrodeposition process yields ZnO thin films whose lattice constants were refined to 3.246±0.001 Å and c = 5.205±0.002 Å, which is in excellent agreement with JCPDS #36-1451 for ZnO (3.250 Å and 5.207 Å)[11]. The refined lattice constants showed no pH dependence for samples deposited over a range of pH values (5.5-7.5) and deposition potentials (–1.3 V to –0.85 V), as was seen with previous results from our group over a more acidic pH range (4-5.5)[41]. Qualitative comparisons of relative peak heights also confirmed that, while our samples are polycrystalline, there is a preferred (002) orientation in the deposit, which is typical for electrodeposited ZnO[16, 106, 62]. This (002) texture is moderately accentuated for samples deposited at -1.1 V (pH 6.5), coinciding with a morphological change from hexagonal

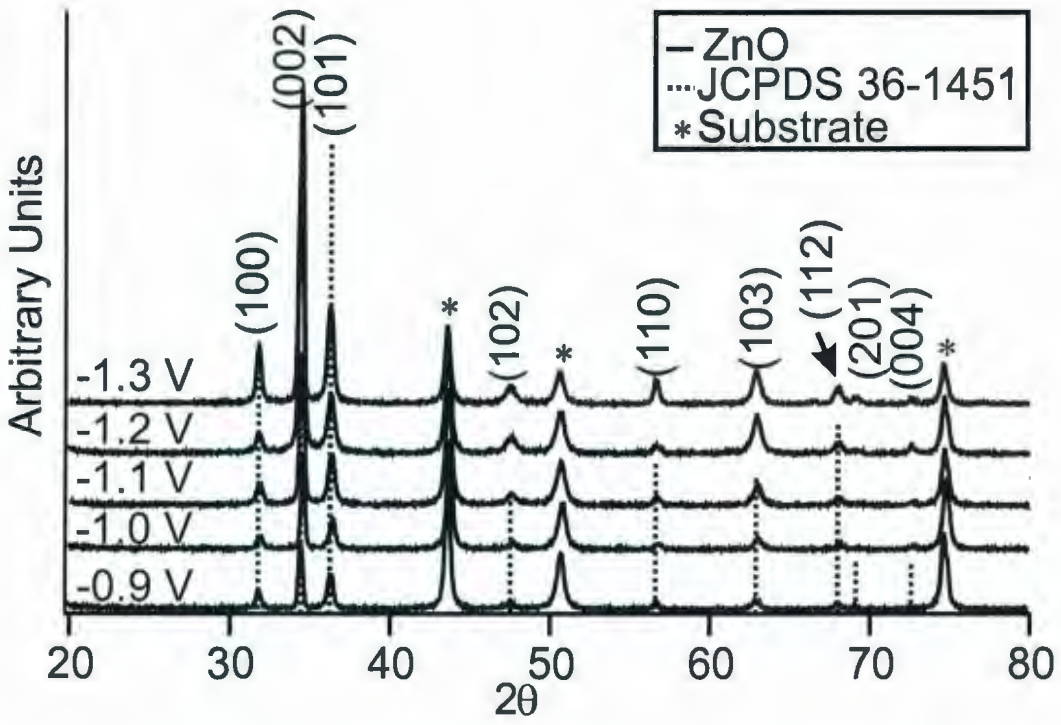

Figure 5.2: Representative indexed XRD patterns from electrodeposited ZnO prepared at *p*H 6.5 with deposition potentials ranging from -1.3 V to -0.9 V *vs.* Ag/AgCl. Refined lattice constants for electrodeposits deposited over the complete range of deposition conditions compared well with the accepted values (a=3.250 Å and c=5.207 Å, JCPDS #36-1451). Plots are offset along the intensity axis for clarity.

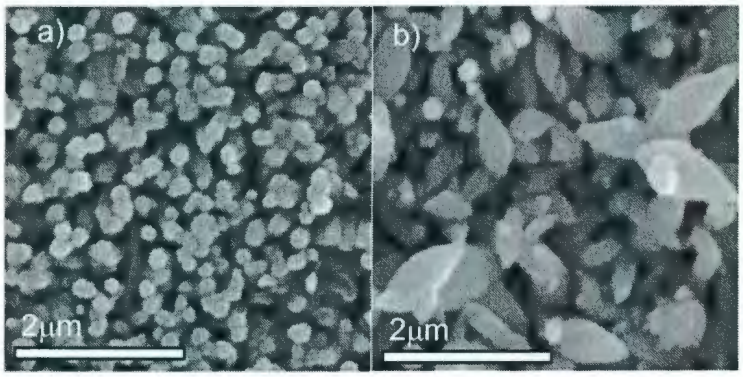

Figure 5.3: Representative SEM micrographs of ZnO samples deposited at -0.9 V in *p*H 6.5 electrolyte (a) and -1.3 V in *p*H 5 electrolyte (b). The hexagonal columns in (a) are typical of deposits from neutral *p*H electrolytes and more positive deposition potentials, while the rice-like morphologies are observed at more negative potentials and more acidic *p*H values. Despite these morphological differences, AFM roughness analyses indicate that both morphologies have similar roughness ratios (1.50 ± 0.25).

crystallites to rice-like structures, as shown in Figure 5.3, and reported previously for electrodeposited zinc oxide[16, 118].

Solution based Mott-Schottky analyses were performed on electrodeposited ZnO/-metal junctions, both ohmic and rectifying. While this technique is well known for nominally ohmic ZnO/substrate junctions[10, 91, 113], it has not previously been performed on samples that already contain a Schottky barrier. A review of the applied bias directions and energy band diagrams, as shown in Figure 5.4, shows that a Schottky barrier at the ZnO/substrate does not adversely impact these capacitance measurements. When a positive potential is applied to the substrate, the ZnO/solution junction is reverse biased, as required for the Mott-Schottky analysis, while ZnO/substrate Schottky junction is forward biased (allowing current flow).

Mott-Schottky plots of ZnO performed in the phosphate buffer typically exhibited

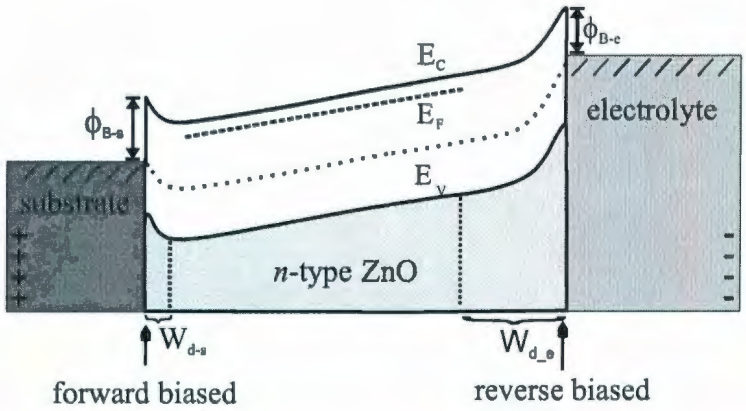

Figure 5.4: Energy band diagram of the substrate/ZnO/electrolyte system during Mott-Schottky analysis for a sample with a pre-existing ZnO/substrate Schottky junction. (A positive potential is applied to the substrate.) Note the large ZnO/electrolyte depletion width (W_{d-e}), compared to the ZnO/substrate depletion width (W_{d-s}), indicating that the ZnO/electrolyte junction is reverse biased while the ZnO/substrate junction is forward biased.

linear responses at potentials between -0.4 V and 0.4 V *vs.* Ag/AgCl (as seen in Figure 5.5), confirming that the effect of the ZnO/substrate Schottky junction is negligible with respect to Mott-Schottky behaviour. For purely ohmic ZnO samples, conduction across the ZnO/substrate is equivalent to a standard contact resistance, and thus does not need special consideration.

Despite the fact that XRD shows no obvious structural differences among samples prepared over this potential and *p*H range, we find drastically different carrier concentrations based on MS analyses. Representative MS plots for samples deposited at low (-1.1 V) and high (-0.9 V) applied potentials (from *p*H 6.5 electrolyte) are shown in Figure 5.5. Linear regression of the slope of these curves corresponds to carrier concentrations of $9 \pm 2 \times 10^{20}$ cm^{-3} and $2 \pm 1 \times 10^{19}$ cm^{-3}, respectively. Over a range

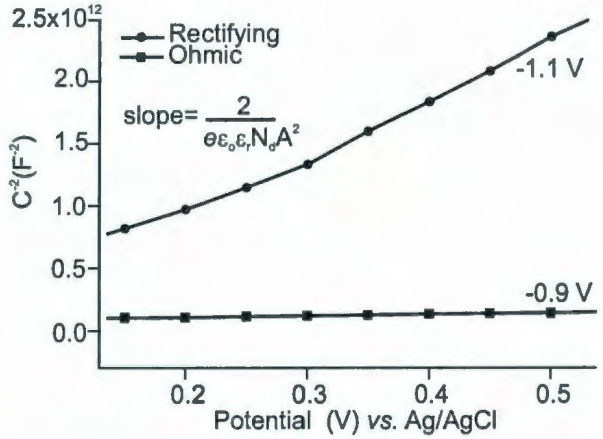

Figure 5.5: Representative C^{-2} *vs.* potential plots obtained from solution Mott-Schottky analyses performed on electrodeposited ZnO samples in *p*H 7 phosphate buffer exhibited linear behaviour over potentials ranging from -0.4 V to 0.4 V *vs.* Ag/AgCl. The upper curve was collected from a samples deposited at -0.9 V, while the lower curve was collected from a sample deposited at -1.1 V. Uncertainty values are determined by the linear regression analysis of the data.

of applied deposition potentials (all in *p*H 6.5 electrolyte), there is a clear trend of decreasing carrier concentration with more negative deposition potentials, as shown in Figure 5.6a. Comparing data from electrodeposits prepared at different *p*H values, Figure 5.6b shows carrier concentration *versus* the standard potential of the hydrogen evolution reaction (HER). Since the potential at which hydrogen evolves in solution is dependent upon *p*H, this effectively couples potential and *p*H, allowing a more direct comparison of carrier concentration change with deposition conditions. Both Figures 5.6a and 5.6b show that carrier concentration decreases with increasing overpotential (with respect to HER). This relationship was established based on measurements of dozens of different samples. Error bars in Figures 5.6a and 5.6b were determined from the standard deviation of multiple measurements, and the uncertainty in Mott-

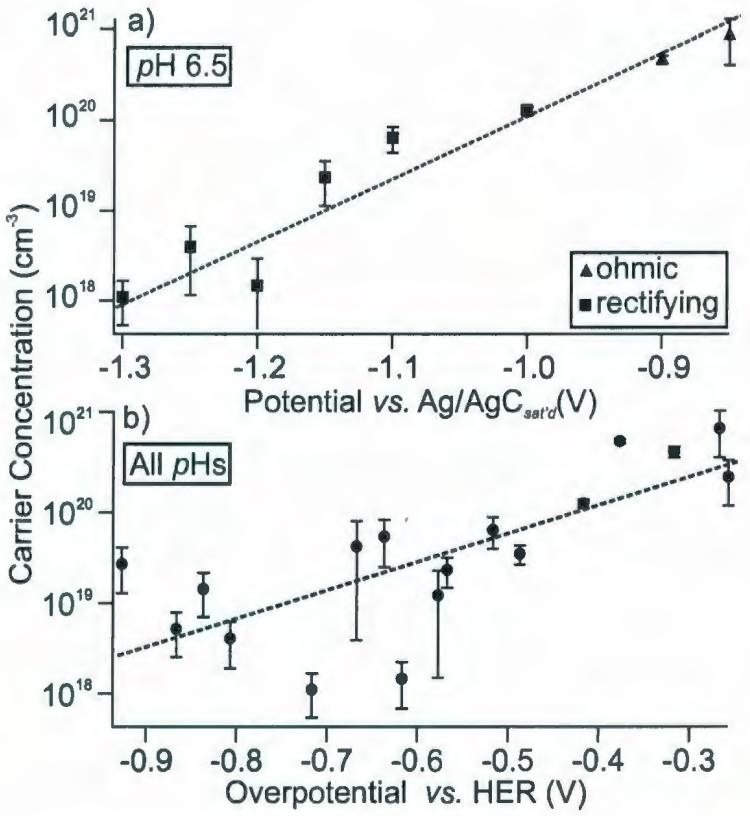

Figure 5.6: Carrier concentrations determined by solution Mott-Schottky analyses indicate a linear relationship between deposition potential and the log of carrier concentration. Graph (a) is plotted for samples deposited at *p*H 6.5 and shows the trend very clearly, while graph (b) is plotted against overpotential (*vs.* the water electrolysis standard potential) and indicates that the trend is present in samples deposited over the whole range of deposition potentials.

Schottky plot slopes.

Since carrier concentration changes can influence optical as well as electronic properties, we also compared trends in optical absorption edges, obtained from diffuse reflectance spectra, with electrodeposition conditions. Samples deposited at more positive potentials exhibited larger band gaps than samples deposited at more negative deposition potentials, as can be seen in Figure 5.7a (samples synthesized at

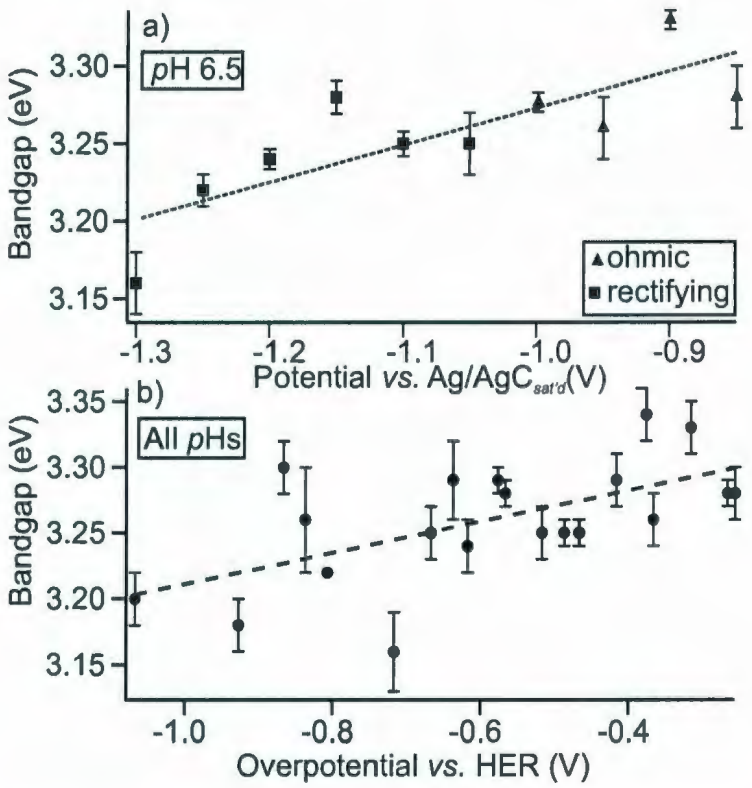

Figure 5.7: UV/Visible diffuse reflectance analysis was used to collect sample band gap values. Our data indicates a linear relationship between band gap and deposition potential. Graph (a) exhibits this linear trend for samples deposited at *p*H 6.5 and is plotted against a Ag/AgCl reference electrode. Graph (b) indicates that this linear trend occurs in samples deposited over all deposition conditions, here it is plotted against the water electrolysis standard potential.

*p*H 6.5) and Figure 5.7b (all samples). Optical band gaps ranged between 3.1 eV and 3.4 eV, which is in agreement with the accepted value for the band gap of ZnO[15, 19, 20, 80, 110].

We note that built-in potentials could not be extracted from our MS data due to an additional sample-dependent capacitance. This may be due to variations in the electrodeposit coverage (parameter f in Equation 5.2), since earlier studies[41]

have shown that small pinholes can occur in our electrodeposits. Fabregat-Santiago *et al.* have also shown that sample-dependent capacitances can occur when there are sample/electrolyte interactions[92].

5.5 Discussion

Over the entire range of deposition potentials (-1.3 to -0.85 V) and *p*H values (4.0 to 7.5) studied, ZnO carrier concentrations ranged between 10^{17} cm^{-3} and 10^{20} cm^{-3}. This range is in agreement with reported carrier concentrations for ZnO[91, 113], including ZnO electrodeposited from nitrate-based electrolytes[10, 112].

Our results indicate a higher *n*-type carrier concentration in ZnO that is electrodeposited at more positive deposition potentials. While some electrolytes, such as those containing Cl^-[10] or borane[112], offer a clear opportunity for extrinsic doping, the same cannot be said for our nitrate-based electrolyte. Instead, it is much more likely that hydrogen is incorporated as an *n*-type dopant. We support this claim by correlating the trends in carrier concentration and optical band gap with respect to deposition potential.

Figure 5.8 shows that the band gap of our ZnO electrodeposits increase with carrier concentration. In the context of traditional donor/acceptor band theory, a decreased band gap would indicate an increased carrier concentration. However, hydrogen doping in ZnO has been observed to go against this trend[12, 68, 71]. Hydrogen-donated electrons can fill empty states in the conduction band of ZnO when doping levels

are high enough to create a degenerate semiconductor, thereby leading to increased band gaps with higher doping levels (Moss-Burstein effect)[16, 119]. Our data are consistent with this Moss-Burstein doping, whether for a single *p*H (Figure 5.8a for samples deposited at *p*H 6.5 from a Cl^-–free electrolyte) or over our whole range of deposition conditions (Figure 5.8b).

If we use the band gap *vs.* potential trend to attribute the increasing carrier concentration to higher H^+ doping levels, we arrive at an interesting – and rather counterintuitive – finding. Intuitively, one could reasonably expect that an increase in hydrogen generation would translate into more incorporated hydrogen and consequently a higher carrier concentration[16]. However, we observe higher carrier concentrations at more positive deposition potentials, where there should be a lower rate of hydrogen generation[50]. Thus, our findings suggest that the relationship between carrier concentration and the presence of hydrogen during the electrosynthesis process is more complicated.

One likely complicating factor is the presence of multiple types of defects. While recent studies indicate that hydrogen donors are an energetically favourable dopant, and thus the most dominant factor in the *n*-type doping in ZnO, there is experimental evidence that supports the prevalence of oxygen and zinc vacancy, interstitial, and anti-site defect contributions[86, 115, 120, 121]. Of these intrinsic point defects, it is known that zinc vacancies, oxygen interstitials, and oxygen anti-sites act as deep acceptors within ZnO while oxygen vacancies, zinc interstitials, and zinc anti-sites act

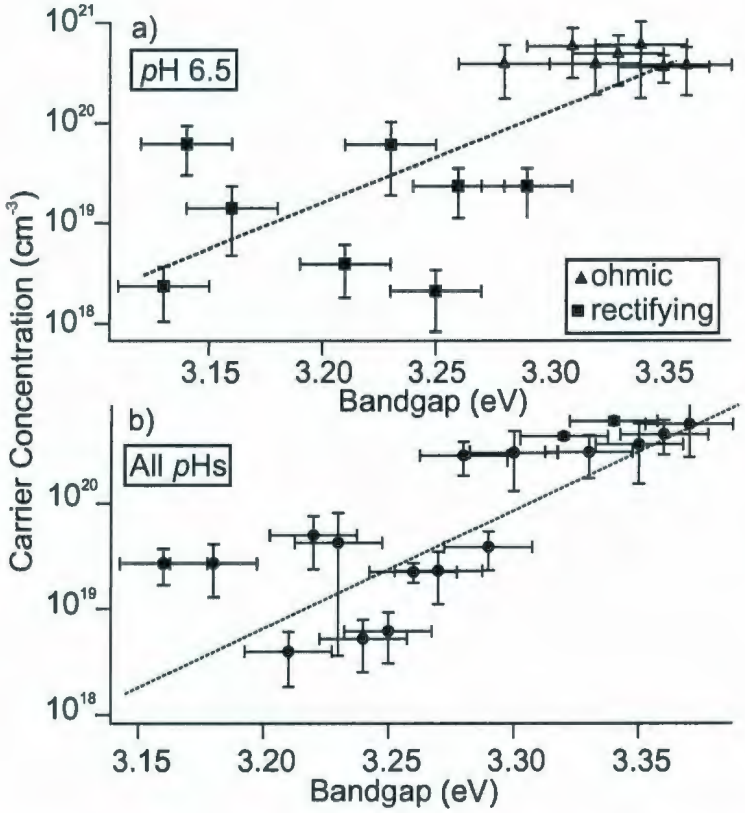

Figure 5.8: We also compared carrier concentration to band gap from samples specifically deposited in pH 6.5 (a) and for samples deposited over the whole range of deposition conditions. Our data indicate that there is a reduction in carrier concentration with band gap, as expected from a Moss-Burstein dopant such as hydrogen acts in ZnO. Plots (a) and (b) also exhibit a limiting of the carrier concentration for wider band gaps, perhaps indicating the maximum amount of hydrogen that can be electrically active within the ZnO crystal lattice.

as donors. In fact, it has been found that in ZnO the formation of acceptor defects is energetically preferable to the formation of native donor defects[14, 122, 123]. In particular, zinc vacancy acceptors require the lowest formation energies of the three acceptor defects[14], and they are also stable to temperatures of 300°C, which is far above our electrodeposition temperatures. Consequently, zinc vacancies would be the most likely kind of acceptor defect, according to thermodynamic arguments, and these acceptors could compensate for, and thus diminish the overall effect of, increased hydrogen incorporation. Previous studies have confirmed that the presence of deep acceptors in ZnO crystals will be active toward hydrogen passivation in ZnO[12, 124].

If we adopt the working hypothesis that compensating defects could reduce the net n-type carrier concentration, it is reasonable to expect that these defects would be more prevalent at more negative deposition potentials. Reaction kinetics will be faster at greater overpotentials, and this increase in synthesis rate would likely contribute to an increase in defect densities. This is indeed consistent with the results shown in Figure 5.8. The only other possible contributor is the unintentional doping with a similar Moss-Burstein doping. Fortunately, careful attention to the purity and choice of our *in situ* chemical species excludes unintentional doping.

We have considered techniques such as Rutherford backscattering and neutron reflectometry to directly measure the amount of hydrogen within our samples as well. Unfortunately, our preliminary experiments with Rutherford backscattering has indicated that the samples are too rough to obtain meaningful hydrogen con-

tent data. Similarly, neutron reflectometry would not have been able to quantitatively assess hydrogen content, even at very high hydrogen concentrations ($\sim 10^{21}$ cm^{-3}). Other studies have combined annealing and conductivity measurements with mass spectrometry[125, 126] or IR/Raman spectroscopy[71, 70, 124] to experimentally prove the existence of electronically active hydrogen within ZnO.

5.6 Conclusions

The large change in carrier concentrations of native (unintentionally doped) electrodeposited ZnO is comparable in magnitude to the effect of intentional extrinsic dopants like Cl^- or borates. We observe that higher n-type carrier concentrations coincide with larger optical band gaps, which is consistent with the Moss-Burstein dopant hydrogen. Our data also indicate that both net carrier concentration and band gap are lower in samples deposited at more negative deposition potentials, contrary to the increase in hydrogen generation at more negative deposition potentials. We attribute this trend to acceptor defects that are more prevalent in deposits with faster growth rates.

There are inherent difficulties in quantitative assessments of hydrogen incorporation in semiconductors, particularly in assessing the hydrogen coordination environment, mobility, and complexation. For this reason, the study of donor and acceptor defects is receiving considerable attention from the scientific community[21], both theoretically and experimentally. The results of the present study show that while

hydrogen doping is most likely the dominant source of net carrier concentration in n-type ZnO, the concentration of compensating defects (deep acceptors in ZnO) likely play a large role in the overall carrier concentration.

Chapter 6

The Effect of Synthesis Conditions and Humidity on Current-Voltage Relations in Electrodeposited ZnO-based Schottky Junctions

6.1 Abstract

Electrochemically produced ZnO/metal rectifying (Schottky) junctions can exhibit consistent barrier heights and high rectifying ratios when prepared using optimized electrolyte *p*H (6.5) and applied voltage ($\leq$-1.1 V *vs.* Ag/AgCl) conditions. An increase in soft breakdown for more acidic deposition electrolytes (*p*H 4) correlates with a diminished preferred orientation in the resulting ZnO electrodeposit. Forward-biased junctions exposed to increased relative humidities show increased current as a result of protonic conduction from water hydrolysis at the ZnO/air interface. At moderate to high relative humidities (50 – 85% RH), hydrophobic coatings improve the quality of the rectifying response by changing the wetting properties of the ZnO surface. Our findings suggest that electrodeposition, in conjunction with post-deposition surface coatings, can offer improved functionality for electron transport materials in wet or humid environments.

6.2 Introduction

ZnO can manifest humidity-related changes in its electronic properties such as resistivity, rectification, and capacitance[127, 128, 129]. Different mechanisms to explain the origin of humidity effects for metal oxide materials have been proposed, including temperature-dependent or voltage-dependent chemisorption[129, 130, 131, 132]. Here we show that electrochemically prepared ZnO rectifying (Schottky) junc-

tions have current-voltage relationships that are influenced by relative humidity changes at ambient temperatures due to a water electrolysis mechanism[133, 134], and that their responses can be qualitatively changed by varying electrolyte *p*H during electrodeposition or by adding post-deposition coatings. These findings highlight the effect that wet or humid environments can have on electron transport materials.

The relationship between humidity and electron transport in ZnO has been investigated in diverse contexts. For example, ZnO has been widely studied as a ceramic material for humidity sensing applications[127, 128, 129, 131]. When used in rectifying *pn* heterojunction humidity sensors, it has been proposed that the electrolytic decomposition of water at the junction continually refreshes the surface to prolong device operation[134]. In contrast, other studies have shown that electrolysis of condensed water can contribute to undesirable degradation in ZnO-based varistors[135] that are exposed to water vapor during the course of their normal operation.

ZnO-based Schottky junctions are typically fabricated using high temperature, high vacuum, or sol-gel processes[128, 129, 130]. Our alternative approach is to use electrochemical deposition to form the rectifying junction. Electrodeposition is a technique that has been used to make ZnO thin films[16, 39, 59, 60, 95], but reports of its electrical resistivity have more often been associated with its function in multilayer systems[94, 136, 137, 138] rather than ZnO alone[40]. Furthermore, none have investigated the impact of humidity changes on electrical responses in electrodeposited ZnO, despite the fact that this synthesis method offers options for controlled deposit

epitaxy and porosity[16, 39, 95].

6.3 Experimental Methods

6.3.1 ZnO Electrosynthesis

Previous work from our group addressed the synthesis conditions required for ZnO electrodeposits displaying either ohmic or rectifying contacts with the underlying conducting metal substrates (Chapter 4)[40]. In the present work, we identify an expanded range of deposition conditions that can be used to synthesize rectifying ZnO contacts – with dramatically improved performance – by adjusting electrolyte *p*H. Samples were deposited at potentials ranging from –2.0 V to –0.7 V *vs.* an Ag/AgCl reference, from an electrolyte of 0.01 M $Zn(NO_3)_2$ (ACS reagent grade, SCP Science) in ultrapure water (18.2 MΩ·cm, Barnstead Nanopure), using HCl or NaOH to adjust the *p*H between 4.0 and 7.0, respectively. Mechanically polished stainless steel (316 series) substrates were cleaned by ultrasonication prior to use. Further details on the reaction mechanism are given in Chapter 2.

6.3.2 Electrical Properties

The current-voltage (I–V) characteristics of electrodeposits were collected with either a Hokuto Denko HA 501 potentiostat or a Keithley 2400 Sourcemeter under varying humidity conditions. Relative humidity was controlled using a sealable plastic

cell with adjustable vents. Dessicant and water vapor were used to adjust the relative humidity of the cell between 15 and 85% (±7%). All DC data were collected and analyzed with LabVIEW (National Instruments, customized in-house). Electrical connections to the samples involved low-resistance (< 1 Ω) ohmic stainless steel or aluminum compression contacts. Contact areas (∼ 0.18 cm^2) were large compared to individual crystallite sizes (typically 100–1000 nm in diameter), so we assume that all electrical measurements involved conduction through and/or across many ZnO grains.

6.4 Results and Discussion

6.4.1 Electrodeposit Characterization

XRD data from electrodeposits (Figure 6.1) were compared with standard diffraction data for hexagonal ZnO (JCPDS 36-1451) and zinc metal (JCPDS 04-0831)[11]. All observed peaks can be indexed to either ZnO or the substrate. However, the presence or absence of Zn metal is difficult to confirm definitively from XRD data because two of the strongest Zn Bragg reflections would appear near (and overlap with) the ZnO (101) and substrate peaks.

Although the electrodeposits appear to be phase-pure based on XRD data, investigations of the ZnO/substrate interface suggest that compositional differences do exist. To facilitate SEM and EDX investigations, the substrate-supported electrode-

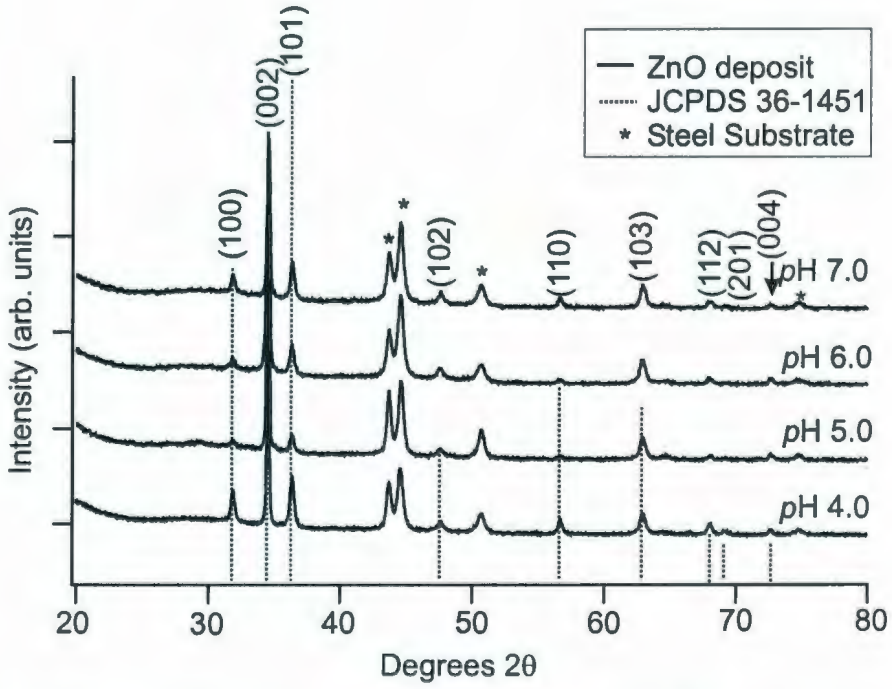

Figure 6.1: Representative indexed XRD patterns from thin films (1.0 ± 0.2 μm thickness) of ZnO prepared by deposition from electrolytes with different bulk pH values. Lattice constant refinements of the indexed peaks yield excellent agreement with ZnO (JCPDS #36-1451)[11]. Bragg peaks due to the stainless steel substrates are marked with an asterisk (*).

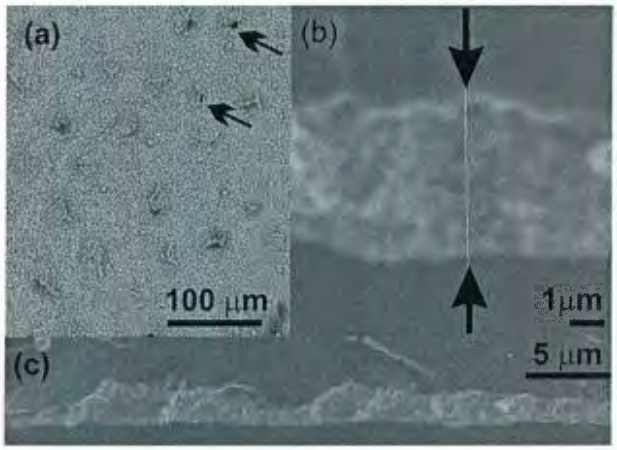

Figure 6.2: Representative SEM images showing (a) the top (air interface) of a ZnO electrodeposit, and (b,c) cross-sectional views. This deposit was prepared from an electrolyte with bulk *p*H 5.5 at -1.1 V. The arrows in the top view in (a) show that occasional pinholes can exist in the film exist. The cross-sectional view in (b) highlights the polycrystalline grains in the electrodeposit, while (c) shows typical thickness changes across the deposit.

posits were coated with epoxy and then immersed in liquid nitrogen to separate the ZnO from the steel substrate, allowing for comparative analysis at both the ZnO/air and the ZnO/substrate interfaces. Differences in the contrast of backscattered electron images from the two ZnO interfaces, in conjunction with elemental composition information from complementary EDX measurements, suggest that there is a higher Zn content at the ZnO/substrate interface. We note that high Zn content at this interface coincides with rectifying current-voltage responses, described in more detail elsewhere[40].

Cross-sectional SEM images (Figure 6.2b,c) emphasize that electrodeposits are polycrystalline films whose thicknesses vary across the sample (typically 1-3 μm). These films are generally continuous, but occasional holes are visible, such as those

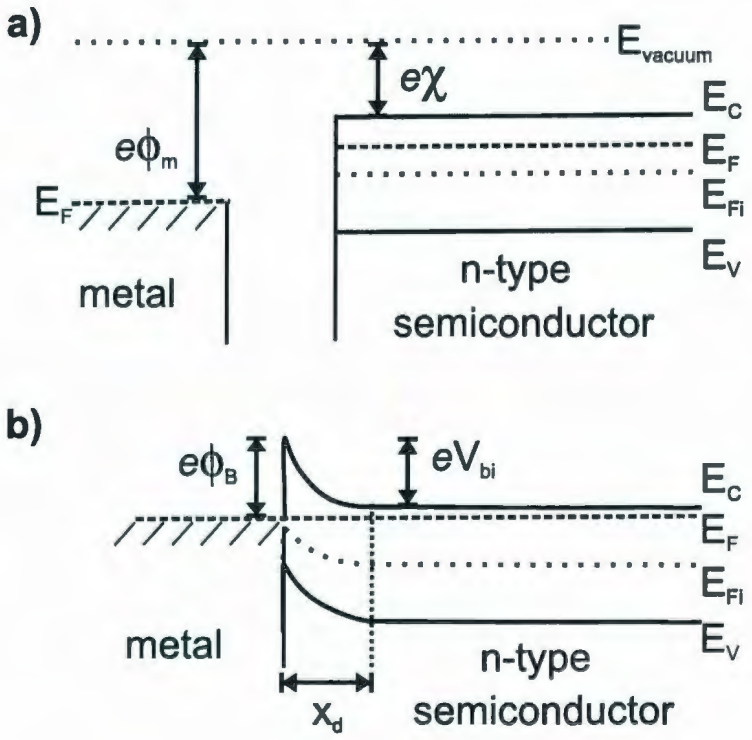

Figure 6.3: A schematic energy band diagram for (a) isolated metal and n-type semiconductor, and (b) a Schottky junction. The work function of the metal (ϕ_m) and the electron affinity of the semiconductor (χ) are given relative to vacuum level (E_{vacuum}). In the n-type semiconductor, the Fermi energy (E_F) is closer to the conduction band energy (E_C) than the valence band energy (E_V). The intrinsic Fermi energy (E_{Fi}) is located mid-way between E_C and E_V. (b) Once the metal and semiconductor come into contact, a Schottky barrier (ϕ_B) forms at the interface and the semiconductor bands bend by an amount V_{bi} over the distance x_D.

denoted with arrows in Figure 6.2a.

6.4.2 Effects of Synthesis Conditions on Rectifying Behavior

The rectifying function of an ideal Schottky junction is based on the relative Fermi energy levels between a n-type semiconductor and metal[139], as shown schematically in Figure 6.3. Theoretically if, when isolated, the Fermi energy of the semiconductor

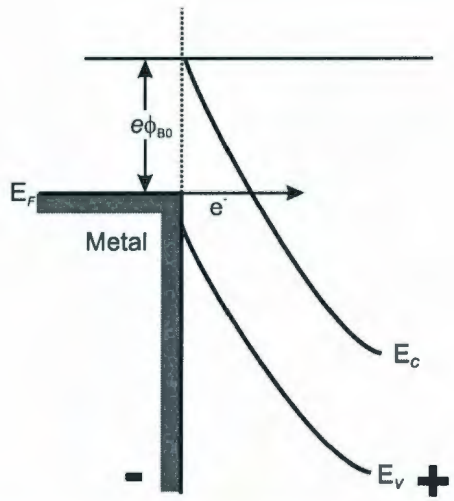

Figure 6.4: At high reverse bias potentials, electrons in a junction can traverse the Schottky barrier without going over the barrier. When occurring only at spatially distinct small regions in a junction, this mechanism is called soft breakdown.

is higher than that of the metal (semiconductor electron affinity is lower than the work function of the metal), then electrons in the semiconductor will move to the lower energy states in the metal to equilibrate the Fermi energies, once contact is established. As a consequence, electrons in the semiconductor encounter a potential barrier, V_{Bi}, that limits flow into the metal. This barrier can be reduced by applying a positive voltage to the metal to enable thermally excited electrons to flow, creating a forward bias current. In practice the formation of this barrier height is not trivial, it is often very dependent on the actual surface involved. Both iron and aluminum, whose work functions are larger than the electron affinity of ZnO, form ohmic contacts with ZnO due to complicated energy level interaction.

Conversely, the barrier height can be increased by applying a negative bias voltage to the metal substrate. Ideally, as the negative bias increases, conduction through

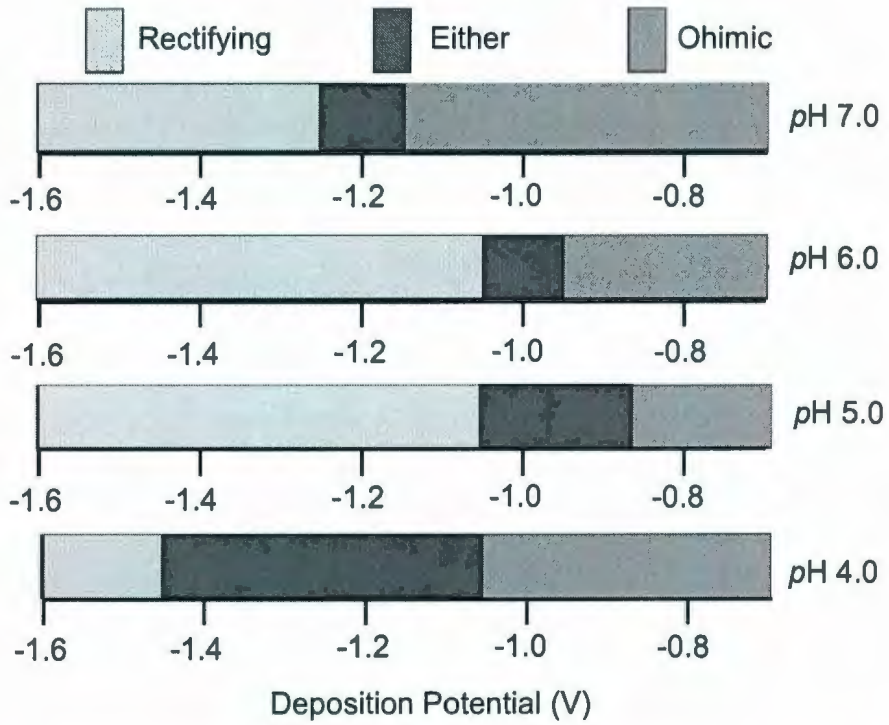

Figure 6.5: The deposition potential ranges for forming ohmic or rectifying ZnO/steel junctions depend on electrolyte *p*H. In all cases, there is a range of voltages for which there is poor selectivity between Schottky and ohmic responses.

the junction will approach a limiting saturation current. In practice, however, very high voltages will cause a reduction in the barrier height leading to non-negligible breakdown current in the reverse direction. This current has been attributed to heating effects, tunneling, and impact ionization[140], as can be seen in Figure 6.4. This typically occurs at localized areas first, where the junction may be of lower quality, allowing breakdown current in a localized region (soft breakdown). This can be observed in *I–V* curves as a non-ohmic, non-exponential increase in reverse saturation current.

We analyzed the rectifying responses of electrodeposited ZnO/metal junctions

that were prepared at different bulk electrolyte *p*H values and deposition potentials, summarized in Figure 6.5. Our experiments encompassed the viable *p*H range for the ZnO electroprecipitation reaction: for *p*H values ≥ 7, spontaneous precipitation of $Zn(OH)_2$ interferes with ZnO formation[39], while *p*H values ≤ 3.5 yield substantial Zn metal deposition that degrades the integrity of the semiconducting pathway through the sample. Figure 6.5 shows that ohmic ZnO/substrate contacts form at more positive deposition potentials (with resistances of 1-10 Ω), while rectification occurs in samples prepared at more negative deposition potentials (with resistances of 10^5-10^6 Ω), consistent with earlier findings[40]. There is also an intermediate range of deposition potentials for which either ohmic response or poor rectification (with pronounced soft breakdown) can result; in other words, there is poor selectivity between linear and rectifying behaviors for these deposition potentials. Nevertheless, the current-voltage response of any single sample is repeatable and does not change over time. A comparison of representative rectifying responses for samples prepared from electrolytes with different *p*H values is shown in Figure 6.6.

There are several factors that likely contribute to the inferior quality of the rectifying responses at the intermediate deposition potentials; all are linked to conditions that can perturb the formation of the Zn-rich ZnO/substrate interface that causes the rectifying junction behavior. First, a more acidic bulk electrolyte *p*H will shift the Nernst potentials of the nitrate reduction (Equation 2.4) and hydrogen evolution reactions to more positive values. Assuming a fixed deposition potential, these

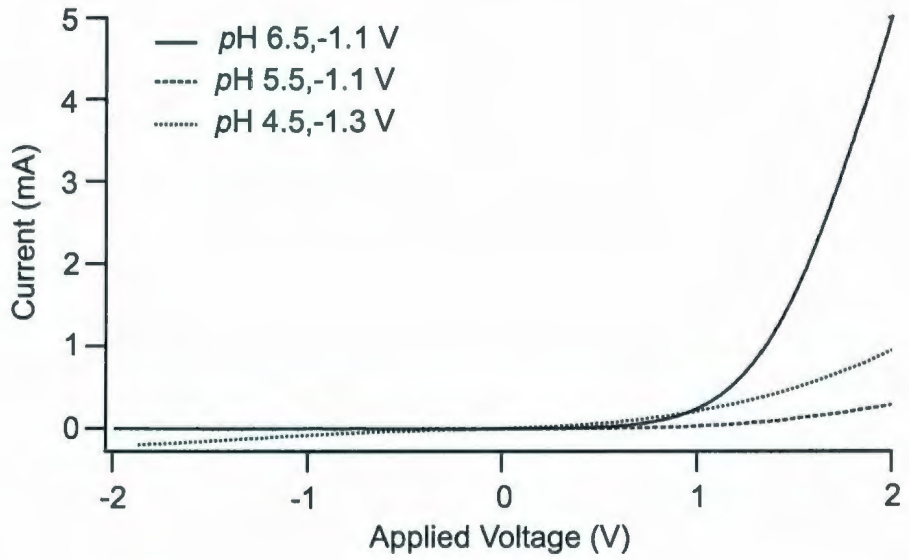

Figure 6.6: Representative I–V sweeps on electrodeposited ZnO Schottky junctions show stronger rectification and less soft breakdown with an increase in deposition electrolyte pH from 4.0 to 6.5. A representative I–V curve for pH 7.0 would coincide with the data for pH 6.5, so it is omitted for clarity.

Nernst potential changes lead to an increased rate of OH^- production near the working electrode surface, and these more alkaline conditions would promote ZnO formation. However, acidic electrolytes also promote metal formation, independent of these Nernst potential changes. The competition between these two factors (localized pH increase to favor ZnO formation, and acidic bulk pH to favor Zn metal formation) at the initial stages of electrodeposit formation could lead to differences in the Zn content at the ZnO/substrate interface among different samples. SEM and EDX investigations show that these compositional changes appear to be confined to within 50 nm of the ZnO/substrate interface, which corresponds to a very small fraction of the overall electrodeposit (thicknesses $\sim$ 2 μm). Thus, XRD measurements that

probe the entire sample would not be expected to show evidence of significant Zn content, consistent with Figure 6.1.

For a more quantitative comparison, pH -dependent rectification data (like those shown in Figure 6.6) were fit to the Schottky relation given in Equation 6.1.

$$J = A^* \, T^2 \exp\left(\frac{-e\Phi_B}{kT}\right) \exp\left(\frac{e(V - IR)}{nkT}\right) \tag{6.1}$$

This expression describes the idealized exponential increase in forward current with increasing forward bias voltage[20, 86, 89], where J is current density, e is the electron charge, I is current, k is Boltzmann's constant, V is voltage, R is the series resistance, T is temperature, n is the ideality factor, and A^* is Richardson's constant (32 A/cm^{2}K^2). Table 6.1 provides a summary of Schottky barrier heights and ideality values determined by fitting collected data to Equation 6.1. Also included are rectifying ratios, which give the relative magnitudes of the forward bias (+2 V) and reverse bias (-2 V) currents.

A linearized form of the Schottky equation has also been used by others to extract the ideality and Schottky barrier from the linear portion of the I–V curve before significant forward current flows [141].

$$\ln(J) = \frac{e}{nkT}(V - IR) - \frac{e\Phi_B}{nkT} + \ln(A^* \, T^2) \tag{6.2}$$

For our samples, the linearized Schottky analysis technique provided data consistent with the ideal Schottky equation but with larger uncertainties, due in part to fitting

pH	n	Φ_{B0}	Rectifying ratio	Resistance (ω)
4.0±0.25	15 ± 5	0.80 ± 0.04	6 ± 4	~ 1
5.5±0.25	13 ± 5	0.73 ± 0.05	100 ± 20	$10^5 - 10^6$
6.5±0.25	13 ± 5	0.85 ± 0.03	1000 ± 200	$10^5 - 10^6$
7.0±0.25	13 ± 5	0.85 ± 0.03	1000 ± 200	$10^5 - 10^6$

Table 6.1: Data obtained from fitting rectifying current-voltage responses in samples prepared from electrolytes with different pH values to the ideal Schottky equation. The highest rectifying ratios occur in junctions prepared from electrolytes near neutral pH. Uncertainties were estimated from the standard deviation of the average experimental value.

fewer data points. Therefore, only data fit to the ideal Schottky equation is included in Table 6.1.

Rectifying ratios show a dramatic increase for junctions prepared in less acidic deposition electrolytes (Figure 6.6). Regardless of electrolyte pH, Schottky barrier heights for our electrodeposited ZnO junctions compare well with values for junctions synthesized by other methods[17, 20, 86, 89]. Ideality (n) values for all electrodeposited Schottky junctions are greater than 2, indicating multiple conduction pathways[17, 82].

It is not entirely clear why the more acidic electrolytes yield samples with more soft breakdown and correspondingly lower rectifying ratios. Scrutinizing the XRD data for pH -dependent differences in preferred orientation (from peak height comparisons) or particle size (from peak broadening) did not yield an obvious correlation across the entire range of pH values studied, nor do optical absorption edge data offer additional

insights. However, we did observe that deposits prepared at the most acidic *p*H values (4.0) showed a substantial decrease in the (002) orientation that is widely observed in ZnO electrodeposits[16, 39, 60, 95]. We also observe that rectifying junctions prepared from the most acidic electrolytes have the lowest resistances ($\sim$1 Ω at *p*H 4 compared to $\sim 10^5$ Ω at *p*H 6.5).

Based on these investigations of junction performance as a function of electrodeposition conditions, we conclude that deposits prepared from *p*H 6.5 electrolytes show the best diode functionality without the risk of spontaneous $Zn(OH)_2$ precipitation. Thus, all subsequent data is presented for electrodeposits prepared from electrolytes with this *p*H using a deposition potential of –1.1 V.

6.4.3 Humidity Effects on Rectification

Previous studies have indicated that ZnO/CuO based rectifying *pn* junctions, which are operationally similar to Schottky junctions, are sensitive to changes in relative humidity when forward biased[134]. The humidity-dependent responses of this and similar systems[129, 132] has been attributed to water electrolysis at the positive and negative sides of the junction. A schematic diagram of the water electrolysis reaction, given in Figure 6.7a, depicts the oxidation and reduction reactions that occur at the anode and cathode, respectively. For comparison, Figure 6.7b shows that water vapor can adsorb to the ZnO/air interface, and this water can be electrolyzed when the ohmic compression contact acts as a cathode while the ZnO acts as an anode

(forward bias condition).

$$\text{(at ZnO)} \quad 2H_2O \leftrightharpoons O_2 + 4H^+ + 4e^- \tag{6.3}$$

$$\text{(at metal)} \quad 2H^+ + 2e^- \leftrightharpoons H_2 \tag{6.4}$$

The protons generated at the anode diffuse and can be reduced to hydrogen by electrons at the cathode surface. Combining current responses due to the ideal Schottky junction conduction (Equation 6.1) with the electrolysis-generated proton conduction yields a total current density expression with three components:

$$J = A^* T^2 \exp\left(\frac{-e\Phi_B}{kT}\right) \exp\left(\frac{e(V - IR)}{nkT}\right) + Ck_f[H_2O]^{\frac{1}{2}}[H^+] - Ck_r[O_2]^{\frac{1}{4}}[H^+], \tag{6.5}$$

where C is a constant, and k_f and k_r are the forward and reverse reaction rates from Equations 6.3 and 6.4. The second term in Equation 6.5 is due to the physisorbed water electrolysis and increases with both humidity and voltage increases. The third term counteracts the forward bias current and is due to the oxygen partial pressure of the system[134]. The rectifying behavior of the Schottky contact ensures that there is little reverse bias current, even in the presence of water electrolysis. We note that relative magnitudes of the protonic conduction, based on electrolysis and charge movement through adsorbed water, and the Schottky (thermionic emission) current are dependent on applied bias voltage. In our samples, the current resulting

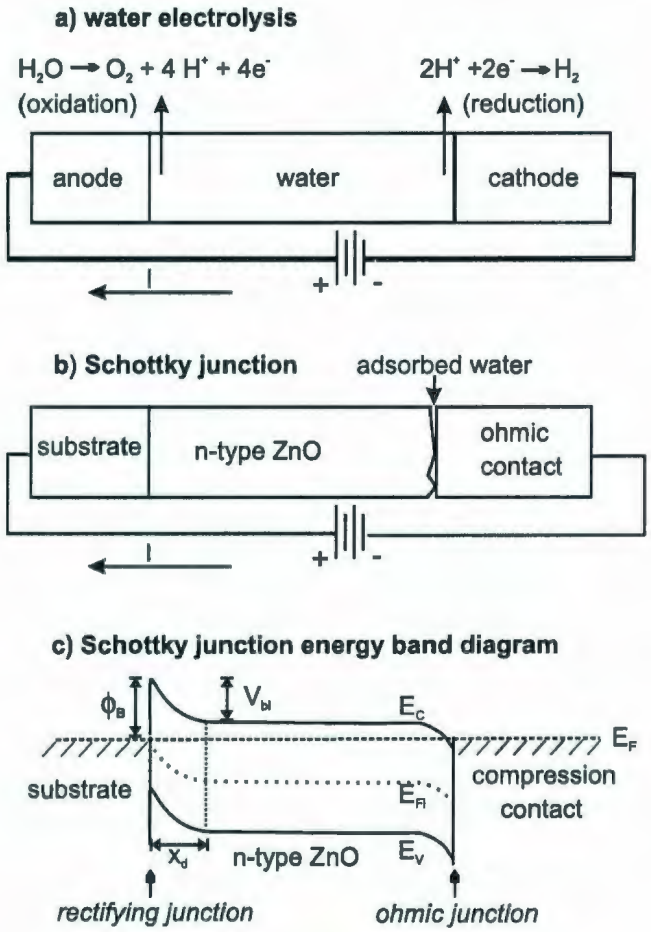

Figure 6.7: Schematic diagrams illustrate (a) the water electrolysis reaction that can occur between two metal electrodes, and (b) where the water electrolysis reaction occurs in the electrodeposited Schottky junctions (in the water adsorbed at the ZnO/air interface). The corresponding junction energy band diagram (c) emphasizes that the rectifying junction occurs at the ZnO/substrate, while an ohmic contact exists between the ZnO/air interface and the metal compression contact.

from the electrolysis-generated proton conduction ($\sim$ 10 mA) greatly outweighs the contribution of the Schottky current ($\sim$ 10 – 100 μA). Due to the polycrystalline nature of our samples, grain boundary contributions dominate the electrical resistance of our samples relative to the thickness-dependent resistance of the ZnO itself. This fact, in conjunction with the surface-based water electrolysis mechanism, implies that the details of the ZnO/air interface are more important for the magnitude of the forward current flow (which can vary by an order of magnitude, from 100 to1000 μA) than film thickness (with smaller percentage uncertainties of 1.0 ± 0.2 μm).

Figure 6.8 illustrates the role that humidity plays in the quality of the rectifying response in electrodeposited ZnO Schottky junctions. For low humidities ($\leq$ 50%), Schottky junctions show I–V sweeps with minimal signs of soft breakdown at reverse bias and good rectifying ratios ($\sim$1000). However, higher relative humidities lead to noticeable signs of soft breakdown at reverse bias, as well as increased noise at forward bias. At the highest humidities ($>$ 70%), the forward current can also show erratic responses, in both direction and magnitude, to humidity changes. Nevertheless, the ZnO electrodeposits display excellent adherence to the substrate, even with repeated cycling to high (75-95%) relative humidities. There were no other visible signs of sample degradation, such as color changes[135], upon repeated exposure to high relative humidities and bias voltages.

While these electrodeposited junctions do exhibit humidity-sensitive I–V responses under sweeping voltage conditions for constant relative humidities, they do not

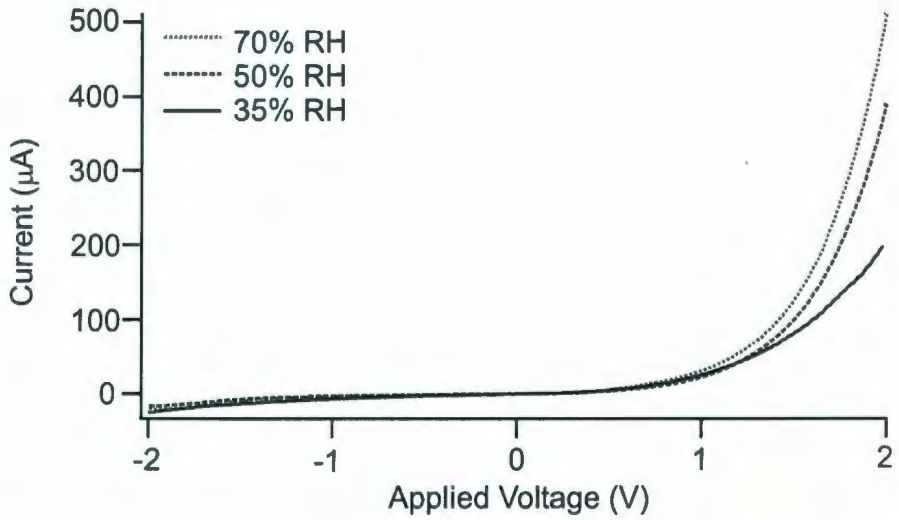

Figure 6.8: *I–V* sweeps on electrodeposited Schottky junctions show larger forward bias currents at higher relative humidities.

function effectively as traditional humidity sensors that operate at a fixed bias voltage in changing relative humidity environments. For example, although abrupt current changes are observed in junctions forward biased at 1–2 V when exposed to intervals of alternating 50% and 80% relative humidities, there is also substantial drift in the current in between these humidity changes. Thus, it is not possible to calibrate the junction so that a specific current indicates a specific relative humidity value. Additional details, including a representative plot of current *vs.* time for junctions exposed to different relative humidities, is provided in Section 6.6.

For completeness, we note that ohmic electrodeposited ZnO/substrate junctions are also affected by humidity, but the effects are much less pronounced. The humidity-dependent increase in resistance is $\leq 1\%$ (1–5 Ω) for ohmic samples cycled between 15% and 80% relative humidity. In the context of the water electrolysis mechanism

described above, proton conduction ($\sim$ 10 mA) is negligible compared to the larger currents that can flow through the lower-resistance ohmic samples (400–600 mA at 2 V), leading to a much weaker humidity-related effects.

6.4.4 Surface Coating Effects on Rectification

Since erratic current responses in our junctions are more prevalent at high relative humidities, it is possible that this problem is due to a dynamic contact area between the ZnO and metal pressure contact as more water vapor adsorbs and begins to condense at the junction for the highest humidity levels. (This effect could be separate from the water electrolysis-based degradation that has been observed in other ZnO-based devices[135].) To this end, we investigated the effect of thin surface coatings, applied post-electrodeposition, at the ZnO/air interface.

Hydrophobic coatings and materials have been widely studied recently, but there has been little focus on the role that hydrophobicity can play in controlling the electronic response of ceramic rectifying junctions. Some reports have used hydrophobic coatings to preserve the integrity of humidity sensitive polymers[142, 143]. Our results suggest that this is an avenue worth investigating to control the quality of the rectifying response in junctions that may be adversely affected by changes in relative humidity.

We find that adding a hydrophobic coating, to change the way that water adsorbs and condenses the ZnO/air interface, can lead to improved rectifying responses of our

junctions. Best results were obtained by applying a thin layer of aliphatic petroleum distillates (Stoddard solvent, mean molecular weight 144 g/mol, dissolved in a 1:10:10 mixture of xylene, propane and butane, Kiwi Outdoor Camp Spray). These layers accentuate the natural hydrophobicity of our ZnO electrodeposits. (This hydrophobicity, consistent with other reports[144], is due in part to the surface roughness of the electrodeposits[16, 40].) Assessments of coating continuity and thickness using AFM showed that the hydrophobic layers appear continuous on length scales greater than $\sim$ 100 nm and typically vary in thickness from 10–60 nm. Pooling of the coating mixture does occur in deep features of the deposit, leading to substantially thicker coatings in some places.

Figure 6.9 shows that electrodeposits with these coatings exhibit less soft breakdown at high relative humidities (50-70%), and rectifying ratios that are comparable to those observed at lower humidities. At the highest relative humidities ($\geq$ 85%), it is still possible to observe erratic changes in current, but the magnitude of the changes are much smaller than for uncoated junctions.

The continuity and thickness of the hydrophobic coating can impact how effectively it suppresses soft breakdown in the junctions at higher relative humidities. For example, thin layers of silicone (applied in a manner similar to the petroleum distillates) did not coat the junctions as uniformly, leaving some exposed regions. The corresponding Schottky responses showed somewhat improved rectification over uncoated samples, but more soft breakdown occurred relative to the data shown

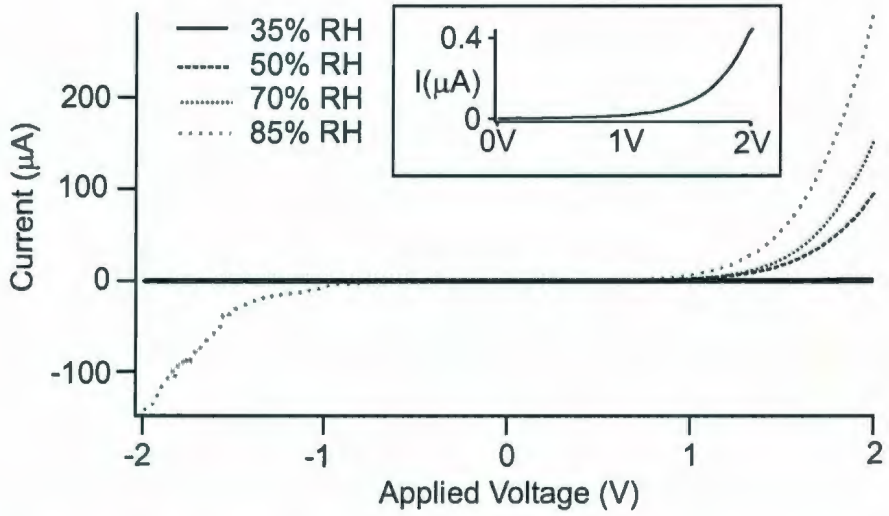

Figure 6.9: Sprayed hydrophobic coatings reduce soft breakdown, except at the highest relative humidity values ($\geq$ 85%). The inset shows the same data with a smaller current scale to emphasize the rectifying nature of the I–V response at 35% RH.

in Figure 6.9. In other experiments, more complete electrically insulating coatings were applied by submersing junctions in a solution of 5 mM octadecyltrichlorosilane (OTS) in toluene while confined to a dessicated glove box, following a method reported earlier[144]. This procedure yielded coatings whose continuity and thickness were comparable to the sprayed coatings, according to AFM investigations. However, through-sample resistances were prohibitively high (0.5–50 MΩ) and unstable, suggesting that the coatings acted as electrical insulation between the ZnO and metal compression contacts. For all silicone and OTS coated samples, removal of the coatings with ethanol or acetone restored the original rectifying behavior. The current *vs.* time trends during exposure to different relative humidities for representative coated and uncoated junctions is provided in Section 6.6.

For comparison, we also addressed the effect of metallic coatings that still preserve enough surface roughness to allow the samples to remain hydrophobic. Aluminum (65 ± 15 nm or 200 ± 30 nm thicknesses) were thermally evaporated at 10^{-3} torr onto rectifying ZnO deposits. After coating, sample resistances fell from $\sim 10^6\ \Omega$ to $\sim 1\ \Omega$, eliminating the rectifying responses. Although cross-section SEM shows that our films are largely continuous, these resistance measurements suggest that aluminum may permeate pinholes in the film (Figure 6.2a), bypassing the conduction pathway through the bulk ZnO and effectively short-circuiting the Schottky junction. Aluminum could also be in contact with the ZnO depletion layer, which would adversely affect the desired Schottky band bending at the ZnO/metal substrate interface.

6.5 Conclusions

The quality of the rectifying responses in electrodeposited ZnO/metal junctions, including the magnitude of currents during forward bias and soft breakdown effects during reverse bias, can be optimized by adjusting the deposition potential and the bulk electrolyte *p*H. These two parameters can be used to control the propensity to form the Zn-rich interface (during the initial stages of film growth) that most likely causes the rectifying behavior. Additionally, hydrophobic coatings at the ZnO/air interface can further decrease soft breakdown and improve the rectifying ratios at moderate relative humidities, if the coatings are both continuous and do not elec-

trically insulate the ZnO from the ohmic compression contact. We expect that this use of post-deposition surface coatings could be relevant for other inorganic materials and devices whose electronic operation is degraded in humid or wet environments.

6.6 Supporting Information

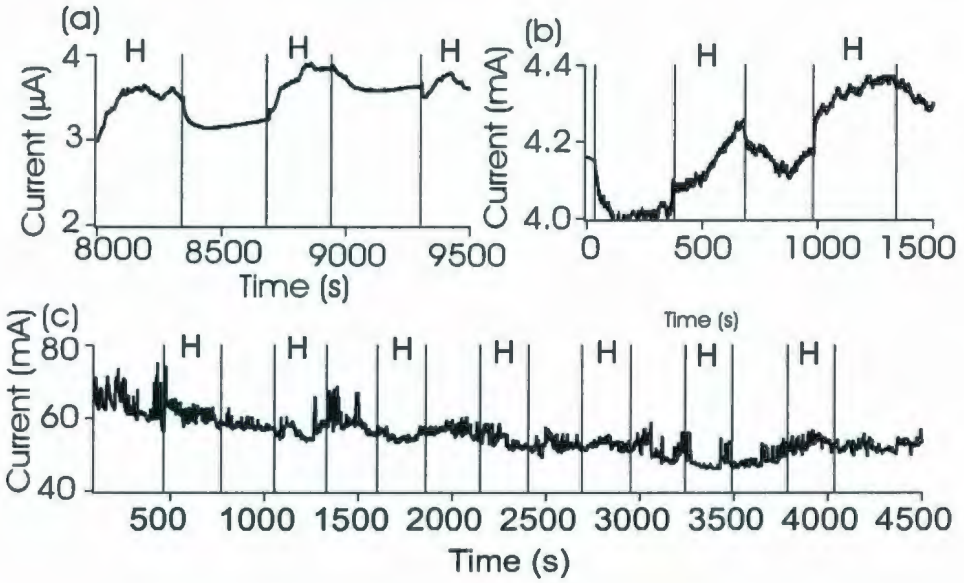

Figure 6.10: Current-time plots for ZnO/metal junctions during controlled humidity tests. Relative humidity was cycled between between 80% (labeled "H") and 50% at 5 minute intervals while applying -1 V for as deposited samples (a), samples coated in petroleum distillates (b), and samples coated in OTS. All junctions were prepared from electrolytes with *p*H 6.5 at -1.1 V *vs.* $Ag/AgCl_{sat'd}$.

Although electrodeposited ZnO-based Schottky junctions exhibit humidity sensitive current-voltage responses under sweeping voltage conditions for constant relative humidities, they do not function effectively as traditional humidity sensors that operate at a fixed bias voltage in changing relative humidities. Abrupt current jumps

(10-20%) occur when relative humidity levels change between 80% (labeled "H") and 50% at 5 minute intervals and 1 V forward bias (Figure 6.10a). However, substantial signal drift (most likely due to changing ZnO/water/probe geometries and sample degradation) prevents calibrating the junction so that a specific current indicates a specific relative humidity value. Samples sprayed with a coating of petroleum distillates also showed signal drift, but with slightly less sensitivity to humidity changes (2-3% current changes) and improved rectification (Figure 6.10b). Samples coated with an electrically insulating octadecyltrichlorosilane (OTS) layer show virtually no susceptibility to changing relative humidity conditions, along with noisier data due to prohibitively large contact resistances (0.5-50 MΩ) (Figure 6.10c).

Chapter 7

ZnO/Cu_2O Heterojunctions

Developing practical and novel electronic devices has been a main goal of semiconducting materials science. One of the promising applications that drives semiconductor research is high efficiency photovoltaic devices to convert solar radiation into electrical energy. The classic photovoltaic device uses extrinsically doped semiconductor *pn* homojunctions in order to achieve this feat. As proof-of-concept, we studied the photovoltaic characteristics of ZnO/Cu_2O *pn* heterojunctions.

7.1 Bilayer *pn* Junction Consideration

A junction between an n-doped and a p-doped semiconductor is the classic example of rectifying non-linear device (Figure 7.1) When an n-doped semiconductor and a p-doped semiconductor are brought together, there is a movement of charge carriers as electrons diffuse into the p-doped side, and holes diffuse into the n-doped

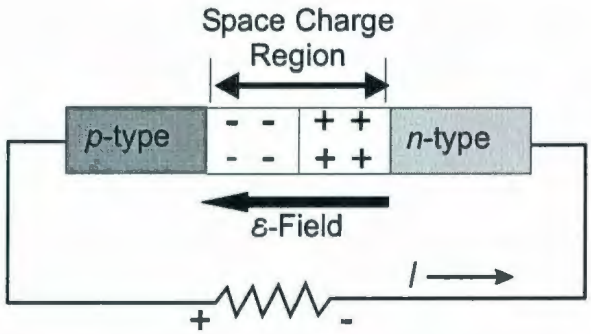

Figure 7.1: This diagram illustrates the doped regions of a *pn* junction. The space charge (depletion) region occurs near the $n - p$ interface.

side, creating a space charge depletion region and an induced electric field (Figure 7.1).

When a photon is absorbed in the space charge region, or within a diffusion length of the junction, an electron-hole pair is created. This electron moves to the n-type side due to the induced electric field, creating a greater charge imbalance between the n and p-type sides, and a photo-generated current. The resultant photo-current can do work on a resistive load while trying to equalize the charge imbalance.

Current through *pn* junctions is governed by an exponential expression relating current density to the applied voltage, similar to the Schottky barrier expression:

$$J = J_s \left[\exp\left(\frac{e(V_a)}{kT}\right) - 1 \right]. \tag{7.1}$$

Here, J_S is the saturation current density and is given by:

$$J_S = \frac{q\ D_p\ p_{n0}}{L_p} + \frac{q\ D_n\ n_{p0}}{L_n}, \tag{7.2}$$

wherein D_p and D_n are the minority-carrier hole and electron diffusion coefficients (cm/s), p_{n0} and n_{p0} are the thermal equilibrium minority-carrier hole and electron densities (cm^{-3}), and L_p and L_n are the minority-carrier diffusion lengths (cm). At applied voltages more negative than a few kT/qV, the current saturates.

Heterogeneous *pn* junctions (comprised of two different materials) have been studied extensively for use in photovoltaic devices[44]. They offer the ability to increase the efficiency of solar cells over homojunctions by exploiting a larger range of energies present in solar light[145]. As with the synthesis of single layer semiconductor devices, electrodeposition of *pn* junctions offers the possibility of multi-layer semiconductor structures at low temperature and atmospheric pressure.

ZnO/Cu_2O heterojunctions offer multiple advantages over the synthesis of highly toxic chalcogenide semiconductor heterojunctions[146]. Both ZnO and Cu_2O are relatively non-toxic materials that can be electrodeposited in an aqueous solution at low temperatures without annealing. They are also both natively doped. ZnO is natively *n*-type due to interstitial hydrogen doping with donor energies just below the conduction band (see Chapter 5) while Cu_2O is universally accepted as natively *p*-type due to copper vacancies with acceptor energies 0.4 eV above the valence band.[146].

Here, we study the electrochemical synthesis of heterogeneous ZnO/Cu_2O *pn* junctions using a "two bath" technique. The ideal electrochemical *pn* junction synthesis procedure would use a single aqueous bath to deposit both materials sequentially[95]. However, utilizing two electrochemical baths to deposit the semiconducting single

layers still reduces the complexity and cost of the synthesis procedure over UHV techniques[95, 146].

ZnO/Cu_2O junctions can be formed in two permutations: ZnO/Cu_2O/substrate (ZCS) and Cu_2O/ZnO/substrate (CZS), as illustrated in Figure 7.2[46]. Previous studies have shown that photovoltaic cells created using the CZS structure show higher efficiencies than the ZCS structure when synthesized using reactive radio-frequency magnetron sputtering[46] due to a reduction in lattice mismatch (7.1%) between the (001) preferred orientation of ZnO electrodeposits and the cubic (111) Cu_2O [46, 147]. While this lattice mismatch is high with respect to some *pn* heterojunctions (Ge/Si is 4.1%), this lattice mismatch reduction between certain faces is still a promising avenue of investigation[46, 147]. We attempted both permutations using electrodeposition to test the performance of these different layer geometries.

In order to increase the efficiency of solar cells, it is advantageous to create *pn* junctions from materials with different band gaps[18, 43, 44, 145, 146]. In our work ZnO, with the wider band gap (3.3 eV *vs.* 2.0 eV), was the window material[146] to absorb higher energy photons and to allow lower energy photons to reach the Cu_2O layer[18, 43, 44]. As a result, it is important for the layers to be deposited in a way that lets light reach the Cu_2O while still ensuring electrical contacts with the ZnO and Cu_2O. This can be achieved with transparent conducting substrates like indium tin oxide or a vapour deposited copper grid, as is often used with silicon photovoltaic cells[65]. Unfortunately, the copper grid blocks some of the semiconductor surface

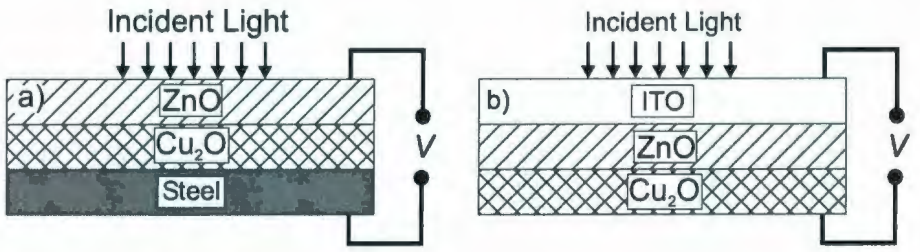

Figure 7.2: These two diagrams indicate two different multi-layer structures that allow light to reach the *pn* junctions. (a) shows steel substrate where Cu_2O is deposited first, and then a ZnO layer is deposited on top of it. (b) shows ZnO deposited on indium tin oxide (ITO), with a layer of Cu_2O deposited on top. The electrical contacts to the heterojunctions are indicated for each multi-layer structure.

area, reducing possible efficiency[18].

Indium tin oxide (In_2O_3:Sn_2O, ITO) vapour deposited on glass microscope slides were chosen as our transparent conducting substrate. ITO is a wide-bandgap, natively *n*-type semiconductor, that also offers transparent mechanical support when deposited on glass. This allows an intimate contact between ZnO and the top (light incident side) substrate without blocking any of the ZnO surface. The bottom contact can be made with either a compression or evaporated metal contact.

7.2 Electrodeposition of ZnO and Cu_2O for *pn* Junctions

7.2.1 ZnO Layer Synthesis

While *pn* junctions exhibit rectifying *I–V* scans, each individual component layer should display low-resistance ohmic behaviour. In order to ensure such response from

ZnO layers, single layers were deposited at -0.9 V *vs.* $Ag/AgCl_{sat'd}$ in an electrolyte consisting of 10 mM $Zn(NO_3)_2$ + 0.5 mM NaOH (*p*H 6.5) as outlined in Chapter 5, on either ITO substrates, stainless steel substrates, or pre-deposited Cu_2O/steel junctions (see Section 7.3).

7.2.2 Cu_2O Layer Synthesis

Unlike the multi-step synthesis of ZnO, the electrodeposition of Cu_2O involves a straight-forward reduction-oxidation reaction. Copper (I) oxide films were deposited using a net cathodic (reducing) current[45, 54, 55, 56, 57]:

$$2Cu^{2+} + 2e^- + H_2O \rightleftharpoons Cu_2O + 2H^+ \tag{7.3}$$

The cathodic reduction of Cu^{2+} to Cu^+ at the working electrode surface has an equilibrium potential of -0.163 V *vs.* $Ag/AgCl_{sat'd}$ (at pH 7, 25 °C, and 1 atm). This is illustrated in the Pourbaix diagram seen in Figure 7.3. Note that the potential region for Cu_2O stability is much smaller and more *p*H dependent than for $Zn(OH)_2$ stability (Figure 2.1). Consequently, achieving the conditions for phase-pure Cu_2O formation is challenging.

Cu_2O films were synthesized using electrolytes containing 5 mM $CuSO_4 \cdot 5H_2O$ (Sigma-Aldrich ACS grade reagent). Supporting electrolytes were used to adjust the *p*H and to enable Cu^{2+} ion complexing. The complexing of the Cu^{2+} ions with acetate, tartrate, or lactate ions is required to increase the stability of Cu^{2+} within

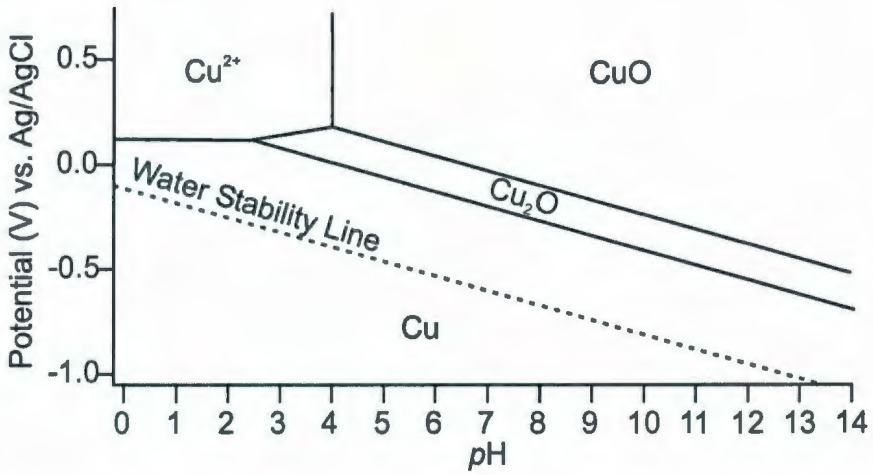

Figure 7.3: Diagram indicates the potentials and pH regions in which Cu, Cu^{2+}, CuO, and Cu_2O are stable. This schematic diagram, based on thermodynamic calculations of phase stabilities at STP (25°C and 1 atm)[49]. This is used as a general guideline when determining synthesis conditions, as they do not include the effect of supporting electrolytes, temperatures and pressures other than STP, electrode stability, *etc.* The dashed lines indicate the lower limits of stability for water; below the dashed line, hydrogen will be evolved.

solution as pH is adjusted[45, 148]. If the Cu^{2+} is not complexed, it will reduce to Cu^{+} in solution at high pH values, thereby blocking the electrodeposition of Cu_2O by Equation 7.3. To create neutral pH electrolytes, 0.25 – 1.0 M potassium acetate (KCH_3COO) was added as a complexing agent with slight buffering capability[57]. To create more alkaline electrolytes, L+ tartaric acid (0.3 M)[149] and lactic acid (0.3-3 M)[54, 150, 151] were utilized. These were used in conjunction with NaOH to adjust the pH level between 9 and 12. All depositions were carried out at 60°C in a three-electrode cell with no Ar or N_2 purging.

X-ray diffraction analysis was used to confirm the identity of electrodeposited Cu_2O (body-centered cubic crystal structure with space group $Pn3m$), as well as to

determine any preferred orientation (Figure 7.4). Samples deposited potentiostatically between -0.050 V and -0.400 V with both neutral and alkaline electrolytes contained peak structures consistent with Cu_2O (JCPDS #05-0667)[11]. Using all peaks distinct from the stainless steel substrate (5-6 peaks) for the linear least squares refinement, the average cubic lattice constant was $a = 4.272 \pm 0.003$ Å, in agreement with other reports in the literature 4.27 Å[11]. No significant changes in lattice constants occur in samples deposited at different pH values. Cu_2O deposited from neutral pH electrolytes exhibited a light orange colour with a metallic sheen, possibly indicating copper metal incorporation. Unfortunately, copper metal content cannot be determined definitively from our XRD data, as the substrate peaks overlap with expected Cu metal peaks. Samples deposited with the alkaline electrolytes did exhibit a deep red colour, consistent with Cu_2O [11].

Diffuse reflectance UV/Visible spectroscopy was also used for phase confirmation in electrodeposited Cu_2O samples. The absorption edge of collected spectra indicate that the band gaps of our electrodeposited Cu_2O samples were in the range of 2.09–2.2 eV, which is in agreement with the reported values for $p-$type Cu_2O (2.0-2.2 eV)[46, 152]. Representative diffuse reflectance data of both Cu_2O and ZnO can be seen in Figure 7.5. An analysis of diffuse reflectance data indicated that deposition potential had no discernible influence on the bandgap of the electrodeposited samples.

An analysis of electrical conduction through electrodeposited Cu_2O/metal junctions showed ohmic behaviour (Figure 7.6) for applied voltages between -2.0 V and

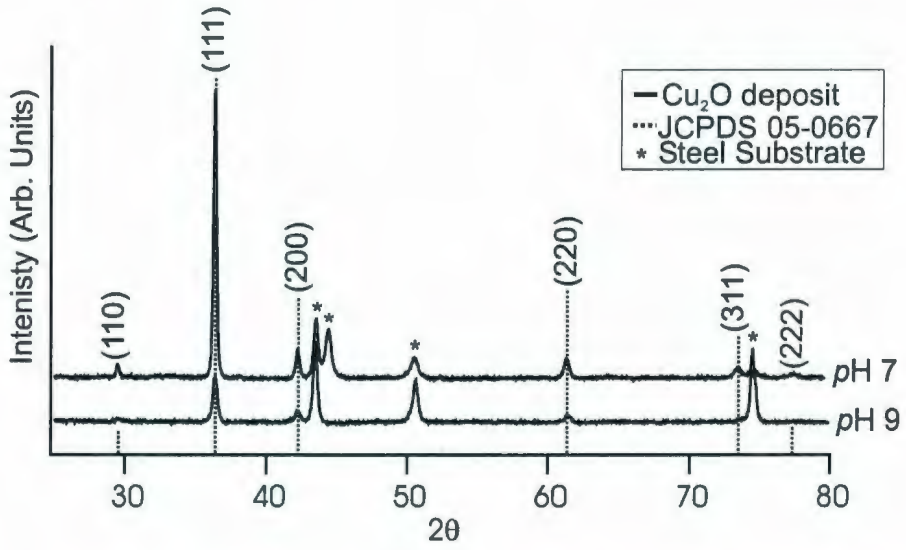

Figure 7.4: Representative indexed XRD patterns from electrodeposited Cu_2O prepared with either the acetate based electrolyte (pH 7) or the tartaric acid based electrolyte (pH 9). Lattice constant analysis of these data indicate an experimental lattice constant of $a = 4.272 \pm 0.003$ Å, commensurate with the accepted value of 4.27 Å[11]. The extra substrate peak near 44° (2θ) in the data collected from samples deposited in the acetate based electrolytes are indicative of the 316 series steel (as compared to the A-286 series used with the tartaric acid based electrolytes).

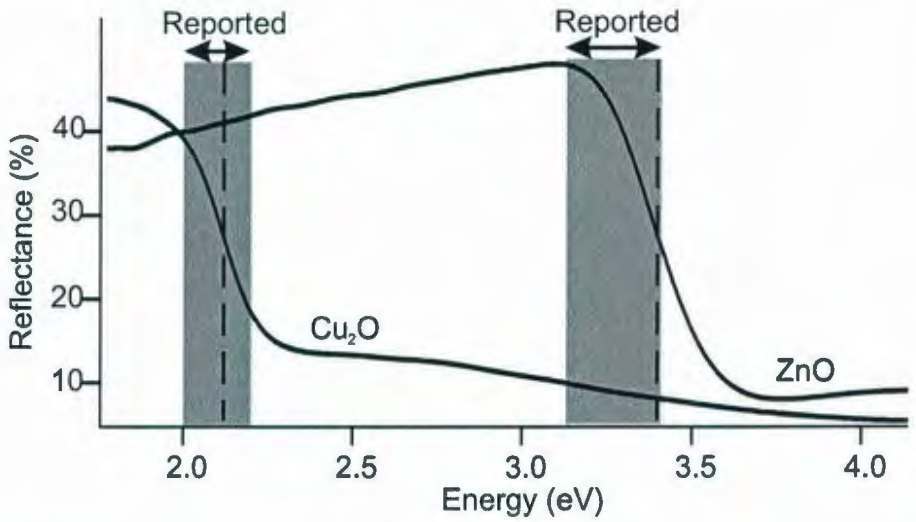

Figure 7.5: Representative diffuse reflectance spectra of electrodeposited Cu_2Ocan be compared with a typical diffuse reflectance spectra obtained from our electrodeposited ZnO. The dashed lines represent the bandgap calculated from these specific curves (2.12 eV for Cu_2O and 3.40 eV for ZnO) and their position within the reported values of each material (2.0-2.2 eV for Cu_2O and 3.1-3.4 eV for ZnO).

2.0 V. Linear I–V behaviour is expected because Cu_2O has an electron affinity (1.235 eV)[153] smaller than the typical work function of steel ($\approx$ 5 eV). The resultant barrier height across a Cu_2O/steel junction would be negative, causing an ohmic junction. The through-film resistances were $1 - 10\ \Omega$ over a contact area of 0.18 cm^2, as determined by 2-probe electrical measurements.

7.3 Multilayer Synthesis

To synthesize multilayer junctions, either ZnO or Cu_2O was deposited on the chosen substrate, deposits were rinsed in ultrapure water, and then dried in a flowing argon stream. Low-resistance ohmic contacts were confirmed before proceeding. The

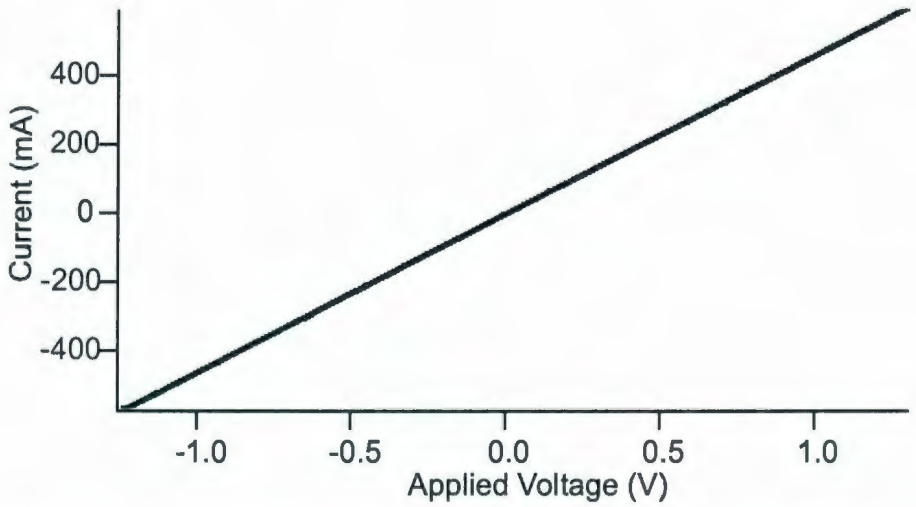

Figure 7.6: Typical I–V scan of a Cu_2O /steel sample. This sample was deposited at -0.4 V in 5 mM $CuSO_4 \cdot 5H_2O$ + 1.0 M KCH_3COO. Note the ohmic behaviour and associated resistance $\sim 1\ \Omega$.

second layer was then deposited in the same manner as if they were single layers, but with a slightly smaller deposition area (Figure 7.7) to prevent a direct electrical pathway between the second layer and the substrate. After deposition, the multi-layer structure was cleaned in ultrapure water and under flowing argon. The general findings of these experiments are summarized in Table 7.1.

Acetate Electrolyte

Both Cu_2O/ZnO/steel and Cu_2O/ZnO/ITO samples were prepared with the acetate electrolyte for the Cu_2O synthesis step. Cu_2O layers deposited on ZnO using this electrolyte were uniform and well-adhered, with complete coverage of the ZnO layer. However, the reverse ordering (ZnO/Cu_2O/substrate) permutations could not be synthesized repeatably due to inconsistent coverage.

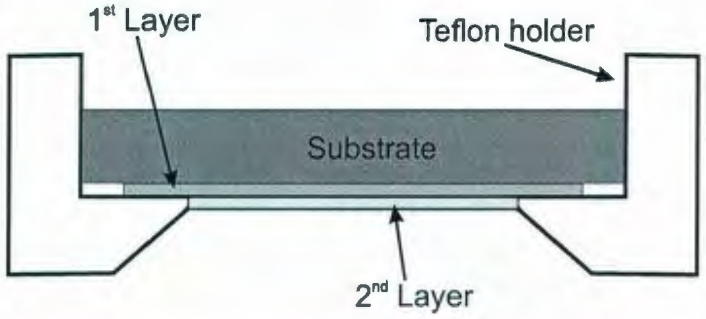

Figure 7.7: Schematic diagram of the Teflon holder used to deposit multilayer samples. When the second layer is being deposited, the electrolyte is only in contact with the first layer, not the original substrate.

Cu-based Electrolyte	Cu_2O/ZnO/substrate	ZnO/Cu_2O/substrate
acetate (acidic)	Cu incorporation	could not synthesize
tartaric acid (alkaline)	ZnO dissolution	could not synthesize
lactic acid (alkaline)	ZnO dissolution	light sensitive rectifying junction

Table 7.1: This table summarize the results of our ZnO/Cu_2O *pn* junction synthesis experiments.

I–V sweeps across Cu_2O/ZnO/ITO and Cu_2O/ZnO/steel samples exhibited non-linear, poorly rectifying current response, counter-indicative of *pn* junction formation. We suspect that this is due to copper metal incorporation within the Cu_2O layer due to its light orange colour. By considering the Pourbaix diagram (Figure 7.3), it is clear that copper metal formation is reasonable near the *p*H/potentials where Cu_2O is formed. Indeed, previous work has found that electrodeposited Cu_2O can include copper metal incorporation[138, 154, 155], and that the deposition of ZnO onto Cu_2O can reduce the Cu^+ in Cu_2O to Cu metal[94].

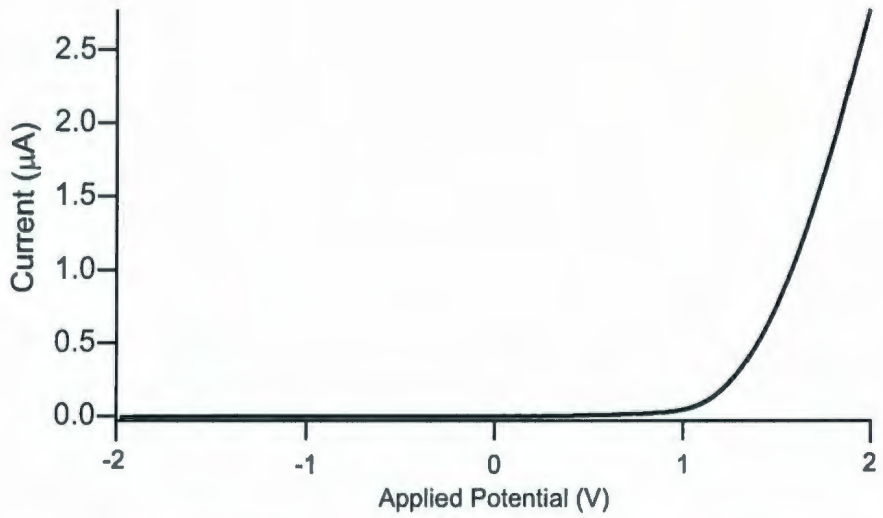

Figure 7.8: *I–V* sweep of an electrodeposited ZnO/Cu_2O/steel junction. The Cu_2O layer was deposited from the lactate electrolyte (*p*H 9) at -0.2 V, while the ZnO layer was deposited in 0.02 M $Zn(NO_3)_2$ + 0.05 mM NaOH (*p*H 6.5) at -0.9 V.

Tartaric Acid Electrolyte

Tartaric acid-based electrolytes (*p*H 9-12) were also used to form Cu_2O layers for Cu_2O/ZnO/ITO and ZnO/Cu_2O/steel multi-layer structures. Cu_2O could not be deposited on ZnO using tartaric acid-based electrolytes due to ZnO dissolution. ZnO also could not be deposited on Cu_2O synthesized in the tartaric acid electrolytes. It is possible that the Zn^{2+} adlayer could not form, or that the nitrate reduction could not occur due to some aspect of the Cu_2O crystal faces exposed to the solution. There is also a possibility that incorporated ions from the tartaric solution could also inhibit ZnO synthesis, although there is no evidence in the literature to support this.

Lactic Acid Electrolyte

For ZnO/Cu_2O/steel multi-layers prepared using the alkaline lactic acid electrolytes, ZnO deposits showed good coverage (approaching 100%). UV/Visible analysis of these structures confirmed the band gap of the ZnO layer (3.3 eV), and this layer was was thick enough to prevent any signal from the Cu_2O layer. *I–V* sweeps across these samples display typical rectifying *pn* junction behaviour (Figure 7.8). Cu_2O/ZnO/steel could not be synthesized with the lactic acid electrolyte due to its dissolution of ZnO. The formation of light-sensitive ZnO/Cu_2O/substrate junctions is contrary to the work of Akimoto *et al.*, who found that the ZnO/Cu_2O/metal permutation was not reliably rectifying. They concluded that the synthesis of rectifying light-sensitive Cu_2O/ZnO/substrate junctions was more favourable due to a diminishing of the lattice mismatch[46].

7.3.1 Photovoltaic Responses

The light sensitivity of synthesized *pn* junctions were tested with both swept potential and applied bias experiments. Analyzing *I–V* behaviour during exposure to light is the traditional way to calculate the efficiency of photovoltaic junctions[65]. The efficiency (η) is determined by finding the largest possible box that can be inscribed inside the "light current" *I–V* scan (Figure 7.9). The point (I_m, V_m) that maximizes the inscribed box is used to determine the efficiency:

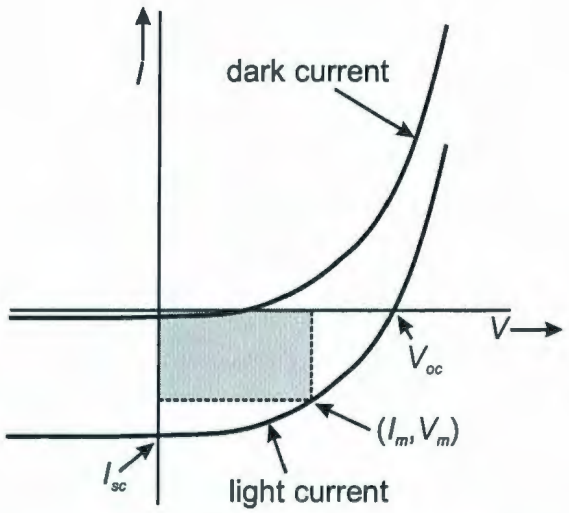

Figure 7.9: I–V sweeps of an ideal light sensitive pn junction. The shaded box indicates the maximum power output of the photovoltaic cell. I_{sc} (short circuit current) is the maximum current, and V_{oc} (open circuit voltage) is the maximum voltage drop that can be produced by the photovoltaic cell.

$$\eta = \frac{P_m}{P_{in}} \times 100\% = \frac{I_m V_m}{P_{in}} \times 100\%. \tag{7.4}$$

Here, P_m is the maximum power output ($I_m V_m$) and P_{in} is the power input from the light.

Our electrosynthesized pn junctions did not show appreciable light sensitivity in their I–V curves when exposed to room lights or white/blue LEDs. Due to a very small short circuit current, the low signal-to-noise ratio made it impossible to calculate an efficiency. Our efforts were impeded by a time-dependent drift in the photo-generated current, as well as a very low light conversion efficiency.

In order to test light sensitivity, a second technique was devised to detect any photo-generated current produced in our samples over time. A forward bias potential

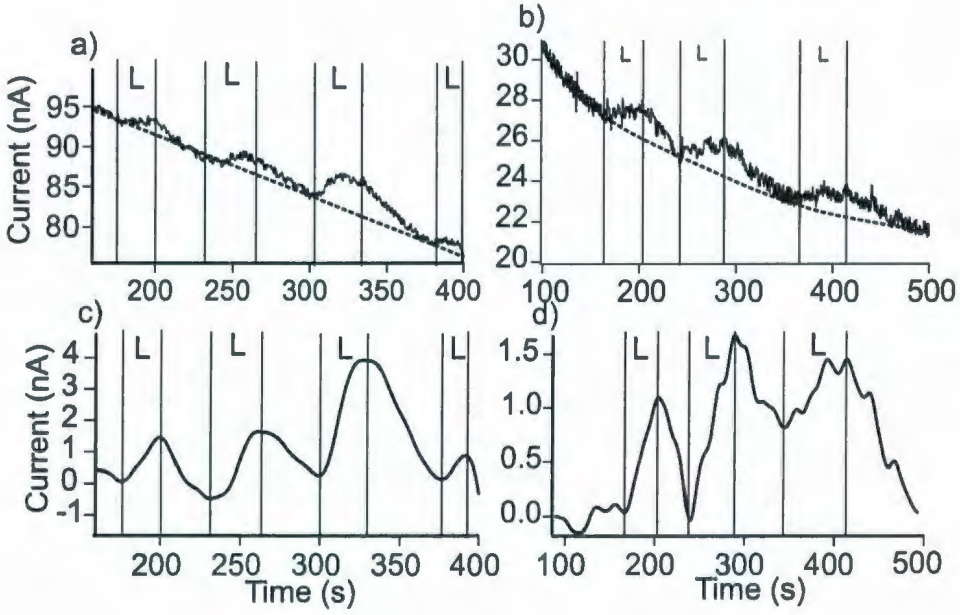

Figure 7.10: Current-time plot of two ZnO/Cu_2O/steel *pn* junctions. At times denoted with an "L", a white/blue LED light was shone upon the sample, leading to current increases. (c) and (d) indicate the humidity sensitive current changes by subtracting the background drift (dashed line) from (a) and (b), respectively.

of 1 V was applied using a stainless steel compression contact with a planar surface area of 0.18 cm^2. The current through the junction was then recorded as a function of time, while being periodically exposed to an incident light (a $\sim$ 1 W white/blue LED). Figure 7.10 shows a light-dependent current increase ($\sim$ nA), with a time-dependent current drift ($\sim$ minutes). This current drift had been observed earlier by our group for ZnO/stainless steel[41], but its origins are unclear.

Although our junction has a low efficiency, it demonstrates a proof-of-concept for photovoltaic response in electrodeposited ZnO/Cu_2O that had not been reported in the literature prior to the start of our project. Other research groups have since published results from similar photovoltaic junctions[138, 156, 157]. ZnO/Cu_2O solar cells

have even been deposited with baths similar to ours with efficiencies of 0.41%[147]. Taking our work in the context of these more recent studies, the solar conversion efficiency of electrodeposited ZnO/Cu_2O *pn* junctions is not competitive with other solar cell devices such as silicon and gallium arsenide based cells[65]. While theoretical predictions of the solar conversion efficiencies of ZnO/Cu_2O photovoltaic cells are near 18%[146], the highest efficiencies reported are for samples deposited using arc plasma evaporation (1.52%)[158] and ZnO deposited on Cu_2O (made through high temperature oxidation of a copper metal sheet) using an ion beam sputtering system in conjunction with a Mg_2F antireflective coating[159]. Recent studies have linked this low-efficiency with crystal defects at the ZnO/Cu_2O interface and within the Cu_2O[147]. While no work has been performed attempting to quantify and reduce the defect concentration of Cu_2O, our research of ZnO single layers (see Chapter 6) has shown that electrodeposition can have a large effect on carrier/defect concentration.

Chapter 8

Conclusions and Future Work

8.1 Conclusions

Originally, the goal of this thesis work was to explore the electrochemical synthesis of ZnO/Cu_2O *pn* heterojunctions for applications in solar cells. Electrodeposition of *pn* junctions was in its infancy, with most electrodeposited *pn* junctions using at least one other method to synthesize one of the component layers[160]. When we first explored the ZnO/Cu_2O system, we found that the rectifying characteristics of our electrodeposited multi-layers were unexpectedly inconsistent. Careful examination of the constituent layers indicated that there were complicated issues with conduction through the ZnO layer that had not been previously reported in the literature. We then focused intensely on understanding conduction to and through the ZnO layer.

My research has since made some very interesting advances in the field of electrical

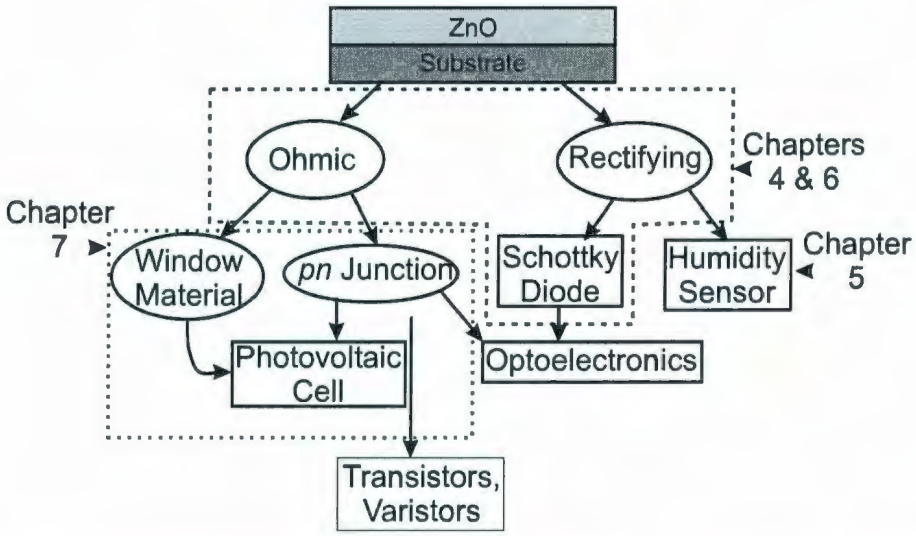

Figure 8.1: This flow chart indicates how this thesis work can influence different areas of semiconductor and device physics. Here, we have concepts in ovals and applicable devices are displayed within rectangular boxes.

conduction to and through ZnO/metal junctions. We were the first to report the ability to selectively synthesize either ohmic or rectifying ZnO/metal contacts[40, 41]. This discovery has some important consequences for the use of electrodeposited ZnO in electronic devices. The flow chart in Figure 8.1 illustrates how this discovery can be pertinent to several areas of materials physics.

The immediate result of being able to predictably create rectifying ZnO/substrate junctions is the selective formation of Schottky diodes (Chapter 4, improved in Chapter 6). ZnO Schottky diodes have recently been linked to novel optoelectronic devices such as UV emitters, UV photodetectors, photodiodes, and transparent thin-film transistors[19, 82, 86]. This earlier ZnO Schottky diode research has used relatively expensive metals (Pd, Pt, Au, and Ag) and ultra high vacuum synthesis

techniques[25], whereas our samples were created using multiple types of stainless steel. The ability to cost-effectively deposit reliable Schottky diodes could have an impact on UV range optoelectronic applications, where UHV techniques are the norm.

Another attribute of rectifying ZnO/metal junctions that is directly applicable to device physics is its gas sensitivity[161, 162]. An important complementary concern is the effect of relative humidity sensitivity on such sensing devices. To assess the feasibility of using ZnO-based sensors in a humid atmosphere, we studied the humidity sensitivity of rectifying Schottky diodes. Our results indicate that the current response of rectifying ZnO/metal junctions is very dependent upon the level of relative humidity. In Chapter 6, we cataloged the effect of relative humidity on the functionality of ZnO/metal junctions, as well as determined a hydrophobic coating that can be used to increase the stability of these junctions. In a natural extension of this work, we studied the feasibility of these junctions as relative humidity sensors, but found erratic responses at high humidities. Our studies also showed that relative humidity has a much smaller effect on the resistance of ohmic ZnO/metal junctions.

In Chapter 5, we studied the effect of deposition conditions on the carrier concentration of our electrodeposited ZnO/metal substrates. Our carrier concentration studies showed that we can effectively change the carrier concentration and bandgap of our ZnO/metal junction through manipulation of deposition potential and bulk pH without using external dopants. This has ramifications for both Schottky and ohmic ZnO/metal junction applications, as carrier concentration is very important to

depletion width formation in Schottky and *pn* junctions. Consequently, controlling carrier concentration can have a large impact on a variety of semiconductor applications.

Another consequence of our ohmic *vs.* rectifying studies is that we can also selectively produce low-resistance ohmic ZnO/metal junctions. In particular, low-resistance connections to ZnO are important for use in semiconducting multi-layer devices where relatively high current throughput is important to their functionality[18, 43, 65]. For example, these ohmic junctions can be used when creating window layers and *pn* junctions for devices such as photovoltaic cells, transistors, and varistors[22, 163]. As proof-of-concept, we explored multi-junction systems in Chapter 7. By choosing our ZnO deposition conditions carefully, and experimenting with a range of Cu_2O deposition conditions, we were able to achieve light-sensitive ZnO/Cu_2O *pn* junctions.

My thesis work proves that, while controlling electronic properties of ZnO can be very complicated, systematic synthesis-property studies yield greater control of ZnO that aids understanding and performance of complex multi-layer systems.

I have discovered methods to control the current-voltage behaviour, carrier concentrations, and band gaps of electrodeposited ZnO/metal junctions. Even though semiconductor research has been undertaken for well over a century, my work shows that even well known systems can deliver surprising results if the right questions are asked.

8.2 Future Work

This thesis work was originally driven by the goal of creating exclusively electrochemically synthesized *pn* junctions. Since we started our project, this goal has been achieved by other groups, but reported that the solar conversion efficiencies of these junctions are not competitive with the established silicon-based solar cells[46, 147]. This difficulty highlights some of the opportunities for both electrodeposited semiconductor physics research, and device physics research in general.

One of the current drawbacks to electrodeposition can be the comparatively unorganized (rough and non-patterned) surfaces of electrodeposits. While an increase in interface area can increase the functionality of some multi-layer semiconductor devices (such as photovoltaic cells), it is often more beneficial to have well-characterized, low-defect interfaces[46, 146, 147]. Consequently, it would be useful to study the effect of deposition conditions on the level of organization of the semiconductor surface, specifically for multi-layer systems. While the electrodeposition of "single crystal" monolayers on single crystal substrates has been reported previously[38, 39], electrochemically synthesized deposits are often complex. By increasing the organization of polycrystalline single layer surfaces, it may be possible to improve the performance of multi-layered devices. For example, it has been reported that window layers with an inverted pyramidal texture will increase the light-trapping ability of solar cells[18, 43], and that more efficient Cu_2O/ZnO photovoltaic functions form because of a diminished lattice mismatch between some preferred orientations[46]. This is an advantage

that high temperature/high vacuum techniques typically enjoy; the ability to grow very well organized surface topographies on multiple substrates.

With our electrodeposition technique it is possible to make more organized thin films. Slowing the kinetic growth rate with deposition temperature or electrolyte concentration[59, 60] may be one way to explore less rough ZnO surfaces. It is also possible to reduce growth along certain crystallographic directions. For example, by adding phosphate ions that preferentially attach to some basal plane faces of ZnO it is possible to reduce growth along the (001) direction[164]. This allows the growth of larger (002) orientated flat plates. Careful study of the effect of deposition deposition morphology could lead to a better surface for *pn* or Schottky junctions.

Several research groups have already started interface organization research with some systems. Recent work by John Stickney's (University of Georgia) group on electrodeposited selenide/chalcogenide multi-layer systems[36] has focused on the construction of very well characterized interfaces using atomic layer electrodeposition. Their research is a preliminary step towards using electrodeposition to create well characterized multi-layer devices. Others have been working on the electrodeposition of multi-layer metal and metal alloy structures synthesized on semiconductors (Si) for use in spin-valve applications[27, 30]. This work could possibly be expanded to include electrodeposition of the semiconductor substrate in order to tailor the electromagnetic response from spin-valves.

Similar work by Daniel Lincot's (École Nationale Supérieure de Chimie de Paris)

group on CIGS-based ($Cu(In,Ga)Se_2$) multi-layer systems, with extra CdS and ZnO layers, has utilized mostly non-electrochemical techniques[165, 166, 167]. It could be possible to utilize the work reported here to enhance these systems, as it may be able to increase the efficiency of the ZnO layers by influencing its conductance, carrier concentration, or band gap.

In general, there are many avenues of exploration open to materials physics researchers. Often, these avenues bridge chemistry, physics, and engineering in the pursuit of more efficient electronic devices. While the electrodeposition of materials for electronic devices may not hold all the answers, similar to other synthesis techniques, it is important to explore all areas of materials research in order to get the best out of our electronic devices.

Bibliography

[1] Katz, H. E.; Huang, J. *Annual Review of Materials Research* **2009,** *39,* 4.1-4.22.

[2] Hayden, O.; Agarwal, R.; Lu, W. *Nanotoday* **2008,** *3,* 12-22.

[3] Chaniotakis, N.; Sofikiti, N. *Analytica Chimica Acta* **2008,** *615,* 1-9.

[4] Linder, S. *Russian Electrical Engineering* **2007,** *78,* 509-514.

[5] Service, R. F. *Science* **2008,** *319,* 718-720.

[6] Cen, C.; Thiel, S.; Mannhart, J.; Levy, J. *Science* **2009,** *323,* 1026-1030.

[7] Reiner, J. W.; Walker, F. J.; Ahn, C. H. *Science* **2009,** *323,* 1018-1019.

[8] Exarhos, G. J.; Zhou, X.-D. *Thin Solid Films* **2007,** *515,* 7025-7052.

[9] Marotti, R. E.; Guerra, D. N.; Bello, C.; Machado, G.; Dalchiele, E. A. *Solar Energy Materials & Solar Cells* **2004,** *82,* 85–103.

[10] Rousset, J.; Saucedo, E.; Lincot, D. *Chemistry of Materials* **2009,** *21,* 534-540.

[11] Joint Commission on Powder Diffraction Standards – International Centre for Diffraction Data, "Powder Diffraction File", 2003.

[12] Van de Walle, C. G. *Physical Review Letters* **2000,** *85,* 1012-1015.

[13] Van de Walle, C. G.; Neugebauer, J. *Annual Review of Materials Research* **2006,** *36,* 179-198.

[14] Janotti, A.; Van de Walle, C. G. *Physical Review B* **2007,** *76,* 165202/1-22.

[15] Özgür, Ü.; Alivov, Y. I.; Liu, C.; Teke, A.; Reshchikov, M. A.; Doğan, S.; Avrutin, V.; Cho, S.-J.; Morkoç, H. *Journal of Applied Physics* **2005,** *98,* 041301/1-103.

[16] Ren, T.; Baker, H. R.; Poduska, K. M. *Thin Solid Films* **2007,** *515,* 7976-7985.

[17] Brillson, L. J.; Mosebacker, H. L.; Hetzer, M. J.; Strzhemechny, Y.; Jessen, G. H.; Look, D. C.; Cantwell, G.; Zhang, J.; Song, J. J. *Applied Physics Letters* **2007,** *90,* 102116/1-3.

[18] Green, M. A. *Progress in Photovoltaics: Research and Applications* **2001,** *9,* 123-135.

[19] Ip, K.; Gila, B. P.; Onstine, A. H.; Lambers, E. S.; Heo, Y. W.; Baik, K. H.; Norton, D. P.; Pearton, S. J.; Kim, S.; LaRoche, J. R.; Ren, F. *Applied Physics Letters* **2004,** *84,* 5133-5135.

[20] Oh, M.-S.; Hwang, D.-K.; Lim, J.-H.; Choi, Y.-S.; Park, S.-J. *Applied Physics Letters* **2007,** *91,* 042109/1-3.

[21] Chambers, S. A. *Surface Science* **2007,** *601,* 5313-5314.

[22] Look, D. C. *Surface Science* **2007,** *601,* 5315-5319.

[23] Lee, S. T.; Wang, N.; Lee, C. *Materials Science and Engineering* **2000,** *A286,* 16-23.

[24] Liu, Y.; Gorla, C. R.; Liang, S.; Emanetoglu, N.; Lu, Y.; Shen, H.; Wraback, M. *Journal of Electronic Materials* **2000,** *29,* 69-74.

[25] Allen, M. W.; Alkaisi, M. M.; Durbin, S. M. *Applied Physics Letters* **2006,** *89,* 103520/1-3.

[26] Da Silva, R. C.; Schwarzacher, W. *Journal of The Electrochemical Society* **2007,** *154,* D88-D90.

[27] de Araujo, C. I. L.; Munford, M. L.; Delatorre, R. G.; da Silva, R. C.; Zoldan, V. C.; Pasa, A. A.; Garcia, N. *Applied Physics Letters* **2008,** *92,* 222101/1-3.

[28] Naghavi, N.; Hubert, C.; Etcheberry, A.; Bermudez, V.; Hariskos, D.; Powalla, M.; Lincot, D. *Progress in Photovoltaics: Research and Applications* **2009,** *17,* 1-9.

[29] Lincot, D. *et al. Solar Energy* **2004,** *77,* 725-737.

[30] Jiang, Y.; Yao, S.; Zhang, W. *Thin Solid Films* **2008,** *516,* 3210-3216.

[31] Wang, H.; Wu, Y.; Li, Q.; Wang, M.; Li, G.; Zhang, L. *Applied Physics Letters* **2006,** *89,* 052107/1-3.

[32] Kim, S.-S.; Nah, Y.-C.; Noh, Y.-Y.; Jo, J.; Kim, D.-Y. *Electrochimica Acta* **2006,** *51,* 3814-3819.

[33] BuAli, Q.; Johns, L. E.; Narayanan, R. *Electrochimica Acta* **2006,** *51,* 2881-2889.

[34] Shen, W.; Mazumdar, D.; Zou, X.; Liu, X.; Schrag, B. D.; Xiao, G. *Applied Physics Letters* **2006,** *88,* 182508/1-3.

[35] Wang, J.; Polizzi, E.; Ghosh, A.; Datta, S.; Lundstrom, M. *Applied Physics Letters* **2005,** *87,* 043101/1-3.

[36] Vaidyanathan, R.; Cox, S. M.; Happek, U.; Banga, D.; Mathe, M. K.; Stickney, J. L. *Langmuir* **2006,** *22,* 10590-10595.

[37] Bao, Z. L.; Majumder, S.; Talin, A. A.; Arrott, A. S.; Kavanagh, K. L. *Journal of The Electrochemical Society* **2008,** *155,* H841-H847.

[38] Boonsalee, S.; Gudavarthy, R. V.; Bohannan, E. W.; Switzer, J. A. *Chemistry of Materials* **2008,** *20,* 5737-5742.

[39] Limmer, S. J.; Kulp, E. A.; Switzer, J. A. *Langmuir* **2006,** *22,* 10535-10539.

[40] Chatman, S.; Ryan, B. J.; Poduska, K. M. *Applied Physics Letters* **2008,** *90,* 012103/1-3.

[41] Chatman, S.; Poduska, K. M. *ACS Applied Materials and Interfaces* **2009,** *1,* 552-558.

[42] Chatman, S.; Emberley, L.; Poduska, K. M. *ACS Applied Materials and Interfaces* **2009,** .

[43] Green, M. A. *Nanotechnology* **2000,** *11,* 401-405.

[44] Green, M. A. *Physica E* **2002,** *14,* 11-17.

[45] Golden, T. D.; Shumsky, M. G.; Zhou, Y.; VanderWerf, R. A.; Van Leeuwen, R. A.; Switzer, J. A. *Chemistry of Materials* **1996,** *8,* 2499-2504.

[46] Akimoto, K.; Ishizuka, S.; Yanagita, M.; Nawa, Y.; Paul, G. K.; Sakurai, T. *Solar Energy* **2006,** *80,* 715-722.

[47] Brattain, W. H. *Review of Modern Physics* **1951,** *23,* 203-212.

[48] Chee, K. T.; Keowsim, T. .; Weichman, F. L. *Canadian Journal of Physics* **1979,** *57,* 988-993.

[49] Pourbaix, M. *Atlas of electrochemical equilibria in aqueous solutions;* Pergamon Press: New York, 1966.

[50] Bard, A. J.; Faulkner, L. R. *Electrochemical methods : fundamentals and applications;* John Wiley: New York, 2001.

[51] Wang, J. *Analytical Electrochemistry;* Wiley-VCH: New York, Second ed.; 2000.

[52] Petrucci, R. H.; Harwood, W. S. *General Chemistry: Principles and Modern Applications;* Macmillan Pubplishing Company: New York, Sixth ed.; 1989.

[53] Therese, G. H. A.; Kamath, P. V. *Chemisty of Materials* **2000,** *12,* 1195-1204.

[54] Mahalingam, T.; Chitra, J. S. P.; Chu, J. P.; Moon, H.; Kwon, H. J.; Kim, Y. D. *Journal of Materials Science: Materials in Electronics* **2006,** *17,* 519-523.

[55] Switzer, J. A.; Liu, R.; Bohannan, E. W.; Ernst, F. *Journal of Physical Chemistry B* **2002,** *106,* 12369-12372.

[56] Lu, D.; Tanaka, K. *Journal of The Electrochemical Society* **1996,** *143,* 2105-2109.

[57] Wijesundera, R.; Hidaka, M.; Koga, K.; Sakai, M.; Siripala, W. *Thin Solid Films* **2006,** *500,* 241-246.

[58] Switzer, J. A. *American Ceramic Society Bulletin* **1987,** *66,* 1521-1524.

[59] Izaki, M.; Omi, T. *Applied Physics Letters* **1996,** *68,* 2439-2440.

[60] Yoshida, T.; D.Komatsu,; N.Shimokawa,; H.Minoura, *Thin Solid Films* **2004,** *451-452,* 166-169.

[61] Cox, J. A.; Brajter, A. *Electrochimica Acta* **1979,** *24,* 517-520.

[62] Peulon, S.; Lincot, D. *Journal of The Electrochemical Society* **1998,** *145,* 864-874.

[63] Goux, A.; Pauporte, T.; Chivot, J.; Lincot, D. *Electrochimica Acta* **2005,** *50,* 2239-2248.

[64] Serway, R. A. *Physics for Scientists and Engineers;* Saunders College Publishing: Philadelphia, 4th ed.; 1996.

[65] Neamen, D. *An Introduction to Semiconductor Devices;* McGraw-Hall: Boston, 2006.

[66] Ashcroft, N. W.; Mermin, N. D. *Solid State Physics;* Brooks/Cole Thomas Learning: Austalia, 1976.

[67] Kittel, C. *Introduction to Solid State Physics;* John Wiley and Sons Inc.: New York, Seventh ed.; 1996.

[68] Cox, S. F. J.; Davis, E. A.; Cottrell, S. P.; King, P. J. C.; Lord, J. S.; Gil, J. M.; Alberto, H. V.; Vilão, R. C.; Duarte, J. P.; Ayres de Campos, N.; Weidinger, A.; Lichti, R. L.; Irvine, S. J. C. *Physical Review Letters* **2001,** *86,* 2601-2604.

[69] McCluskey, M. D.; Jokela, S. J.; Zhuravlev, K. K.; Simpson, P. J.; Lynn, K. G. *Applied Physics Letters* **2002,** *80,* 3807-3809.

[70] Jokela, S.; McCluskey, M.; Lynn, K. *Physica B* **2003,** *340-342,* 221-224.

[71] Nickel, N. H.; Fleischer, K. *Physical Review Letters* **2003,** *90,* 197402/1-3.

[72] McCluskey, M. D.; Jokela, S. J.; H. Oo, W. M. *Physica B* **2006,** *376-377,* 690-693.

[73] Van de Walle, C. G.; Neugebauer, J. *Nature* **2003,** *423,* 626-628.

[74] Li, X.; Keyes, B.; Asher, S.; Zhang, S. B.; Wei, S.-H.; Coutts, T. J.; Limpijumnong, S.; Van de Walle, C. G. *Applied Physics Letters* **2005,** *86,* 122107/1-3.

[75] Van de Walle, C. G. *Physica Status Solidi B* **2003,** *235,* 89-95.

[76] Selim, F. A.; Weber, M. H.; Solodovnikov, D.; Lynn, K. G. *Physical Review Letters* **2007,** *99,* 085502/1-3.

[77] Jacobi, K.; Zwicker, G.; Gutmann, A. *Surface Science* **1984,** *141,* 109-125.

[78] Ozawa, K.; Sawada, K.; Shirotori, Y.; Edamoto, K.; Nakatake, M. *Physical Review B* **2003,** *68,* 125417/1-6.

[79] Wang, L.-S.; Wu, H.; Dezsai, S. R.; Lou, L. *Physical Review B* **1996,** *53,* 8028-8031.

[80] Ellmer, K. *Journal of Physics D: Applied Physics* **2001,** *34,* 3097-3108.

[81] Wright, J. S. *et al. Applied Surface Science* **2007,** *253,* 3766-3772.

[82] Newton, M. C.; Firth, S.; Warburton, P. A. *Applied Physics Letters* **2006,** *89,* 072104/1-3.

[83] von Wenckstern, H.; Biehne, G.; Rahman, R. A.; Hochmuth, H.; Lorenz, M.; Grundmann, M. *Applied Physics Letters* **88,** 092102/1-3.

[84] Weichsel, C.; Pagni, O.; Leitch, A. W. R. *Semiconductor Science and Technology* **2005,** *20,* 840-843.

[85] Kim, S.-H.; Kim, H.-K.; Seong, T.-Y. *Applied Physics Letters* **2005,** *86,* 022101/1-3.

[86] Kim, S.-H.; Kim, H.-K.; Seong, T.-Y. *Applied Physics Letters* **2005,** *86,* 112101/1-3.

[87] Strzhemechny, Y. M.; Mosbacker, H. L.; Look, D. C.; Reynolds, D. C.; Litton, C. W.; Garces, N. Y.; Giles, N. C.; Halliburton, L. E.; Niki, S.; Brillson, L. J. *Applied Physics Letters* **2004,** *84,* 2545-2547.

[88] Kim, S.; Kang, B. S.; Ren, F.; Ip, K.; Heo, Y. W.; Norton, D. P.; Pearton, S. J. *Applied Physics Letters* **2004,** *84,* 1698-1700.

[89] Liang, S.; Sheng, H.; Liu, Y.; Huo, Z.; Lu, Y.; Shen, H. *Journal of Crystal Growth* **2001,** *225,* 110-113.

[90] Leem, D.-S.; Song, J.-O.; Hong, W.-K.; Maeng, J.-T.; Kwak, J. S.; Park, Y.; Seong, T.-Y. *Applied Physics Letters* **2005,** *86,* 102102/1-3.

[91] Windsich, C. F.; Exarhos, J. *Journal of Vacuum Science and Technology A: Vacuum, Surfaces, and Films* **1999,** *18,* 1677-1680.

[92] Fabregat-Santiago, F.; Garcia-Belmonte, G.; Bisquert, J.; Bogdanoff, P.; Zaban, A. *Journal of The Electrochemical Society* **2003,** *150,* E293-E298.

[93] Bizzotto, D. "Dan Bizzotto Homepage", Online, http://www.chem.ubc.ca/personnel/faculty/bizzotto/.

[94] Katayama, J.; Ito, K.; Matsuoka, M.; Tamaki, J. *Journal of Applied Electrochemistry* **2004,** *34,* 687-692.

[95] Lincot, D. *Thin Solid Films* **2005,** 40-48.

[96] Lasocha, W.; Lewinski, K. "Prozski", World Wide Web, Last accessed Fall 2003.

[97] Schwarzenbach, D. "LATCON: Program for the LS-refinement of Lattice Constants", 1975.

[98] Schwarzenbach, D.; Abrahams, S. C.; Flack, H. D.; Gonschorek, W.; Hahn, T.; Huml, K.; Marsh, R. E.; Prince, E.; Robertson, B. E.; Wilson, J. S. R. A. J. C. *Acta Cryrstaollgraphica* **1989,** *A45,* 63-75.

[99] Schwarzenbach, D.; Abrahams, S. C.; Flack, H. D.; Prince, E.; Wilson, A. J. C. *Acta Cryrstaollgraphica* **1995,** *A51,* 565-569.

[100] Goldstein, J. I.; Newbury, D. E.; Echlin, P.; Joy, D. C.; Fiori, C.; Lifshin, E. *Scanning Electron Microscopy and X-Ray Microanalysis: A Text for Biologists, Materials Scientists, and Geologists;* Plenum Press: New York, 1981.

[101] Reimer, L. *Scanning Electron Microscopy;* Springer Series in Optical Sciences Springer-Verlag: Berlin, 1985.

[102] Riveros, G.; Gómez, H.; Hendríquez, R.; Sshrebler, R.; Córdova, R.; Marotti, R. E.; Dalchiele, E. *Boletín de la Sociedad Chilena de Química* **2002,** *47,*.

[103] Kim, H.-K.; Han, S.-H.; Seong, T.-Y.; Choi, W.-K. *Applied Physics Letters* **2000,** *77,* 1647–1649.

[104] Chatman, S.; Noel, A. J. G.; Poduska, K. M. *Journal of Applied Physics* **2005,** *98,* 113902/1-6.

[105] Dharmadasa, I. M.; Haigh, J. *Journal of The Electrochemical Society* **2006,** *153,* G47-G52.

[106] Canava, B.; Lincot, D. *Journal of Applied Electrochemistry* **2000,** *30,* 711-716.

[107] Neville, R. C.; Mead, C. A. *Journal of Applied Physics* **1970,** *41,* 3795-3800.

[108] Grabitz, P.; Rau, U.; Werner, J. *Thin Film Solids* **2005,** *487,* 14-18.

[109] Sode, A.; Li, W.; Yang, Y.; Wong, P. C.; Gyenge, E.; Mitchell, K. A. R.; Bizzotto, D. *Journal of Physical Chemistry B* **2006,** *110,* 8715-8722.

[110] Huang, J.; Lu, H.; Ye, Z.; Wang, L.; Zhao, B.; He, H. *Journal of Applied Physics* **2007,** *102,* 053521/1-3.

[111] Marotti, R. E.; Giorgi, P.; Machado, G.; Dalchiele, E. A. *Solar Energy Materials & Solar Cells* **2006,** *90,* 2356-2361.

[112] Ishizaki, H.; Imaisumi, M.; Matsuda, S.; Izaki, M.; Ito, T. *Thin Solid Films* **2002,** *411,* 65-68.

[113] Mora-Seró, I.; Fabregat-Santiago, F.; Denier, B.; Bisquert, J. *Applied Physics Letters* **2006,** *89,* 203117/1-3.

[114] Wagner, T.; Waitz, T.; Roggenbuck, J.; Fröba, M.; Kohl, C.-D.; Tiemann, M. *Thin Solid Films* **2008,** *515,* 8360-8363.

[115] Li, Z.; Geßner, A.; Richters, J.-P.; Kalden, J.; Voss, T.; Kübel, C.; Taubert, A. *Advanced Materials* **2008,** *20,* 1279-1285.

[116] Michaelis, E.; Wöhrle, D.; Rathousky, J.; Wark, M. *Thin Solid Films* **2005,** *497,* 163-169.

[117] Pajkossy, T. *Solid State Ionics* **2005,** *176,* 1997-2003.

[118] Peulon, S.; Lincot, D. *Advanced Materials* **1996,** *8,* 166-170.

[119] Burstein, E. *Physical Review* **1954,** *93,* 632-633.

[120] Ma, Y.; Du, G. T.; Yang, S. R.; Li, Z. T.; Zhao, B. J.; Yang, X. T.; Yang, T. P.; Zhang, Y. T.; Liu, D. L. *Journal of Applied Physics* **2004,** *95,* 6268-6272.

[121] Myong, S. Y.; Lim, K. S. *Applied Physics Letters* **2003,** *82,* 3026-3028.

[122] Kohan, A. F.; Ceder, G.; Morgan, D.; Van de Walle, C. G. *Phys. Rev. B: Condens. Matter* **2000,** *61,* 15019-15027.

[123] Oba, F.; Nishitani, S. R.; Isotani, S.; Adachi, H.; Tanaka, I. *Journal of Applied Physics* **2001,** *9,* 824-828.

[124] Lavrov, E. V.; Weber, J.; Börrnert, F.; Van de Walle, C. G.; Helbig, R. *Physical Review B* **2002,** *66,* 165205/1-7.

[125] Ohashi, N.; Ishigaki, T.; Okada, N.; Sekiguchi, T. *Applied Physics Letters* **2002,** *80,* 2869-2871.

[126] Ip, K.; Overberg, M. E.; Heo, Y. W.; Norton, D. P.; Pearton, S. J.; Stutz, C. E.; Luo, B.; Ren, F.; Look, D. C.; Zavada, J. M. *Applied Physics Letters* **2003,** *82,* 385-387.

[127] Barsan, N.; Koziej, D.; Weimar, U. *Sensors and Actuators B* **2007,** *121,* 18-35.

[128] Lee, C.-Y.; Lee, G.-B. *Sensor Letters* **2005,** *3,* 1-15.

[129] Chen, Z. Q.; Kawasuso, A.; Xu, Y.; Naramoto, H.; Yan, X. L.; Sekiguchi, T.; Suzuki, R.; Ohdaira, T. *Physical Review B* **2005,** *71,* 115213/1-8.

[130] Fenner, R.; Zdankiewicz, E. *IEEE Sensors Journal* **2001,** *1,* 309-317.

[131] Traversa, E.; Bearzotti, A. *Sensors and Actuators B* **1995,** *23,* 181-186.

[132] Kulwicki, B. A. *Journal of the American Ceramic Society* **2001,** *74,* 697-708.

[133] Chakrapani, V.; Angus, J. C.; Anderson, A. B.; Wolter, S. D.; Stoner, B. R.; Sumanasekera, G. U. *Science* **2007,** *318,* 1424-1430.

[134] Yoo, D. J.; Park, S. J. *Journal of The Electrochemical Society* **1996,** *143,* L89–L91.

[135] Chen, W. P.; Chan, H. L. W. *Journal of the American Ceramic Society* **2002,** *85,* 1625-1627.

[136] Zhang, D. K.; Liu, Y. C.; Liu, Y. L.; Yang, H. *Physica B* **2004,** *351,* 178–183.

[137] Mondal, A.; Mukherjee, N.; Bhar, S. K. *Materials Letters* **2006,** *60,* 1748-1752.

[138] Izaki, M.; Shinagawa, T.; Mizuno, K.-T.; Ida, Y.; Inaba, M.; Tasaka, A. *Journal of Physics D: Applied Physics* **2007,** *40,* 3326-3329.

[139] Wager, J. F. *Thin Solid Films* **2008,** *516,* 1755-1764.

[140] Sze, S. M. *Physics of Semiconductor Devices;* John Wiley and Sons Inc.: New York, 1981.

[141] Gupta, R.; Singh, R. *Materials Science in Semiconductor Processing* **2004,** *7,* 83-87.

[142] Lv, X.; Li, Y.; Hong, L.; Luo, D.; Yang, M. *Sensors and Actuators B* **2007,** *124,* 347-351.

[143] Ueda, M.; Nakamura, K.; Tanaka, K.; Kita, H.; Okamoto, K. *Sensors and Actuators B* **2007,** *127,* 463-470.

[144] Badre, C.; Pauporte, T.; Turmine, M.; Dubot, P.; Lincot, D. *Physica E* **2008,** *40,* 2454-2456.

[145] Wu, C.-H.; Williams, R. *Journal of Applied Physics* **1983,** *54,* 6721-6724.

[146] Izaki, M.; Mizuno, K.-T.; Shinagawa, T.; Inaba, M.; Tasaka, A. *Journal of The Electrochemical Society* **2006,** *153,* C668-C672.

[147] Jeong, S.; Mittiga, A.; Salza, E.; Masci, A.; Passerini, S. *Electrochimica Acta* **2008,** *53,* 2226-2231.

[148] de Jongh, P. E.; Vanmaekelbergh, D.; Kelly, J. J. *Chemistry of Materials* **1999,** *11,* 3512-3517.

[149] Poizot, P.; Hung, C.-J.; Nikiforov, M. P.; Bohannan, E. W.; Switzer, J. A. *Electrochemical and Solid-State Letters* **2003,** *6,* C21-C25.

[150] Liu, R.; Kulp, E. A.; Oba, F.; Bohannan, E. W.; Ernst, F.; Switzer, J. A. *Chemistry of Materials* **2005,** *17,* 725-729.

[151] Leopold, S.; Arrayet, J. C.; Bruneel, J. L.; Herranen, M.; Carlsson, J.-O.; Argoul, F.; Servant, L. *Journal of The Electrochemical Society* **2003,** *150,* C472-C477.

[152] Dong, Y.; Li, Y.; Wang, C.; Cui, A.; Deng, Z. *Journal of Colloid and Interface Science* **2001,** *243,* 85-89.

[153] Ho, L.; Ervin, K. M.; Lineberger, W. C. *Journal of Chemical Physics* **1990,** *93,* 6987-7002.

[154] Mizuno, K.; Izaki, M.; Murase, K.; Shinagawa, T.; Chigane, M.; Inaba, M.; Tasaka, A.; Awakura, Y. *Journal of The Electrochemical Society* **2005,** *152,* C179-C182.

[155] Tang, Y.; Chen, Z.; Jia, Z.; Zhang, L.; Li, J. *Materials Letters* **2005,** *59,* 434 438.

[156] Paul, G.; Ghosh, R.; Bera, S.; Bandyopadhyay, S.; Sakurai, T.; Akimoto, K. *Chemical Physics Letters* **2008,** *463,* 117-120.

[157] Hsueh, T.-J.; Hsu, C.-L.; Chang, S.-J.; Guo, P.-W.; Hsieh, J.-H.; Chen, I.-C. *Scripta Materialia* **2007,** *57,* 53-56.

[158] Minami, T.; Miyata, T.; Ihara, K.; Minamino, Y.; Tsukada, S. *Thin Solid Films* **2006,** *494,* 47-52.

[159] Mittiga, A.; Salza, E.; Sarto, F.; Tucci, M.; Vasanthi, R. *Applied Physics Letters* **2006,** *88,* 163502/1-3.

[160] Izaki, M.; Murasumi, A.; Chigane, M.; Ishikawa, M.; Yamashita, M.; Katayama, J.-I.; Takahashi, H.; Nakamura, H. *Electrochemical and Solid-State Letters* **2000,** *3,* 501-503.

[161] Liu, C.-Y.; Chen, C.-F.; Leu, J.-P. *Journal of The Electrochemical Society* **2009,** *156,* J16-J19.

[162] Zhang, T.; Zeng, Y.; Fan, H. T.; Wang, L. J.; Wang, R.; Fu, W. Y.; Yang, H. B. *Journal of Physics D: Applied Physics* **2009,** *42,* 045103/1-8.

[163] Wager, J. F. *Science* **2003,** *300,* 1245-1246.

[164] Imai, H.; Iwai, S.; Yamabi, S. *Chemistry Letters* **2004,** *33,* 768-769.

[165] Darga, A.; Mencaraglia, D.; Djebbour, Z.; Dubois, A. M.; Guillemoles, J.; Connolly, J.; Roussel, O.; Lincot, D.; Canava, B.; Etcheberry, A. *Thin Solid Films* **2009,** *517,* 2550-2553.

[166] Hubert, C.; Naghavi, N.; Etcheberry, A.; Roussel, O.; Hariskos, D.; Powalla, M.; Kerrec, O.; Lincot, D. *Physica Status Solidi A* **2008,** *205,* 2335-2339.

[167] Canava, B.; Roussel, O.; Guillemoles, J.; Lincot, D.; Etcheberry, A. *Physica Status Solidi C* **2006,** *3,* 2551-2554.